UCRL-19464

C.2

RECEIVED
LAWRENCE
RADIATION LABORATORY

DOCUMENTS SECTION

STUDY OF DIPIONS IN THE MASS RANGE 400 TO 1000 MeV PRODUCED IN $\pi^- p$ COLLISIONS

Thambu Narayanaiyenger Rangaswamy
(Ph. D. Thesis)

May 20, 1970

AEC Contract No. W-7405-eng-48

TWO-WEEK LOAN COPY

This is a Library Circulating Copy which may be borrowed for two weeks. For a personal retention copy, call Tech. Info. Division, Ext. 5545

LAWRENCE RADIATION LABORATORY
UNIVERSITY of CALIFORNIA BERKELEY

UCRL-19464 c.2

DISCLAIMER

This document was prepared as an account of work sponsored by the United States Government. While this document is believed to contain correct information, neither the United States Government nor any agency thereof, nor the Regents of the University of California, nor any of their employees, makes any warranty, express or implied, or assumes any legal responsibility for the accuracy, completeness, or usefulness of any information, apparatus, product, or process disclosed, or represents that its use would not infringe privately owned rights. Reference herein to any specific commercial product, process, or service by its trade name, trademark, manufacturer, or otherwise, does not necessarily constitute or imply its endorsement, recommendation, or favoring by the United States Government or any agency thereof, or the Regents of the University of California. The views and opinions of authors expressed herein do not necessarily state or reflect those of the United States Government or any agency thereof or the Regents of the University of California.

UNIVERSITY OF CALIFORNIA

LAWRENCE RADIATION LABORATORY
BERKELEY, CALIFORNIA 94720
TELEPHONE (415) 843-2740

June 2, 1971

TO: Recipients of UCRL-19464, "Study of Dipions in the Mass Range 400 to 1000 MeV produced in $\pi^- p$ Collisions," May 20, 1970

The results presented in this paper are from a preliminary analysis of the data and are known to contain errors. Specifically, Tables I – V and VII – X and Figures 20 – 32 are incorrect. The reader is referred to UCRL-20824 for the final results of the analysis of this data.

A. R. Clark

Study of Dipions
in the Mass Range 400 to 1000 MeV
Produced in $\pi^- p$ Collisions

Contents

Abstract iv
I. Introduction 1
II. Experimental Setup and Data Collection 4
A. Beam 5
B. Target 6
C. Diboson Spectrometer 7

III. Data Processing 12
A. Scanning and Measuring 12
B. Reconstruction 17
C. Orbits and Momenta 17
D. Beam Momentum 18
E. Vertex and Kinematic Fits 19
F. Detection Efficiency 19
G. Systematic Errors 23
IV. Results 24
V. Conclusions 38

Acknowledgments 41
Appendices
A. Quantities Relevant to the Design and Operation of the System 44
Effectiveness of the Counters in the Trigger Logic 46
B. Initial Guess for the Secondary Momenta. 48
C. Determination of the Orbit Parameters for the Secondaries 50
D. Parameterization of Beam Momentum. 53

References 55
Tables 59
Figure Captions 79
Figures 86

STUDY OF DIPIONS IN THE MASS RANGE 400 TO 1000 MEV PRODUCED IN $\pi^- p$ COLLISIONS

Thambu Narayanaiyengar Rangaswamy

Lawrence Radiation Laboratory
University of California
Berkeley, California

ABSTRACT

We have performed a counter-spark chamber experiment at the Bevatron to study the finer details of the $\pi\pi$ (dipion) interaction exhibited in the reaction

$$\pi^- + p \rightarrow \pi^+ + \pi^- + n$$

at incident π^- momenta of 3, 4, 4.5, 5 BeV/c. The momenta of the secondaries were measured by a large aperture magnet spectrometer (60" poletip, 23" gap Bevatron M5 magnet operated at ~ 17 Kg). The track segments were sampled by a set of optical spark chambers imbedded in the magnet. The design of the scintillation counter array and the triggering scheme vetoed a considerable fraction of πp elastic events, events with one or more π^0's and events with more than two charged secondaries. We collected a total of 1.9 million pictures all of which were scanned and measured by SASS (Spark Chamber Automatic Scanning System). Of these, 1.6×10^5 events satisfied the above reaction hypothesis. This sample is the largest so far collected in any single experiment and is comparable to the bubble chamber compilations of all existing data on this reaction. The results from

the 3 and 5 BeV/c data for the forward-backward ratio in the dipion decay and the S-wave phase shifts for iso-spin I=0 agree well with published results from previous experiments. The density matrix elements of the dipion angular distribution particularly at 3 BeV/c incident π^- momentum disagree with published results at 2.7 BeV/c. We do not believe that systematic errors in our experiment can account for this large difference. Our values for the density matrix elements are in better agreement with published results at 11.2 BeV/c incident π^- momentum. The shapes of the differential cross-section at 3 and 5 BeV/c predicted by the one pion exchange model with absorption as put forth by Gottfried and Jackson agree well with our results. Their model is unable to explain quantitatively the observed variation of the density matrix elements as a function of t, the square of the 4-momentum transfer from the target proton to the outgoing neutron.

The fits to the dipion mass distribution at 3 and 5 BeV/c lead to consistent values for the mass of ρ^0 the resonance; the widths are significantly different. For the 3 BeV/c data the fits necessitate an additional enhancement at a dipion mass ~ 645 MeV with a full width $\Gamma \sim 304$ MeV. This enhancement could arise from an improper knowledge of the background and πN cross channel effects. The 5 BeV/c data does not have a perceptible contribution from this enhancement; however there is evidence of two other enhancements in this data – one at a mass ~ 936 MeV with a full width $\Gamma \sim 47$ MeV, and another at a mass ~ 1029 MeV with a full width $\Gamma \sim 27$ MeV. The peak at 936 MeV is ~ 5 standard deviations away from the rest of the contribution and hence

statistically significant. It is unlikely that this enhancement could arise from the decay of η' (958) $\rightarrow \pi^+ \pi^- \gamma$. The peak at 1029 MeV being ~ 3 standard deviations away, is on the border line of being significant. Our estimated resolution of 22.5 MeV at the ω^0 mass leads to a negligible contribution from $\omega \rightarrow \pi^+ \pi^-$. The unweighted data however indicates a non-negligible contribution from this decay for large values of t.

The analysis of the data at 4 and 4.5 BeV/c incident momentum, now under progress, should reveal more details of the $\pi\pi$ interaction and substantiate the results at 3 and 5 BeV/c.

I. INTRODUCTION

π – mesons have played a prominent role in our understanding of strong interactions ever since Yukawa[1] predicted the existence of mesons from his model of nuclear forces. He postulated that strong interaction processes are mediated by π – mesons, similar to the electromagnetic interactions which occur through the exchange of photons. The discovery of the π – meson by Powell and his collaborators[2] came much later. In emulsion stacks exposed to cosmic rays they identified events associated with the decay of π – mesons. The advent of high energy accelerators opened up new possibilities for the study of strong interactions. The high yield, at accelerators, of pions relative to the other mesons has led to a large number of experiments for the study of pion-hadron interactions (strongly interacting particles are referred to as 'hadrons'). If we invoke the notion of particle exchanges in the various reactions then, the lowest mass hadron with the correct set of quantum numbers is expected to be the dominant exchange in a given strong interaction reaction.

Interactions between π – mesons themselves are expected to yield a significant amount of information concerning strong interactions. However, due to the lack of π – meson targets as yet,[3] one is forced to study the nature of $\pi\pi$ interaction either in the presence of other hadrons, or, in association with weak and electromagnetic processes. The latter alternative is of course a much cleaner procedure, since the corrections needed to extract the desired information are neglegible. The recent development of high energy electron-positron colliding beams have helped significantly in the study of this interaction.[4] The data from these colliding ring experiments are as yet limited by the small cross-section for such processes as well as the intense electromagnetic background around the

collision volume. Apart from this interesting development another way to study the $\pi\pi$ interaction is in Ke_4 decays.[5] Even though this is a well understood procedure, limitations arise from the low yield and more significantly from the low mass of the decaying K-meson which restricts the maximum energy of the dipion system. Therefore, one is tempted to use the information from this procedure as a cross-check and look for other possibilities.

The only other possibility is to extract the $\pi\pi$ interaction from the πN reactions involving two or more pions in the final state. The strong interaction between the nucleons and the pions, which is superimposed on the $\pi\pi$ interaction, adds a great deal of complexity as well as a certain amount of ambiguity to the process of extraction. The prescription for the extraction procedure was given by Goebel[6] and by Chew and Low.[7] They argued that the 'peripheral πN interactions' in which very small 4-momenta are transferred from the initial to the final nucleon would be dominated by the lowest mass hadron exchange, namely the π - meson. Since the nucleon is a 'spectator' in such a process its presence can be accounted for through appropriate form factors. In addition one can make an extrapolation to put the virtual exchanged π-meson on the mass shell, the extent of extrapolation being quite small. This is the well known Chew-Low extrapolation procedure for the study of the π-π interaction. There have been many experiments[8] which have used this procedure for the study of the above interaction. All these experiments show the presence of the known boson resonances, the ρ-meson being the most dominant. One curious feature in these experiments is the varying width and mass of the ρ^0 meson depending on the momentum transfers between the nucleons.[9] Durand and Chiu[10] proposed that this might be due to interference with an S=0

resonant state hidden beneath the ρ^o resonance. No experiment as yet has seen an explicit S-wave resonance in the mass spectrum within the ρ^o region. Although there is evidence that the S-wave T=0 phaseshift passes through a resonance slightly below the mass of the ρ^o,[11] the large non-resonant S-wave background imposes serious limitations on observing such a resonance - all the more so because its cross-section is, at best, very small relative to the ρ^o cross-section.

With the aim of understanding these features better, we set up a counter-spark chamber experiment at the Bevatron and have collected a larger number of events of the type

$$\pi^- + p \rightarrow \pi^+ + \pi^- + n,$$

than all other experiments yet performed. As a by product, we also recorded events of the type

$$\pi^- + p \rightarrow K^+ + K^- + n$$

II. EXPERIMENTAL SETUP AND DATA COLLECTION

The dipion interaction exhibited in the reactions

$$\pi + N \rightarrow \pi + \pi + N \qquad (a)$$

has been studied by very many groups. However, in any individual study, the number of events collected has not been sufficient to study finer structures in the mass distributions and angular distributions. With the use of spark chambers the most accessible reaction in particular is,

$$\pi^- + p \rightarrow \pi^+ + \pi^- + n \qquad (b)$$

The charged particles in this reaction allow not only a good momentum measurement but also a definte identification of the specific type of reaction through kinematic fitting.

The experiment at the Bevatron, during June-December 1966, was specifically designed to obtain a high yield of events of type (b) at incident π^- momenta of 3, 4, 4.5 and 5 BeV/c. By combining a large aperture spectrometer using optical spark chambers and a selective trigger system, we achieved a high trigger rate for the desired events of type (b). The trigger requirements suppressed considerably the elastic channel

$$\pi^- + p \rightarrow \pi^- + p \qquad (c)$$

as well as the inelastic π^0 production channels

$$\begin{aligned} \pi^- + p &\rightarrow \pi^- + p + m\,\pi^0 \ (m \geq 1) \\ &\rightarrow \pi^+ + \pi^- + n + m\,\pi^0 \ (m \geq 1) \end{aligned} \qquad (d)$$

As an added feature, the outgoing particles were identified so that we could also study the reaction

$$\pi^- + p \rightarrow K^+ + K^- + n \qquad (e)$$

A π^- beam centered at one of the above mentioned momenta was allowed to impinge on a liquid hydrogen target. A beam spectrometer system, composed of a scintillator hodoscope, a pair of bending magnets and quadrupole

doublets, and a pair of optical spark chambers, was used to measure the momentum of individual beam particles. Lead sandwiched between scintillation counters partially surrounding the target helped to veto a considerable fraction of events associated with π^0's. A pair of counters around the target used as pulse height analyzers helped to reject part of the elastic events and events with more than two charged particles in the final state. A second spectrometer system located beyond the target, and consisting of a set of four optical spark chambers embedded in a large magnet (60" diameter pole face, 28" gap, and a peak field of 17 kg.), was used to determine the momentum of each outgoing particle. Events with two charged particles in the final state were selected preferentially with the aid of two sets of hodoscoped scintillation counters, one set being placed at the entrance and the other at the exit of this spectrometer. The nature of the secondary (π or K) was recorded with the help of a pressurized Freon Cerenkov counter located further downstream. The events were recorded on film which was later scanned and measured using the 'SASS' automatic scanning system.

A quantitative summary of the design and operating features is given in Appendix A.

A. Beam

Figures 1 (a), (b) show the layout of the beam at the Bevatron floor and its optical analogue. The π^- beam, produced from a copper target at the EPB (External Proton Beam) focus, is focused on to the liquid hydrogen target by means of a double focusing transport system. The hodoscope BH at the first focus of the π^- beam is made up of 28 counters, each 1/4" wide x 1/2" thick (along the beam) x 6.75" long scintillator viewed individually by a 1P21 phototube. The Cerenkov counter $\check{C}_B$ differentiated incident π^-'s from K^-'s. The beam trigger requirement demanded that this

counter be in coincidence with the beam counters S_1, S_2 and the beam hodoscope BH, along with the counters BA and DSA (downstream anti-counter) in anti-coincidence. The observed 92% efficiency of $\check{C}_B$ along with the large flux, at our energies, of π^-'s relative to K^-'s leads to an extremely low probability of misinterpreting an inciden K^- as a π^-. Since we are not using the data with incident K^- in our analysis, the inefficiency of the Cerenkov counter $\check{C}_B$ has no significance.

The beam hodoscope in association with the beam spark chambers B_1 and B_2 enabled us to measure the momentum of incident pions to $\pm$ 0.4%.

B. Target

Figure 2 shows a sketch of the target assembly. The liquid hydrogen target (3" diameter, 12" long) was surrounded on the top, bottom and, upstream left and right sides, by a lead scintillator sandwich (1/2" scintillator on either side of 1/4" Pb - a total of 1.11 radiation lengths for normal incidence). This sandwich (target anti labeled as TA in Fig. 3) serves to veto a considerable fraction (~ 20%) of events associated with π^0's. Since at our energies the π^0's come off from the target at small angles relative to the plane of the lead sandwich counter, they traverse two to three times the material afforded at normal incidence. The inner target counters IS_L, IS_R (Fig. 2) served a two-fold purpose - (a) to select preferentially events with only two minimum ionizing particles coming out of the target, and, (b) to reject events with recoil protons having a momentum $\leq$ 600 MeV/c i.e., more than twice minimum ionizing (most of these are from the forward elastic events). These two scintillators were hence designed to have a sufficiently uniform response

over the entire area and to allow pulse height discrimination. To reject protons the discriminators were set at 1.8 times the minimum ionization pulse and the electronic logic was arranged so that none of the desired two-prong inelastic events were rejected.

C. Diboson Spectrometer

The availability of the Bevatron M5 magnet (60" pole tip, 23" gap) allowed the construction of a large aperture spectrometer for measuring the momentum of the charged secondaries. The magnet was run at a peak field of 17 kg. The spectrometer assembly is shown in Fig. 3. The entrance aperture was defined by a pair of 6 channel scintillator hodoscopes. Each counter in these two arrays was 15" long, 2" wide and 1/8" thick (along the beam). The 26 channel rear hodoscope RH, together with the two large counters RH_L and RH_R, define the exit aperture of the spectrometer. RH consisted of two sets of 13 counters, one above and the other below the median plane. The gap between any two adjacent counters in each of these two sets and between the two sets themselves, due to the thickness of the wrapping on these counters, resulted in a neglegible loss of aperture. Each of the counters in RH was 18" long and 1/4" thick. The two counters at either end of each set were 6" wide, the counters in the middle being 4" wide. The sizes of these counters were chosen so as to have a neglegible loss, in trigger rate, due to two charged secondaries passing through the same counter. The exit ring counters ER above the target vetoed low momentum particles which were reflected by the magnetic field. The downstream anti-counter (DSA) vetoes primarily the beam particles which did not interact in the target as well as the π^-'s from the forward elastic cone.

The essential details of the electronics and the trigger logic is shown in Fig. 4. The trigger demanded:

1 beam particle ($S_1 + S_2$ + 1 counter in BH + $\overset{\gamma}{C}_B + \overline{BA} + \overline{DSA}$)

AND (i) 1 particle in IS_L and 1 particle in IS_R

OR (ii) $\geq$ 2 particles in IS_L and NONE in IS_R

OR (iii) $\geq$ 2 particles in IS_R and NONE in IS_L

AND 2 particles in ($ES_L + ES_R \equiv ES$)

AND 2 particles in ($RH + RH_L + RH_R$)

AND NONE in TA

AND NONE in ER

Spark Chambers:

The main features of the design and operation of the optical spark chambers is listed in Appendix A, Table 1A. The beam chambers B1 and B2 were 4 gap, aluminium foil chambers. The spark chambers located inside the magnetic field were designed to afford the minimum possible material in the path of the secondaries. Chambers 2, 3, 4 (Fig. 5a) were 'foam plate' chambers,[11] while chamber 1 (Fig. 5b) was a hollow plate chamber Each of the chambers 1, 2, 3 had four gaps whereas chamber 4 had six gaps. The total material in the path of the secondaries due to each of the chambers 1, 2, 3 was equivalent to ~ 0.023 radiation lengths. Chamber 4 afforded a total material equivalent to ~ 0.031 radiation lengths.

Six fiducials were firmly attached to each chamber - three on the top view and three on the side view. These fiducials served to locate the individual chambers on the film for the automatic scanning system which was used to measure the film. Two sets of grids per chamber (one for each view) rigidly attached to the magnet served as a calibration for

spatial reconstruction of the events. The chambers were viewed by the camera through a series of carefully designed mirrors (Fig. 6). The net combined distortion due to all the mirrors in any one view amounted to $\lesssim 0.3\%$ ($\lesssim$ 12 mils. for a 4" separation between adjacent grid marks). The entire optical system, grids and fiducials were designed to simplify the task of the automatic scanning system.

Proper alignment of all mirrors and chambers was achieved by using a laser source in place of the camera unit.

The high magnetic field of the magnet M5 causes a considerable bending of low momentum secondaries. Hence a considerable fraction of the triggers is composed of events in which one of the secondaries pass only through the spark chambers 1 and 2 within the magnetic field. A good momentum measurement on these secondaries is directly related to how well we can measure the position and orientation of the tracks in the chambers. If we were to use an electric clearing field to clear old tracks, the $(\vec{E} \times \vec{B})$ staggering of the sparks in the adjacent gaps of the chambers would lead to a poor measurement of the tracks. The alternative of using an electro-negative gas to clear old tracks was hence adopted. After extensive tests on a prototype chamber,[12] a gas mixture of 90% neon, 10% helium and 45 ppm (parts per million) of Freon-12 was used in chambers 1, 2, 3 and 4. Chamber 5 and the beam chambers B1 and B2 used the neon-helium mixture without the Freon. The beam chambers were operated with a 50V clearing field while chamber 5 had a 100V clearing field. A 20V clearing field was used on chamber 1, 2, 3 and 4 in order to clear the Freon ions, and resulted in a negligible staggering of the tracks. The 18 KV high voltage pulse for firing the chambers was limited to a width of 30 Ns by a secondary "crowbar" spark gap. This eliminated spurious breakdown in the chambers.

The efficiency of each of the chambers for two track events with at least 3 sparks on each track was very close to 100% for the time delay of ~ 320 Ns between the passage of the particle and the firing of the chambers.

The rear Cerenkov counter $\check{C}_K$ and spark chamber 5 were used for the detection of outgoing $K^{\pm}$'s. The Cerenkov counter was designed so that differentiation between charged π's and K's (with momenta $\leq$ 1.5 BeV/c) was possible over the whole range of permissible angles at the exit end of the spectrometer. The secondaries which do not pass through the rear hodoscope RH and the Cerenkov counter $\check{C}_K$, as well as those which interact either in the walls of this Cerenkov counter or ahead of it, would be recorded as K's. To eliminate this possibility spark chamber 5 was incorporated so that we could select only those events which gave a K- signal in the Cerenkov counter and had at least one non-interacting secondary producing a track in this chamber. This procedure aided considerably in selecting a cleaner sample of nK^+K^- events. Corrections are of course needed to account for the K's which decay in flight.

The data box, which was photographed along with the spark chambers, contained the run No., the frame No., the particular beam hodoscope triggered, the nature of the beam particle (π^- or K^-), and the response of the Cerenkov counter $\check{C}_K$.

The trigger rate was ~ 5/pulse and each run was terminated after 1,000 frames. At the beginning and at the end of each run the chamber fiducials, the calibration grids and the data box fiducials were exposed so as to have a constant check on chamber and mirror locations and camera magnification.

A constant check was maintained on the counting rates of all counters as well as their appropriate combinations. The high voltage pulses on all the chambers and counters, the flow rates of the neon-helium mixture and

Freon, and the magnet currents were checked every hour and corrected for any drifts. In addition the normal running was interrupted approximately every 10,000 triggers to run non-interacting beam particles all the way through the system - one run (~ 500 frames) with the M5 magnetic field switched off and another run with the M5 field on. The first run gave local corrections for the chamber locations and the latter was used to check on the central momentum of the beam.

At the beginning and at the end of the experiment the magnetic field was mapped in detail (0.3% accuracy). The chamber locations relative to the center of the M5 magnet were also measured (to $\pm$ 1/64"). The two sets of measurements agreed well within the precision of the measurements.

Figure 7 shows a photograph of the calibration grids and fiducials. In both views and for each chamber, the gap with a fiducial mark at each end indicates the first gap the particles pass through. The last gap is indicated by the associated single fiducial mark. Figure 8a shows a two-prong event which is accepted by the scanning system as a 'good' event, while the background events in 8b and 8c are rejected during scanning since they do not satisfy the 'two-prong' criteria. (See Sec. III.A.) The event frames have only the data box fiducials as reference marks.

III. DATA PROCESSING

An outline of the main stages of data processing is indicated in Fig. 9.

A. Scanning and Measuring

The film was scanned and measured on SASS (SPARK CHAMBER AUTOMATIC SCANNING SYSTEM), which is controlled by a DDP-24 computer. The scanning system is basically a computer-controlled cathode ray tube which can position a spot of light anywhere on the film; the transmitted light is measured by a photomultiplier tube. The background due to noise on the film is rejected by ensuring that the pulse height from the photomultiplier should be above a preset threshold. Whenever a dark spot (spark or fiducial) is encountered on the film during the scan, the computer records the position of the spot relative to the origin of the scan line, as well as a digitized intensity and width. The information on the intensity and width is used to match the tracks in the two views of the chambers. The positions of the accepted sparks are displayed on a second cathode ray tube for visual monitoring. A light pen associated with this display system is used either to scan selected regions on the film or to instruct the computer to accept or reject a particular fiducial or spark. An optical projector displays the frame on a screen and allows the scanner to examine the film when necessary.

The least count (1 SASS UNIT) of the system is 6 microns on the film (corresponds to a spatial resolution of 0.3 mm) for the scan direction perpendicular to the edge of the film. In the direction parallel to the edge of the film (i.e., along the gaps in the side views of chambers 1, 2, 3 and both views of B1 and B2) the least count

is 9 microns on film.

Unlike raster scans, our system could be programmed to scan a single line along each spark chamber gap on the film, whose positions were obtained from the grid and fiducial exposures. Having positioned the grid frame in the film transport system, the light pen associated with the display system is used to scan selectively on the screen entire regions which contain the fiducial and grid marks and display all the dark patches on the film within this region. The fiducial marks are then picked off with the use of the light pen and the computer records their position coordinates. These fiducials determine the start and orientation of the scans along each of the gaps or across the grid marks. The relevant information about this entire frame is punched out on paper tape to be re-used with the specific run as and when needed. The coordinates for the fiducials on the various chambers as well as those on the data box are retained in memory so as to cross-check and set the origin of the scans for the individual gaps of the chambers while scanning event frames.

Having obtained the data for specifying the scans, the system can now be set to advance in a semi-automatic fashion - i.e., automatic except for manual interruption when the computer needs help for some part of the decision-making process. The data box fiducials on each frame are measured first and the origin and orientation of the scans for the individual gaps of the various chambers are corrected linearly using the grid frame as standard. These shifts arise from jitter in the sprocket holes and the consequent differences in positioning of the film. In case the mean shift of the data box fiducials is larger than 10 SASS units, the frame is either rejected or the last grid frame in the run is measured to check whether

most of the frames agree with it within the set tolerance limits. During the running of the experiment care was taken to end a run prior to any expected movements of the camera or the rest of the apparatus. Thus, in most cases the two grid framed agreed with one another very well. The run and frame numbers, the nature of the beam particle (π^- or K^-), the specific beam hodoscope triggered and the nature of the outgoing particle(s) as indicated by the downstream counter $\check{C}_K$, are all recorded from the data box neon light panel.

The program then scans each spark chamber in order.

Each position measurement of a spot involves a set of three equally spaced scans across the spot on the film; the mean of the three center values is taken as the position of the spot. This helps to average out distortions in spark shape.

The conditions for accepting an event are:

1. One and only one beam hodoscope triggered;
2. Only one track in each view of each beam chamber;
3. Only two tracks in each of the chambers 1 and 2. In case the two tracks overlap in one of the two views, say, the side view of chamber 2, the top view of this chamber should have two distinct tracks;
4. Any track with a projected inclination larger than ($\tan^{-1}2$) radians relative to the normal to the gaps is rejected. These tracks are due to very low momentum electron tracks which bend around in the magnetic field or due to particles which scatter from the magnet yoke; in addition, due to the large inclination multiple sparks are produced in a single gap and in such cases the track orientation is not well defined;

5. The two tracks in the end view of chamber 1 had to converge within a reasonable distance from the liquid hydrogen target. This condition eliminates background from interactions upstream of the liquid hydrogen target as well as stray beam particles;

6. Downstream of chamber 2, the total number of tracks in any given chamber had to be equal to or less than that in the preceding chamber. This criterion helped to reduce background from interactions in the chambers and particles which scatter from the magnet yoke.

The sparks on each track in each view of a chamber were fitted to a straight line. (Due to the magnetic field the curvature of the particle trajectory within a chamber is sufficiently small over the accepted range of particle momenta). To reduce the background due to spurious sparks and confusion among sparks which belong to different nearby tracks, the maximum deviation of any particular spark from the fitted straight line was preset for each view of each chamber. In addition, the minimum number of sparks on a track was also preset. If the sparks in a track deviate more than the preset maximum the program calls for help, and at the same time displays on the second cathode ray tube all the sparks in the particular view. By looking at the film, the scanner now deletes with the light pen the sparks which are not part of the particular track. If the number of sparks left after this process is smaller than the allowed minimum for the particular chamber, the track is deleted from that view. The average frequency with which help was called varied from once every 5 frames to once every 20 frames depending on the quality of the film and the efficiency of the chambers and the beam conditions when the film was exposed. Help was called primarily in cases wherein:

(a) Multiple sparks in a gap lead to track robbing,

OR (b) Breakdown at the edges of a chamber result in poor multiple track efficiency,

OR (c) The tracks are very near in one view so that the sparks coalesce,

OR (d) The two tracks are superposed in a particular view,

OR (e) The sparks are faint in one of the two views,

OR (f) Dirt on the film fakes a spark!

While scanning the calibration runs with single tracks, each chamber had to have only one track.

The average time for scanning and measuring a frame, including the cases where help was called, was ~ 2 sec. The measured information for all the events was recorded on tape. Repeated sampling and scanning indicated that the scanning inefficiency for two-prong events is negligible. The maximum drifts for repeated measurements were less than 1 SASS unit. A specially prepared film with a precision grid was measured each day to check constantly the linearity of the system and possible drifts. The nonlinearity arises from:

(a) The mirror distortions in the experimental set up,

(b) The nonlinearity of the scan due to the cathode ray tube,

(c) The aberrations in the optical setup used for scanning.

The overall nonlinearity in the system amounted to less than 0.3% as measured from the known 4" spatial separation between the grid marks (≤ 12 mils in 4").

B. Reconstruction

The film coordinates of the sparks (as measured by SASS) must now be transformed into real space coordinates. The 'Far Grids' - (Fig. 10) are set as the local reference frame for each chamber. Using the 'Near Grids' we can compute the projected slope, in real space, for the optical rays reaching the camera from each of the grid marks on the far grid. Thus, given the film coordinates for a spark, we can now find by linear interpolation from the nearest neighbors the projected coordinates and slopes - (Y_F, $\tan\theta_H$) and (Z_F, $\tan\theta_V$) (Fig. 11). If (X,Y,Z) are the 3-space coordinates of the spark, then from the figure

$$\tan\theta_H = \frac{Y-Y_F}{Z-Z_g} \qquad \text{(i)} \qquad \text{and} \qquad \tan\theta_V = \frac{Z-Z_F}{Y-Y_g} \qquad \text{(ii)}$$

Since Y_g, Z_g (see Fig. 11) have been measured, we can solve (i) and (ii) for Y and Z. Also from the known X-values for the different gaps we can fit the sparks in a given chamber to straight lines in the XY and XZ planes, and obtain the vector $\vec{X} \equiv (x,y,z,\theta,\phi)$ for each of the track segments observed. (x,y,z) are the position coordinates and (θ,ϕ) give the orientation of the tracks. The corresponding error matrices are obtained using linear propagation of errors

C. Orbits and Momenta

The two trajectories through the spark chambers are now to be synthesized from the track segments in the individual chambers. All possible links connecting the track segments in adjacent chambers are set up (resulting in a 'TREE' structure). A convexity test in the XY plane demanding that θ_1 θ_{12} θ_2 be a monotone (Fig. 12) separates the segments into two groups. An initial guess of the link momentum is now obtained by allowing perturbations on a circular orbit in the magnetic

field. A field expansion of the form,

$$B_z(u) = a_1 + a_2 \sin \frac{\pi}{2} u + a_3 \cos \frac{\pi}{2} u + a_4 \sin \frac{2\pi}{2} u$$

where u is a path variable ($u = \pm 1$ at the end points of the arc) was found to be best-suited.

The equation,

$$\xi''(u) + \xi(u) = 1 + \frac{kR}{p} B_z(u),$$

for the radial perturbation ξ, is solved by the method of undetermined coefficients. (Appendix B.)

A particular solution of the form

$$\xi(u) = c_1 + c_2 \sin \frac{\pi}{2} u + c_3 \cos \frac{\pi}{2} u + c_4 \sin \frac{2\pi}{2} u$$

is assumed. The link momentum p is obtained by forcing $\xi(\pm 1) = 0$ along with a χ^2 fit of $\xi'(\pm 1)$ to the angles of the track segments. The sign of the momentum (charge) is the same as the sign of the curvature. The estimated momenta of the adjacent links are now used to prune the 'TREE' structure obtained earlier and thereby obtain the estimated momenta for the two trajectories. The trajectory parameters $\vec{u}(x,y,z,\theta,\phi,p)$ for each particle are now refined using the estimated values as initial conditions in an interative Newton-Raphson procedure and solving the differential equations of motion (Appendix C). The derivatives needed are obtained by computing orbits through the magnetic field region. When the trajectory parameters $\vec{u}$ converge within prescribed limits the coordinates $\vec{u}_o(x,y,z,\theta,\phi,p)$ at the point of closest approach to the beam are calculated.

D. Beam Momentum

The position of the incident beam particle at the first focus (as determined by the beam hodoscope) in conjunction with the direction and position of the beam particle (the center of the first gap of beam chamber

B2 is taken as the x-reference) determine the beam momentum for each event. The central momentum p_o for beam particles passing along the axis of the beam spectrometer system and its orientations θ_o relative to the axis of the diboson spectrometer are obtained from the calibration runs[13] (Appendix D). The absolute scale for the momentum is determined by the spectrometer magnets.

E. Vertex and Kinematic fits

An iterative χ^2 - minimization procedure involving linearized constraints is adopted to find the vertex coordinate and the momentum vectors of the charged particles as well as the neutron. The programs closely follow the procedures outlined by Solmitz[14] and Bock.[15] The kinematic fit demands that the events satisfy the hypothesis

$$\pi^- p \rightarrow \pi^+ \pi^- n \qquad \text{(b)}$$

In both the fits a maximum of ten iterations is allowed for the χ^2 to converge. The kinematic fitting program determines the Lab momenta $\vec{P}_{Li}$ of all the particles in the above reaction and, depending on the dynamics of interest, these can be transformed to the desired Lorentz frame.

F. Detection Efficiency

One more piece of information is needed before we invoke physical models. This is the detection efficiency of the apparatus for a given topology of reaction (b) above. As in many of the other spark chamber experiments studying this reaction, we could resort to a Monte-Carlo procedure to determine these efficiencies. There are a total of 9 independent variables in this reaction:

E_0: the incident beam energy

(x,y,z): the vertex coordinates within the target

t : the 4-momentum transfer from the initial to the final nucleon

$m_{\pi\pi}$: the dipion mass

$\theta_{\pi\pi}$: the π-π scattering angle in the dipion rest frame

ϕ_{TY}: the Treiman-Yang angle

ϕ_{PR}: the azimuthal orientation of the production plane in the lab. system

Hence, if we were to use just 10 random numbers for each of the variables, we would have to generate 10^8 events at each energy! In addition to the computer time involved here, binning and rebinning the events at different stages of the analysis would also involve a significant amount of computer time. We therefore adopted the following procedure.

Since the target and the incident beam are unpolarized, and the beam particles are parallel to one of our reference axes, the cross-section for dipion production is independent of the azimuth ϕ_{PR} around this axis. Hence, we can obtain the á priori probability of detecting an individual event with a known topology by rotating the entire event about the beam axis and computing the range of azimuthal angular acceptance for both pions.(16) This can be expressed as the overlap of the angular intervals of acceptance for each of the two particles with the given relative azimuthal angle. For particle momenta greater than ~ 500 MeV/c the limits of the accepted angular ranges were expressed as a polynomial in P and θ, where P is the momentum of the particle and θ is the angle between the beam direction and the direction of motion of the particle of interest; for smaller momenta a look-up table was used. Reflection symmetries associated with the change in sign of the charge and magnetic field

introduce some simplification in the computations. The asymmetry of the apparatus above and below the median plane prohibits additional simplication. The azimuthal angular intervals so obtained depend on the vertex coordinates (x,y,z) within the target. Since the dynamics is independent of the interaction vertex, we can now average over the target volume. The average azimuthal intervals for each secondary pion are computed over a target volume which has a cross-sectional area equal to the half-width of the incident beam. We will denote the two sets of averaged angular intervals for the two pions as $\left\{ \phi_A^+ \right\}$, $\left\{ \phi_A^- \right\}$

The DSA (downstream anti-counter), and TA (target anti-counter) which has a non-negligible cross-section for neutron interaction, introduce additional corrections to the efficiency. Since the DSA has a small aperture around the central beam direction at the exit end of the diboson spectrometer, its contribution can be analytically accounted for through an impact parameter representation in a uniform cylindrical field.[17] For a particle with momentum P and angle θ relative to the beam direction the bending angle β can be expressed as a function of P, c and h, where c is the impact parameter and h is the vertical height above the median plane at the point of closest approach. Any non-uniformity of the magnetic field is accounted for through a perturbative approach. Knowing β and θ we can find the equation to the locus of the point on the particle trajectory at the plane of the DSA counter, for the entire range of azimuthal angles around the beam direction. The points of intersection, if any, of this curve and the boundaries of the DSA counter give the limits for the angular range within which the particle hits DSA. Let us denote by $\left\{\phi_D^+\right\}$, $\left\{\phi_D^-\right\}$ the pair of sets for the angular ranges which <u>exclude</u> the regions in which the particles hit DSA. The overlap of all four of

the sets $\{\phi_A^+\}$, $\{\phi_A^-\}$, $\{\phi_D^+\}$, $\{\phi_D^-\}$ is the final set $\{\phi\}$ and the efficiency for the particular event is

$\epsilon_1 = \frac{\sum_i \Delta\phi_i}{2\pi}$ where $\Delta\phi_i$ is the ith <u>allowed range</u> in $\{\phi\}$. The corresponding set for the neutron $\{\phi_n\}$ and its polar angle θ_n relative to the beam are now known. The probability of interaction for neutrons at normal incidence is assumed to be independent of energy which is valid only for neutron kinetic energies $\gtrsim$ 100 MeV/c. (The uncertainty, in the energy threshold of the neutrons detected by the target anti-counter TA, as well as in the shape of the curve for detection efficiency vs neutron energy at low energies ($\ll$ 100 MeV/c) leads to systematic errors of ~ 8% in the detection efficiency). Any variation in efficiency is hence due to the different angles of incidence on the lead sandwich counter.[18] The average neutron inefficiency $\bar{\epsilon}_n$ for the allowed azimuthal ranges now leads to the final corrected average efficiency

$$\epsilon_o = \epsilon_1 \bar{\epsilon}_n$$

The efficiency has now been averaged over the vertex coordinates and the orientations of the dipion production plane. At each of the incident momenta, we now have a set of average efficiencies depending only on the dynamical variables t, $m_{\pi\pi}$, $\theta_{\pi\pi}$, ϕ_{TY}.

Due to the large amount of data we have it would be expensive and time consuming to compute the individual event efficiencies. We can, therefore take advantage of the fact that the efficiency varies slowly and uniformly over a large part of the allowed regions in the dynamical variables we work with - namely, t, $m_{\pi\pi}$, $\theta_{\pi\pi}$, ϕ_{TY} (the efficiency varies rapidly very near the regions with zero detection efficiency; however these regions are excluded in our analysis and results in an insignificant

loss of the data). We compute the efficiency at specified points in a 4-dimensional mesh involving the above-mentioned dynamical variables and use average efficiencies in each cell of the mesh in place of individual event efficiencies. The data is also binned in the corresponding cells so that we invariably deal with cell averages and ensembles of cells. The cells are of course chosen small enough so that uncertainties in the final fitted distributions do not arise primarily from large cell sizes.

A Monte-Carlo program was also written to compute the efficiencies and to serve as a cross-check. The results from the two procedures were tested on a small subset of the data and agreed very well.

G. Systematic Errors

The systematic error in the efficiency computations for low neutron energies is $\lesssim 8\%$, as mentioned in the previous section. The errors due to inefficiencies in the scanning as well as due to inefficiencies of the spark chambers for detecting two-prong events is negligible; the loss due to a beam track superposed on a good event is also negligible. The inefficiency in the triggering of two-prong events due to finite sizes of the counters in the hodoscope arrays ES and RH is less than 0.5%. The trigger inefficiency for two-prong events of the desired type due to the pulse height criterion on the counters IS_L and IS_R could not be determined well. These counters veto, if at all, events in which one of the two secondary pions has a relatively low momentum. However if these pions are reflected by the magnetic field, they are already accounted for in our detection efficiency computation. A pessimistic estimate for the systematic error in the trigger due to these two counters is $\lesssim 1\%$. The cross-sections we obtain indicate that the overall systematic errors are less than 10%.

IV. RESULTS

We will first discuss the salient features of the unweighted data. Consider the reaction

$$\pi^- p \rightarrow \pi^+ \pi^- x^o \qquad \text{(a)}$$

or $1 + 2 \rightarrow 3 + 4 + 5$,

where x^o is the set of all neutral particles which are undetected in our system. The invariant mass of the neutral system x^o (missing mass) is given by

$$m_x^2 = (p_1 + p_2 - p_3 - p_4)^2 \qquad (1)$$

$$= (E_{1L} + m_p)^2 + m_{\pi\pi}^2 - |\vec{P}_{1L}|^2 + 2\,\vec{P}_{1L} \cdot (\vec{P}_{3L} + \vec{P}_{4L}) + 2\,(E_{1L} + m_p)\,(E_{3L} + E_{4L})$$

where p_i is the 4-momentum
E_{iL} is the Lab. energy
$\vec{P}_{iL}$ is the Lab. 3-momentum
of ith particle
m_p is the mass of the proton

and $m_{\pi\pi}^2 = (p_3 + p_4)^2$, gives the invariant mass of the dipion system. If x^o is a neutron then $m_x = m_n$ where as for $x^o = n + \pi^o$, m_x will vary from the threshold $m_n + m_{\pi^o} = 1.075$ BeV to the kinematic limit. In our case the kinematic fit constrains x^o to the neutron mass. The unconstrained missing mass spectrum for different cuts on the χ^2 for the constrained fits is shown in Fig. 13. The huge neutron peak is clearly seen indicating that most of our events are of the type

$$\pi^- p \rightarrow \pi^+ \pi^- n \qquad \text{(b)}$$

The width of the neutron peak reflects the resolution in the incident and outgoing momenta. The efficient vetoing of π^o's as well as additional charged π's suppresses considerably the events with additional π's. The events in which one or both of the secondary pions pass through only the chambers 1 and 2 have larger values of χ^2 due to underestimation of the input errors. Since these form a considerable fraction of the events the χ^2 distribution extends to large values, even though the observed distribution agrees well with that expected for a 1-constraint fit.[37] To achieve a good separation from the background we now impose cuts on the χ^2 (50 at 3 BeV/c) selected primarily on the empirical missing mass distributions for different χ^2 - cuts. [See Fig. 13; with these cuts on χ^2, the contribution from events with missing mass $\geq m_n + m_{\pi^o}$ (1.075 BeV) is negligible.] Correction for rejected events adds an estimated systematic error of 5% in the absolute normalization of the differential cross-section. For all subsequent analysis the sample of events with these cuts on the χ^2 for the kinematic fit will be used. Since the χ^2 analysis is used only to get as clean an event sample as possible, the errors on the different variables are not propagated in the analysis, and the individual χ^2-values have no further significance.

Figure 14 shows the unweighted dipion mass distribution at 3 and 5 BeV/c. The peaks due to the well established resonances ρ^o and f^o are seen clearly. The f^o intensity is limited at the lower incident momentum (3 BeV/c) by phase space. One of the main points to note is that the total number of $\pi^+\pi^-n$ events is the largest so far collected in any single experiment and is comparable to the total bubble chamber compilations on this reaction.[19] The shapes of the ρ^o and f^o resonances seen here and

the ratio $N(f^o)/(N(\rho^o)$ are distorted due to non-uniform detection efficiency. Figure 15 shows the unweighted scatter plot of $m^2_{\pi\pi}$ vs $|t|$, where t is the square of 4-momentum transfer from the target proton (at rest in the lab.) to the neutron and is defined as

$$t = (p_p - p_n)^2 = m_p^{\ 2} + m_n^{\ 2} - 2m_p E_{nL} = (m_n - m_p)^2 - 2m_p T_{nL} = -\Delta^2$$

(note that t is space-like so that $\Delta^2 > 0$) (2)

The significance of this plot became evident through the 'One pion exchange' (OPE) model put forth by Goebel[6] and Chew and Low.[7] (This plot is often referred to as the 'Chew-Low plot'). They pointed out that, in an S-matrix approach, one can picture reaction (b) to occur through the process shown in Fig. 16, where in a known amount of 4-momentum is exchanged between the bottom and top vertices. In a non-relativistic Yukawa type potential model

$$V(r) \sim \sum_i \frac{\exp(-\mu_i r)}{r} \qquad (3)$$

where μ_i is the mass of the exchanged particle in natural units ($\hbar = c = 1$) the Fourier transform of the amplitude leads to a 'propagator function'

$$\sim \sum_i \frac{1}{\Delta^2 + \mu_i^2} \qquad (4)$$

Hence the amplitude should have a pole at $\Delta^2 = -\mu^2$ or $\Delta = +i\mu$. It is also apparent that the dominant contribution is from poles nearest the physical boundary, i.e., small μ. For the lowest angular momentum states involved, the t channel (see Fig. 16) quantum numbers are those of the pion ($J^{PG} = 0^{-\,-}$). With these plausibility arguments the above

authors conjectured that the exchange of a virtual pion could explain the details of the interaction. With a pure π-exchange the reaction should be dominantly peripheral (small Δ^2). This feature has been observed, at least qualitatively, by many previous experimenters and in other reactions as well. As seen in Fig. 15, this feature is evident in the whole range of $m_{\pi\pi}$; the solid curve represents the kinematic boundary. The unweighted density of points along $|t|$ and along $m^2_{\pi\pi}$ fall more steeply with $|t|$ and $m^2_{\pi\pi}$ than the corrected gradient due to decrease of detection efficiency with $|t|$ and $m_{\pi\pi}$.

The sub-systems (π^+n) and (π^-n) are also of interest in the analysis of the final state interactions. Figure 17 shows the unweighted histograms for the effective masses m_{π^+n} and m_{π^-n}. The outgoing π^-, which moves preferentially forward, shifts the (π^-n) spectrum to the higher end and the (π^+n) spectrum to the lower end. Unlike in the $m_{\pi\pi}$ plot we do not see a dominant production of the known πN resonances. Theremight be an enchancement in m_{π^-n} at $N^*(1238)$ and in m_{π^+n} at $N^*(1688)$; the smallness of the effect makes it hard to obtain a quantitative estimate of the cross-sections. Any resonance in either or both of the πN channels would reflect kinematically into the $\pi\pi$ channel. However the reflected peaks and widths vary with the total c.m. energy and we will use this as a handle to decipher such effects. The Dalitz plots (Figure 18) show the ρ^o and f^o; the bands do not shift with πN mass, indicating that they are dominantly due to resonances in the $\pi\pi$ channel. Also the overlap of the N^* and ρ^o bands is not significant so that in our analysis we will not include any effects due to such an overlap.

To study the details of the π–π interaction the Gottfried–Jackson frame,[21] is found most useful. This is the dipion rest frame with the incident π^- direction (in this system) being the quantization axis. (See Fig. 19). $\theta_{\pi\pi}$, the angle between the incident π^- and the outgoing π^- in this frame, is equivalent to the 2-body scattering angle for $\pi^+ + \pi^- \rightarrow \pi^+ + \pi^-$. ϕ_{TY}, referred to as the Treiman–Yang angle,[22] is the angle between the production and decay planes of the dipion. The distribution in these two angles is determined by the angular momentum state of the dipion system and the t–channel exchange mechanism.[22,23]

We will now consider the weighting procedure and the weighted angular distributions and dipion mass distributions. The weighted distributions from a preliminary analysis of the entire data at 3 and 5 BeV/c are presented.

At each c.m. energy for reaction (b) we have a set of properly weighted averages of the detection efficiency $\bar{\epsilon}$ depending only on the four dynamical variables t, $m_{\pi\pi}$, $\theta_{\pi\pi}$ and ϕ_{TY}. At each of the energies we create 4–dimensional cells in these four variables and set up a table of efficiencies averaged over each of the individual cells (see Section III). We now eliminate a priori all cells with very low efficiency (≤ 0.5) since they can lead to large statistical and systematic errors in the weighted distribution. The above cut–off on the efficiency was chosen after a series of minimizations with different preset values for the lowest acceptable efficiency. Knowing the observed number of events in each of these cells, we adopt a maximum likelihood procedure to obtain the coefficients of the angular distributions in specified regions of t and $m_{\pi\pi}$. For $m_{\pi\pi} \leq 1000$ MeV, incorporating only S and P waves in the most general case, we use the likelihood function[14]

$$W = -N_A + N_A \ln N_A - N_A \ln\left(\int_A \bar{\epsilon} R dA\right) + \sum_i N_i \ln R$$

where $\bar{\epsilon} = \bar{\epsilon}\,(\theta, \phi)\,|_{\bar{t},\, \bar{m}_{\pi\pi}}$

$$R(\theta, \phi) = N_o \Big\{ 1 + (\rho_{oo} - \rho_{11})\,(3\cos^2\theta - 1) - 3\rho_{1-1}\sin^2\theta \cos 2\phi$$
$$-6\sqrt{2}\,\mathrm{Re}\,\rho_{10}\sin\theta\cos\theta\cos\phi + 2\sqrt{3}\,\mathrm{Re}\,\rho_{oo}^{int}\cos\theta$$
$$-2\sqrt{6}\,\mathrm{Re}\,\rho_{10}^{int}\sin\theta\cos\phi \Big\}$$

ρ_{ij} are the density matrix elements for the pure angular momentum states,[24] and ρ_{ij}^{int} denotes the S–P interference terms. $A(\bar{t}, \bar{m}_{\pi\pi})$ is the selected area of the (θ, ϕ) space for a given range in $|t|$ and $m_{\pi\pi}$ over which the average efficiency is larger than the preset limit (0.05); N_i is the number of observed events in the ith cell and N_A is the total number of events within A.

The weights for each of the bins in t and $m_{\pi\pi}$ are now given by

$$w(\bar{t}, \bar{m}_{\pi\pi}) = \frac{\oint R(\bar{t}, \bar{m}_{\pi\pi}, \theta, \phi)\, d(\cos\theta)\, d\phi}{\int_{A(\bar{t},\, \bar{m}_{\pi\pi})} \epsilon(\bar{t}, \bar{m}_{\pi\pi}, \theta, \phi)\, R(\bar{t}, \bar{m}_{\pi\pi}, \theta, \phi)\, d(\cos\theta) d\phi}$$

where $\oint$ represents an integral over the entire (θ, ϕ) space. The errors on the ρ_{ij}'s are propagated to obtain the errors on the weights.

Figure 20 shows the forward–backward ratios ($\sqrt{3}\,\rho_{oo}^{int}$) for $|t| < 0.1\ (\mathrm{BeV/c})^2$ at 3 and 5 BeV/c as a function of $m_{\pi\pi}$. This ratio stays reasonably flat up to $m_{\pi\pi} \sim 0.95$ and dips down beyond it indicating that the S–P interference becomes negligible. The values for the forward–backward ratios are quite consistent with previous experiments.[8,9] Assuming that the data within the range of $|t| < 0.1\ (\mathrm{BeV/c})^2$ is dominated

by the pion pole and that δ_0^2 (the S-wave phase shift in the Isospin 2 channel) is negligible over the whole range of $m_{\pi\pi}$, crude estimates of δ_0^0, the S-wave phase shift in the I=0 channel can be obtained. Following the procedure of Jacobs,[9] we use the relation

$$\frac{F-B}{F+B} = \frac{2 \sin\delta_0^0 \sin \delta_1 \cos(\delta_0^0 - \delta_1)}{3 \sin^2 \delta_1 + 4/9 \sin^2 \delta_0^0} .$$

Figure 21 shows two of the four solutions and these agree fairly well with the phase shift analyses from the other groups.[8] To obtain better estimates one has to do an extrapolation to the pion pole and include the values of δ_0^2 obtained from $\pi^+\pi^+$ experiments.[25]

Figure 22 and Tables IA,B give the details of the density matrix elements obtained at 3 and 5 BeV/c as a function of $m_{\pi\pi}$ for $|t| \leq 0.1$ $(\text{BeV/c})^2$. The tables include the values of the forward-backward ratios as well. Table IC lists the phase shifts derived from the forward-backward ratios. Tables II and III list the values obtained at 3 and 5 BeV/c for $|t| \leq 0.22$ $(\text{BeV/c})^2$ and $|t| < 0.4$ $(\text{BeV/c})^2$. The errors listed just below the corresponding quantities are purely statistical.

We now concentrate on the ρ^0 region only. The density matrix elements, and the forward-backward ratios for $m_{\pi\pi}$ in the range 0.68 to 0.84 BeV (and 0.6 to 0.9 BeV) and for the different ranges in t, is listed in Table IV; the variation of these quantities as a function of $|t|$ is shown in Figs. 23, 24, and 25. At 3 BeV/c incident pion momentum we disagree with the results of Gutay et al. at 2.7 BeV/c[8j], particularly in the values of $(\rho_{00} - \rho_{11})$. Our statistical errors are considerably smaller. We do not believe that the systematic errors in our experiment

can account for the large difference. We obtain unique minima in the maximum likelihood fits for a wide range of starting values for the various parameters, including the set given in reference 8j. For the low t region our results are more in agreement with the data of Hyams et al.,[26] who studied the same reaction at 11.2 BeV/c incident π^- momentum. The solid curves in Figs. 23 and 24 represent predictions based on the one pion exchange model with absorption as put forth by Gottfried and Jackson.[30] (See below.)

Figures 26 and 27 show the variation of differential cross-section with t for events in the dipion mass range 0.68 to 0.84 BeV. As pointed out earlier neither the simple OPE (one pion exchange) model nor OPE with form factors agrees quantitatively with the experimental distributions of $d\sigma/dt$. Gottfried and Jackson,[23] and, Durand and Chiu[27] proposed the one pion exchange model with absorption (OPEA) to obtain better quantitative agreement with the experiments. The former authors start with the prescription given earlier by Sopkovich,[28] and introduce absorption in the initial and final states over and above the one pion exchange Born amplitude (Fig. 28). The distorted Born wave approximation leads to an amplitude

$$T(x) \simeq \exp\left[\frac{i}{2}\,\chi^{(-)}(x)\right] \; B(x) \; \exp\left[\frac{i}{2}\,\chi^{(+)}(x)\right] \qquad (1)$$

where $\chi^{\pm}$ is the phase shift in the in (out) states and $x = qb$; q is the c.m. momentum in the initial or final state and b is the impact parameter. B(x) is the one pion exchange Born amplitude. They now use the experimental fact that the momentum transfer distributions are well fitted by a purely imaginary gaussian amplitude

$$f(\Delta,q) = i\,\frac{\sigma_T}{4\pi A}\ \exp\ \left(-\frac{1}{2}\,A\,\Delta^2\right)$$

where σ_T is the total cross-section an. A is the slope of the elastic differential cross-section $d\sigma/d|t|$. The phase shift is then given by

$$\exp\left[i\ \chi(b)\right] = 1 - \frac{\sigma_T}{4\pi A}\ \exp\ (-\ b^2/2A) \qquad \text{(ii)}$$

where $\chi(b)$ is the phase shift for a wave packet having an impact parameter b.

Using the Jacob-Wick partial wave decomposition they generalize equation (i) to include the various spin states:

$$< \lambda_c\lambda_d|M|\lambda_a\lambda_b > = \sum_j\ (j+\tfrac{1}{2}) < \lambda_c\lambda_d|T_j|\lambda_a\lambda_b > d^j_{\lambda\mu}(\theta) \qquad \text{(iii)}$$

where λ_a,λ_b (λ_c, λ_d) are the helicities of the particles in the initial (final) state and $\mu = \lambda_c-\lambda_d$, $\lambda = \lambda_a-\lambda_b$.

For large angular momenta $j \gg |\lambda|$, $|\mu|$, using the asymptotic expansion

$$d^j_{\lambda\mu}(\theta) \simeq J_n\ \left[(2j+1)\ \sin\ \frac{1}{2}\ \theta)\right]\ ,$$

(where $n = \mu-\lambda$) equation (ii) can be written as an integral:

$$< \lambda_c\lambda_d\ |M|\ \lambda_a\lambda_b> \simeq \int_0^\infty xdx < \lambda_c\lambda_d|\ T(x)|\lambda_a\lambda_b > J_n\ (\omega x) \qquad \text{(iv)}$$

where $\omega = \sin\ \theta/2$

Assuming that the helicity dependences enter only in the Born term while the phase shifts are still given by (ii), the individual distorted-wave Born amplitudes for different helicity states can now be written as

$$< \lambda_c\lambda_d|T(x)|\lambda_a\lambda_b > = \exp \frac{i}{2}\left[\chi^{+}(x)\right] < \lambda_c\lambda_d|B(x)|\lambda_a\lambda_b > \exp \frac{i}{2}\left[\chi^{+}(x)\right] \quad \text{(v)}$$

Equation (v) is directly related to the density matrix elements.

The differential cross section for unpolarized beams is

$$\frac{d\sigma_{ab \to cd}}{d\Omega} = \frac{1}{64\pi^2 s} \frac{q'}{q} \frac{1}{(2s_a+1)(2s_b+1)} \sum_{\lambda} | < \lambda_c\lambda_d|M|\lambda_a\lambda_b > |^2$$

s is the square of the c.m. energy, q, q′ are the c.m. momenta in the initial and final state, and s_a, s_b, etc., are the spins. The total cross-section for the particular channel is

$$\sigma_{ab\to cd} = \frac{1}{32\pi s} \frac{q'}{q} \frac{1}{(2s_a+1)(2s_b+1)} \sum_{\lambda} \int_0^{\infty} x dx \; |< \lambda_c\lambda_d| \; T(x) \; | \; \lambda_a\lambda_b >|^2 \quad \text{(vi)}$$

We now use their model and compare our results with their predictions.

Define $C = \frac{\sigma_T}{4\pi A}$

and

$$\gamma = \frac{A}{2q^2}$$

The values of C and γ for the initial $(\pi^- p)$ state at 3 and 5 BeV/c, computed from existing data,[29] are listed in Table V. For the final $(\pi^+\pi^- n)$ state we use $C_f = 1$ and $\gamma_f = 3/4\ \gamma_i$ as per the Gottfried-Jackson prescription.[23] The solid lines in Figs. 22, 23, 26, and 27 are for these values of the parameters C_i, C_f and γ_i, γ_f. Since the experimental values for $\frac{d\sigma}{dt}$ are obtained over a restricted range of dipion masses within the ρ^o region, the curves for $\frac{d\sigma}{dt}$ have been normalized to the experimental point at $|t| = 0.04\ (\text{BeV/c})^2$. The shape of the predicted

cruve agrees reasonably well with our results. The predictions differ considerably from the experimental results for the density matrix elements.

Finally, we will discuss the weighted dipion mass distributions. Figure 29 shows the weighted dipion mass histograms for the selected regions of $|t|$ at 3 and 5 BeV/c. As mentioned earlier, the weights and errors on the mass distribution are obtained from the fits to the angular distributions in the various subintervals of $|t|$ and $m_{\pi\pi}$. The weights (and errors) for each 20 MeV bin in $m_{\pi\pi}$ are obtained through quadratic interpolations of the coefficient of the angular distributions. We have tried a variety of functions (Table VI) to fit the data. Functions I and II give poor fits at 3 as well as at 5 BeV/c (χ^2/degree of freedom $\gtrsim 10$ at 3 BeV/c; $\gtrsim 5$ at 5 BeV/c), indicating that neither a simple incoherent phase space background nor a linear approximation to the incoherent background can account for the observed distributions. Function IV proposed by Roos,[19] is expected to account for the restricted kinematic range in $|t|$ imposed on the data as well as take note of the fact that the t-dependences for the background and the ρ^0 resonance are different. Even though the fits improve slightly as compared to I and II, the χ^2 values are still too large at both 3 and 5 BeV/c.

In all the above mentioned fits the major contribution to the χ^2 is from the dipion mass regions around 600 MeV at 3 BeV/c and around 930 MeV at 5 BeV/c. We have hence tried incorporating an additional incoherent Breit-Wigner distribution over and above the ρ^0 resonance and a quadratic background (Function III(b)): with this assumption the fits improve considerably (χ^2/degree of freedom $\lesssim 5$ at 5 BeV c and $\lesssim 2$ at 5 BeV c. The results of these fits are shown in Table VII and Figs. 29-32 (solid

lines). The errors obtained from the fits have been multiplied by $\sqrt{\chi^2/D-1}$ where D is the number of degrees of freedom. The fit to the 3 BeV/c data (Fig. 29) leads to a mass $M_{\rho^o} \sim 770$ MeV and a full width at half maximum $\Gamma_{\rho^o} \sim 123$ MeV. This fit leads to a small but negative background contribution. The mass and width of the added Brit-Wigner enhancement are $m_1 \sim 645$ MeV and $\Gamma_1 \sim 300$ MeV. Even though there is evidence that there might be enhancements in the region below the ρ^o mass[31] the negative background contribution along with the large width of this enhancement indicates that its necessity in the mass distribution is very likely to arise from a poor knowledge of the background, and from the fact that kinematic reflections have not been accounted for. Another possibility is that this enhancement might be due to the detection of only the $(\pi^+\pi^-)$ system from $(\omega \rightarrow \pi^+\pi^-\pi^o)$. The kinematic fit which constrains the missing mass to a neutron would then shift the ω-peak to a lower mass and the decay kinematics would lead to a broad $(\pi^+\pi^-)$ peak. However, this possibility can be ruled out since the unconstrained missing mass distribution at 3 BeV/c has a narrow neutron peak with very few events beyond the $(m_n + m_{\pi^o})$ mass. In addition, the 5 BeV/c data does not necessitate this enhancement even though the unconstrained missing mass distribution has a broader peak at the neutron mass (Fig. 13).

The 5 BeV/c data (Fig. 30) is fitted well with the addition of two Breit-Wigner enhancements -- one at a mass $m_1 \sim 935$ MeV and $\Gamma_1 \sim 40$ MeV and another at a mass $m_2 \sim 1030$ MeV and $\Gamma_2 \sim 25$ MeV. The enhancement at 935 MeV[32] is statistically significant since the peak is ~ 5 standard derivations away from the contributions due to the ρ^o and background. It is very unlikely that this enhancement can arise from

$\eta' \to \pi^+\pi^-\gamma$ since the observed width is quite narrow and the cross-section is too large compared to the existing data on η'. The enhancement at the dipion mass ~ 1030 MeV is on the border line of being significant -- ~ 3 standard derivations away from the rest of the contributions.[33]

The small signals from these enhancements make it hard to determine their spins and parities from the details of the angular distribution. However, the significant contribution to the central cos $\theta_{\pi\pi}$ region from events around these dipion mass regions indicate that they must be in an even angular momentum state.

The fits with Function III(b) indicate a consistent difference in the widths of the ρ^o between the 3 and 5 BeV/c data for all the ranges in $|t|$. (See Table VII.) This is very likely to be due to poor assumptions on the shape of the background and due to the fact that it has been added incoherently. The $e^+e^- \to \pi^+\pi^-$ experiments[4] give much lower values for the mass and width of the ρ^o and this implies that the initial and final state strong interactions tend to alter the shape of the ρ^o resonance.

We have also tried fits (Functions V) which include interferences between the ω^o, ρ^o and background as proposed by S. Flatte.[34] Here also we have added incoherently an additional Breit-Wigner enhancement (Function V(b)). The fits to the 3 BeV/c data (Fig. 31) improve considerably <u>even when the ω^o is not included</u>, indicating that there is a strong interference of the ρ^o with the background (see Table VIII). The improvement in the fits to the 5 BeV/c data (Fig. 32) is not significant. The values for the ρ^o mass at 3 BeV/c are significantly higher as compared to the fits using functions III. The fitted widths of the ρ^o

are however still different between the 3 and 5 BeV/c data. Since our estimated resolution at the ω^o mass is poor (~ 22.5 MeV), the addition of the $\omega^o(m_{\omega^o} = 783.4$ MeV, $\Gamma_{\omega^o} = 12.7$ MeV) does not improve the fits significantly (Figs. 33 and 34) and the errors on the ω-contribution are quite large (Table IX). (The unweighted data indicates that the $\omega \to \pi^+\pi^-$ contribution is higher at larger $|t|$ values). Due to a lack of knowledge of the coherence factors between the ρ^o and ω^o, we can only obtain lower limits on the branching ratio $R=\omega(\pi^+\pi^-)/(\omega \to \pi^+\pi^-\pi^o)$. As pointed out in Reference 34, the representation (Function V) allows any degree of coherence among the amplitudes due to the background, ρ^o and ω^o. We estimate the cross-section for $\omega \to \pi^+\pi^-\pi^o$ from the results of Miller, et al.,[35] at 2.7 BeV/c for the reaction

$$\pi^+ n \to \omega^o p$$

and the empirical results of Morrison, et al.,[36] on the variation of cross-section with incident momenta. We assume $\sigma_\omega \sim (p/p_o)^{-1.5}$ and the values obtained at 3 and 5 BeV/c are listed in Table X. The branching ratios R so obtained are listed in Table IX. The systematic errors on R are expected to be large due to the poor estimation of $(\omega \to \pi^+\pi^-\pi^o)$ cross-section and our dipion mass resolution function at the ω-mass.

V. CONCLUSIONS

We have presented results from a preliminary analysis of our data on the dipion system in the mass range 280 MeV to 1100 MeV produced in the $\pi^- p$ collisions at incident momenta of 3 and 5 BeV/c. The details of the angular distributions indicate that the predictions for the ρ^o differential cross-section based on the one pion exchange model of Gottfried and Jackson agree well with the experiment. However, the behaviour of the density matrix elements as a function of $|t|$ deviates considerably from the predictions of this model. Our values for the density matrix elements have much smaller errors but differ considerably from earlier results, particularly at 3 BeV/c. We do not believe that systematic effects in our case can account for the difference. The forward-backward ratios and the crude S-wave (Isospin T=0) phase shifts derived from these ratios agree well with earlier results and reveal a strong interference between the ρ^o amplitude and the S-wave amplitude for dipion masses in the range 400-900 MeV.

The dipion mass distributions below 1100 MeV indicate enhancements <u>in addition to the ρ^o resonance</u>. The fits at 3 BeV/c necessitate an enhancement at a mass $m_o \sim 645.86 \pm 8.54$ MeV with a full width at half maximum $\Gamma_o \sim 304.59 \pm 18.34$ MeV. (See Table VIIA. Values quoted are for $|t| \leq 0.4$.) There has been evidence of a structure in this mass range in earlier experiments.[31] The $\pi\pi$-phase shift analyses (which do not include effects due to kinematic reflections from cross channels) also indicate a wide enhancement around this mass range. At 5 BeV/c we do not observe an enhancement in this mass range. The fits to the 5 BeV/c data necessitate two enhancements in addition to the ρ^o resonance -- one at a

resolution, large statistics experiment to study the reaction

$$\pi^- p \rightarrow \begin{matrix}\rho \\ \omega\end{matrix} + n$$
$$\hookrightarrow e^+e^-$$
$$\text{or } \mu^+\mu^- .$$

since the final state leptons do not strongly interact with the nucleon we should obtain better quantitative agreement with the predictions of the absorption model; one can hope to get more details of the ω-ρ interference mechanism as well.

mass $m_1 \sim 936 \pm 4.06$ MeV with a full width at half maximum $\Gamma_1 \sim 47.64 \pm 18.64$ MeV[32] and another at a mass $m_2 \sim 1029.60 \pm 5.37$ MeV with a full width at half maximum $\Gamma_2 \sim 27.67 \pm 18.38$ MeV.[33] (See Table VII A. Values quoted are for $|t| \leq 0.4$.) On the basis of the observed width and cross-section for the enhancement at ~ 930 MeV we can confidently exclude the possibility that this enhancement is a misidentified dipion state from 3-body decays of $\eta' \rightarrow \pi^+\pi^-\gamma$.[38] The enhancement at 930 MeV is statistically significant while the enhancement at 1030 MeV[33] is on the border line of being significant. Since the enhancements are small we cannot clearly determine their spins and parities. The significant contribution to the angular distribution around $\cos\theta_{\pi\pi} \sim 0$ from events in the mass region around these three enchancements suggests that they must be in an even angular momentum state.

We have also tried to estimate the lower limit for branching ratio $R = \frac{(\omega \rightarrow \pi^+\pi^-)}{(\omega \rightarrow \pi^+\pi^-\pi^0}$ on the basis of the ω-ρ interference model. In this model the mass values obtained for the ρ^0 at 3 and 5 BeV/c agree well – $m_{\rho^0} = 788.27 \pm 2.09$ MeV at 3 BeV/c and $m_{\rho^0} = 791.63 \pm 1.62$ MeV at 5 BeV/c. The widths are however still different - $\Gamma_{\rho^0} = 157.96 \pm 4.76$ at 3 BeV/c and 183.79 ± 4.03 at 5 BeV/c. (See Table VIII. Values for $|t| \leq 0.4$ are quoted here.) The masses and widths are much higher than the values obtained from $e^+e^- \rightarrow \pi^+\pi^-$ experiments.

The analysis of the data at 4 and 4.5 BeV/c incident momenta, now under progress, should reveal more details of the ππ interaction and substantiate the results at 3 and 5 BeV/c. The presence of ω-ρ interference effects as well as the lack of quantitative agreement between the absorption model and our results lends strong support to a high

ACKNOWLEDGMENTS

It is an immense pleasure to thank all the people who helped on this experiment. It is next to impossible to convey within a few lines my gratitude to all of them for their continued help and encouragement. I thank Professor Leroy T. Kerth, my research adviser, for his help throughout the experiment. Drs. W. A. Wenzel, A. R. Clark, T. Elioff, and Bruce Cork offered a good deal of time and effort over a rather long period of time. I am thankful to all of them for their patience and constant encouragement. The discussions and critical comments from Dr. W. A. Wenzel and Dr. Alan R. Clark were very valuable. I thank Dr. Clive Field for critical comments on the manuscript.

I thank Professor L. B. Loeb, my faculty adviser, for his suggestions and advice during my course-work in the graduate school.

It is hard to imagine the beginnings of this experiment - let alone its completion - without the skills of the Lofgren technical staff (especially Fred Goozen, Daniel R. George and G. L. Schnurmacher), the various Engineering and Technical support groups at LRL, the members of the Computer programming group (especially Dave Snyder, Don Zurlinden, Bob Belshe and Leo Vardas) and the Scanning group (especially Dave Perry, Fred Terwillinger, Mike Barnes and Robert Dendy). I thank all the members of the above groups for their help. My thanks to John Wilson for the beautiful format of the Tables and Figures. Murty Parupudi (now at RCA, New Jersey) helped me gain a better insight into the art of programming and I thank him immensely for the long discussions.

Two of the groups need special mention for their continued effort - the Bevatron operating crew and the Computer operations' staff. I thank the former group for the nice beam and the latter for helping me speed up the analysis stage.

I thank Dr. E. J. Lofgren, Dr. E. M. McMillan, Dr. W. A. Wenzel, Professor Leroy T. Kerth, Dr. B. V. Sreekantan and Professor M. G. K. Menon for helping me extend my stay in this country until the completion of this work.

I am indebted to Dr. B. V. Sreekantan and Professor M. G. K. Menon at the Tata Institute of Fundamental Research, India, for their continued encouragement throughout my stay here.

I thank the members of the Lawrence Radiation Laboratory, Berkeley, and the Tata Institute of Fundamental Research, India for their financial help and Senator Fulbright for Instituting the travel program.

A group of individuals in a remote corner of the world have patiently endured a good deal of discomfort during my prolonged stay here. I thank them - my parents, my sister and my brothers - with all my heart and only hope they will be a little bit happier at whatever little I might have learned here after all the time and effort.

Without the help of our highly skilled secretaries, Mrs. Peggy Fox and Mrs. Rae Nuby, this manuscript would be illegible. I thank them immensely for their help. I thank Miss Anna Mae Naranjo for all her secretarial help.

For all those not individually mentioned, I can only think of Keats in his 'Ode to a Grecian Urn' - 'Heard melodies are sweet but those unheard are sweeter'.

This work was done under the auspices of the U. S. Atomic Energy Commission.

TABLE A1

DETAILS OF SPARK CHAMBERS

	B1	B2	1	2	3	4	5
Type	Foil	Foil	Hollow Plate	←	Foam Plate	→	Hollow Plate
No. of Gaps (3/8")	4	4	4	4	4	6	4
Sensitive Area	7" x 9"	4" x 4"	16" x 60"	18" x 60"	20" x 60"	36" x 60"	48" x 96"
Material in the path of the beam per plate	← 1 mil. Al. → ($\sim 2 \times 10^{-3}$ rad. lengths)		~2 mil. Al.	←	~2 mil. Al. (Foam and Foil)	→	4 mil. Al
Gas Filling	← 90% Ne, 10% He →		← 90% Ne, 10% He + 45 ppm of Freon 12			→	90% Ne 10% He
H. V. pulse:							
Amplitude			18 kV	on all chambers			
Trigger delay			~ 320 ns				
Rise time (T_R) and			← $T_R \sim 15$ ns.			→	$T_R \sim 30$ ns.
Width T			T ~ 30 ns.				T ~ 100 ns.
Clearing Field	← 50V →		← 20V			→	100V
Location relative to center of the magnet	-124"	-68"	-30"	-10"	+10"	+52"	+140"

APPENDIX A

Quantities relevant to the design and operation system.

External proton beam (EPB) flux during the experiment	~ 3×10^{10} protons/pulse at 3 BeV/c ~ 2×10^{11} protons/pulse at 5 BeV/c
Beam spill duration	0.7 - 0.9 secs
Bevatron pulse rate	~ 10 pulses/minute
Dimensions of π^- production target at EPB focus	3" long copper 3/16" vertical, 3/8" horizontal
π^- Production angle	7°
π^- Flux during the run	~ 6×10^4 π^-'s/pulse
Momentum range used	3 - 5 BeV/c
Momentum bite	6%
π^- beam size at liquid hydrogen target	~ 95% of the beam contained in 3/4" diameter
Beam Cerenkov counter	pressurized ethylene (75 lbs/in.^{2} at 3 BeV/c, 63 lbs/in.^{2} at 5 BeV/c)
K^-/π^- ratio in the beam	$\lesssim 10^{-3}$ at 3 BeV/c, $\lesssim 10^{-5}$ at 5 BeV/c
Beam hodoscope	28 scintillation counters - each counter is 1/4" wide, 1/2" thick (along the beam), 6.75" long, viewed by 1P21 phototube.

Beam anti counter	2" dia. circular hole in 4" x 4" x 1/4" scintillator
Momentum resolution for individual beam particles	± 0.4%
Liquid hydrogen target	3" dia. 12" long centered at -45" relative to the center of M5 magnet
Target anti coincidence - TA	1/4" thick Pb sandwiched between 1/2" thick scintillators
$ES_{L,R}$	6 channel hodoscope in each half 15" x 2" x 1/8"
Spectrometer magnet M5	60" dia. pole tip, 23" gap operated at a peak field of 17 kG
Rear hodoscope RH	26 channel hodoscope; 13 counters each, above and below the median plane 18" x 4" (or 6") x 1/4"
DSA - Down stream anti-coincidence	9" x 6" x 1/8"
$\check{C}_k$ - $K^{\pm}$ Cerenkov counter	4 ft. dia., 8 ft. long counter with freon at 98 lbs/sq. in. viewed by 16 phototubes (54 AVP, 5" dia. Cathode)
Spark chambers	See Table A1
Optical demagnification	50
Overall optical distortion	0.3%
Trigger rate (2 prong events)	~ 5/pulse
No. of pictures taken	~ 1.9×10^6 (about equally divided among 3, 4, 4.5, 5 BeV/c and both polarities of M5)

No. accepted as 2 prong events after scanning	$\sim 6 \times 10^5$
No. of events satisfying ($\pi^+\pi^-$ n) hypothesis	$\sim 1.6 \times 10^5$
Nature of background on the film (i.e., in the trigger)	~ 10% multiple beam tracks in the beam chamber ~ 30% due to (≥ 1)π^0's from $p\pi^-$ ($m\pi^0$) and $n\pi^+\pi^-$ ($m\pi^0$) ~ 50% due to $p\pi^+\pi^-\pi^-$ and $n\pi^+\pi^-\pi^+\pi^-$

EFFECTIVENESS OF THE COUNTERS IN THE TRIGGER LOGIC:

$S_1 + S_2 + BH + \overline{BH} + \overline{BA} + RH + \overline{RH}$ taken as standard

Reduction factor in trigger rate due to:

DSA	~ 2.0
TA	~ 0.2
$\overline{IS}_L$, $\overline{IS}_R$	~ 0.2
$\overline{ES}_L + \overline{ES}_R$	~ 0.2
ES_L, ES_R in coincidence	~ 2.0
Overall reduction factor relative to standard	~ 4.6

(This factor varied by $\lesssim$ 10% between 3 and 5 BeV/c)

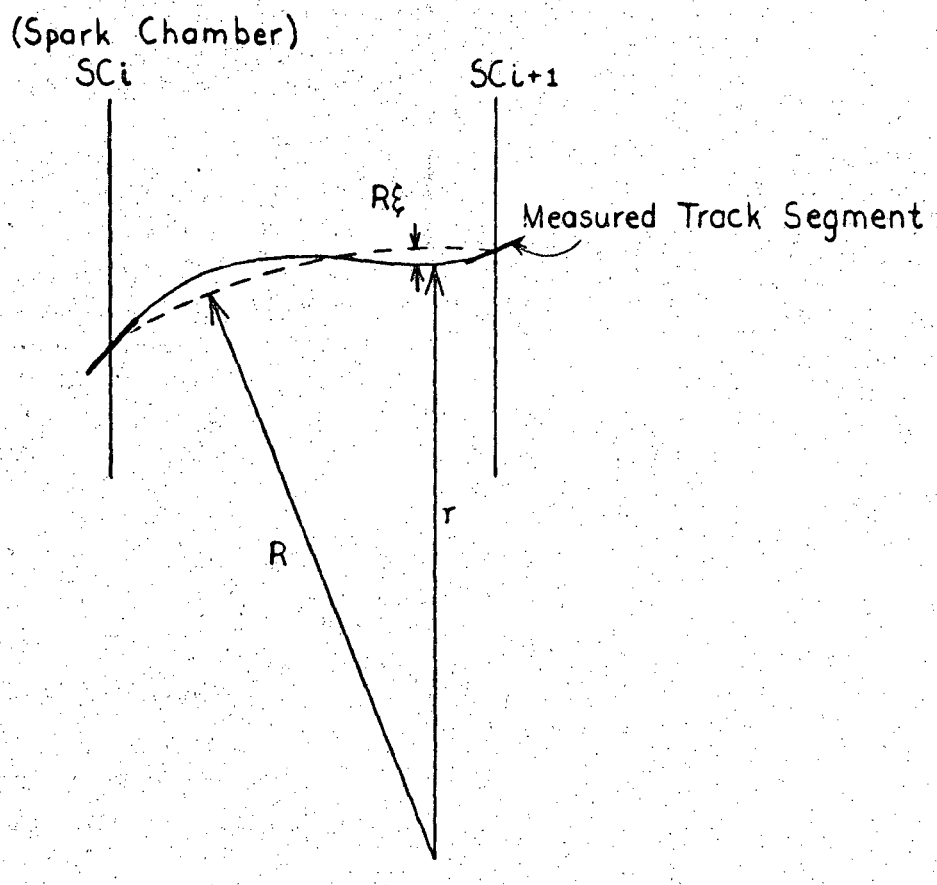

Fig. B1

APPENDIX B

Initial Guess for the Secondary Momenta

The curvature in plane polar coordinates is

$$\kappa = \frac{1}{R} = \frac{r^2 + 2r'^2 - r\,r''}{(r^2 + r'^2)^{3/2}} \tag{B1}$$

with $r' = dr/d\theta$ and $r'' = d^2r/d\theta^2$

To arrive at an initial guess for the momentum we treat the actual trajectory as a perturbation on a circular orbit in a uniform magnetic field. We choose R, the radius of the orbit, and the origin such that the circle passes through the two points we wish to fit and gives the best fit to the measured angles at these two points.

Defining (Fig. B1)

$$r = R(1 + \xi) \text{ with } \xi \ll 1$$

$$\frac{dr}{d\theta} = R\, d\xi/d\theta = R\xi'$$

$$\frac{d^2r}{d\theta^2} = R\xi''$$

If p is the momentum of the particle then

$$\kappa = -\frac{eB}{cp}$$

with the convention that the curvature is positive for electrons. Equation (B1) can now be written as

$$\kappa = -\frac{eB}{cp} \approx \frac{R^2(1 + 2\xi) + 2R^2\,\xi'^2 - R^2(1 + \xi)\,\xi''}{\left[R^2(1 + 2\xi) + R^2\,\xi'^2\right]^{3/2}}$$

$$\approx \frac{1}{R}\left[1 + 2\xi + 2\xi'^2 - (1 + \xi)\,\xi''\right]\left[1 - 3\xi - \frac{3}{2}\,\xi'^2\right]$$

$$\approx \frac{1}{R}\left[1 - \xi - \xi''\right], \text{ retaining the lowest order terms.}$$

Hence the perturbation equation to be solved is

$$\xi'' + \xi = \frac{eR}{cp} B \tag{B2}$$

with the boundary conditions

$$\left.\begin{aligned} &\xi = 0 \\ \text{and}\quad &\xi'_{\substack{a\\b}} = R \tan \psi_{\substack{a\\b}} \end{aligned}\right| \quad \text{at the end points of the arc.}$$

APPENDIX C

Determination of the Orbit Parameters for the Secondaries

The "SASS" measurements give S_{jk}, the j th coordinate at the k th spark chamber located at x_k (for j=1, 2,...5, $S_{jk} = x_k, y_k, z_k, \theta_k, \phi_k$). We need to determine the set of initial conditions $\vec{u}$ (x, y, z, θ, ϕ, p) which minimize the χ^2 - function:

$$\chi^2 \equiv \sum_{j=2}^{5} \sum_{k=1}^{L} \left(\frac{S_j(x_k) - U_{jk}(\vec{u}, x_k)}{\sigma_{jk}} \right)^2 \equiv \sum_{j=2}^{5} \sum_{k=1}^{L} \left(\frac{\Delta_{jk}}{\sigma_{jk}} \right)^2 \qquad \text{(i)}$$

where $U_{jk}(\vec{u}, x_k)$ is the predicted value at x_k for the set $\vec{u}$.

$$\frac{\partial \chi^2}{\partial u_\ell} = 0: \quad \ell = 1, 2, \ldots 6 \qquad \text{(ii)}$$

leads to

$$\sum_j \sum_k \frac{1}{\sigma_{jk}^2} \left(S_{jk} - U_{jk} \right) \frac{\partial U_{jk}}{\partial u_\ell} = 0: \quad \ell = 1, 2, \ldots 6 \qquad \text{(iii)}$$

Since U_{jk} is a non-linear function of $\vec{u}$ and x_k we use

$$U_{jk} \Big|_{\vec{u}+\delta\vec{u}} = U_{jk} \Big|_{\vec{u}} + \sum_{m=1}^{6} \frac{\partial U_{jk}}{\partial u_m} \delta u_m \qquad \text{(iv)}$$

Equation (iii) can then be written as

$$\sum_j \sum_k \sum_m \frac{1}{\sigma_{jk}^2} \frac{\partial U_{jk}}{\partial u_\ell} \delta u_m = \sum_j \sum_k \frac{1}{\sigma_{jk}^2} \frac{\partial U_{jk}}{\partial u_\ell} \Delta jk : \ell = 1, 2, \ldots 6 \qquad \text{(v)}$$

Hence the correction vector $\delta\vec{u}$ can be obtained by solving the Newton-Raphson equation

$$\boxed{\overleftrightarrow{A}\, \delta\vec{u} = \vec{f}} \qquad \text{(vi)}$$

where the matrix $\overleftrightarrow{A}$ is

$$A_{\ell m} = \sum_j \sum_k \frac{1}{\sigma_{jk}^2} \frac{\partial U_{jk}}{\partial u_\ell} \frac{\partial U_{jk}}{\partial u_m}, \qquad \text{(vii)}$$

and the vector $\overleftrightarrow{f}$ is

$$f_\ell = \sum_j \sum_k \frac{1}{\sigma_{jk}^2} \frac{\partial U_{jk}}{\partial u_\ell} \Delta_{jk} \qquad \text{(viii)}$$

We can now solve for $\delta\vec{u}$ iteratively to achieve convergence of the solution.

We also need the convariance matrix for the final set of initial conditions $\vec{u}_o$. Define the vector:

$$\vec{Y} \equiv (U_{21}, U_{22}, \ldots U_{2L}, U_{31}, \ldots U_{5,L})$$

The convariance matrix for $\vec{Y}$ is diagonal, the diagonal elements being

$$(V_y)_{kk} = \frac{1}{\sigma_k^2} \equiv \frac{1}{\sigma_{jk}^2}$$

To first order,

$$\delta\vec{Y} = \overleftrightarrow{\alpha}\,\delta\vec{u}$$

where

$$\alpha_{\ell m} = \frac{\partial Y_\ell}{\partial u_m}$$

The convariance matrix for $\vec{Y}$ is then

$$\overleftrightarrow{V}_y = \delta\vec{Y}\ \delta\vec{Y}^t = \overleftrightarrow{\alpha}\,\delta\vec{u}\,(\overleftrightarrow{\alpha}\,\delta\vec{u})^t \qquad \text{(ix)}$$

$$= \overleftrightarrow{\alpha}\,\delta\vec{u}\,\delta\vec{u}^t\ \overleftrightarrow{\alpha}^t$$

$$= \overleftrightarrow{\alpha}\ \overleftrightarrow{V}_u\ \overleftrightarrow{\alpha}^t$$

Hence the covariance matrix for $\vec{u}_o$ is

$$\overleftrightarrow{V}_u = (\overleftrightarrow{\alpha}^t\ \overleftrightarrow{V}_y^{-1}\ \overleftrightarrow{\alpha})^{-1} = \left(\sum_k \sum_j \alpha_{\ell k}\ V^{-1}_{y_{kj}}\ \alpha_{jm}\right)^{-1}$$

$$= \left(\sum_k \alpha_{\ell k}\ V^{-1}_{y_{kk}}\ \alpha_{km}\right)^{-1}, \text{ since } V_y^{-1} \text{ is diagonal}$$

$$= \left(\sum_k \frac{1}{\sigma_k^2}\ \frac{\partial Y_k}{\partial u_\ell}\ \frac{\partial Y_k}{\partial u_m}\right)^{-1} = \left(\sum_j \sum_k \frac{1}{\sigma_{jk}^2}\ \frac{\partial U_{jk}}{\partial u_\ell}\ \frac{\partial U_{jk}}{\partial u_m}\right)^{-1}$$

$$\equiv \overleftrightarrow{A}^{-1} \qquad \text{(x)}$$

Where $\overleftrightarrow{A}$ is the matrix defined in equation (vii)

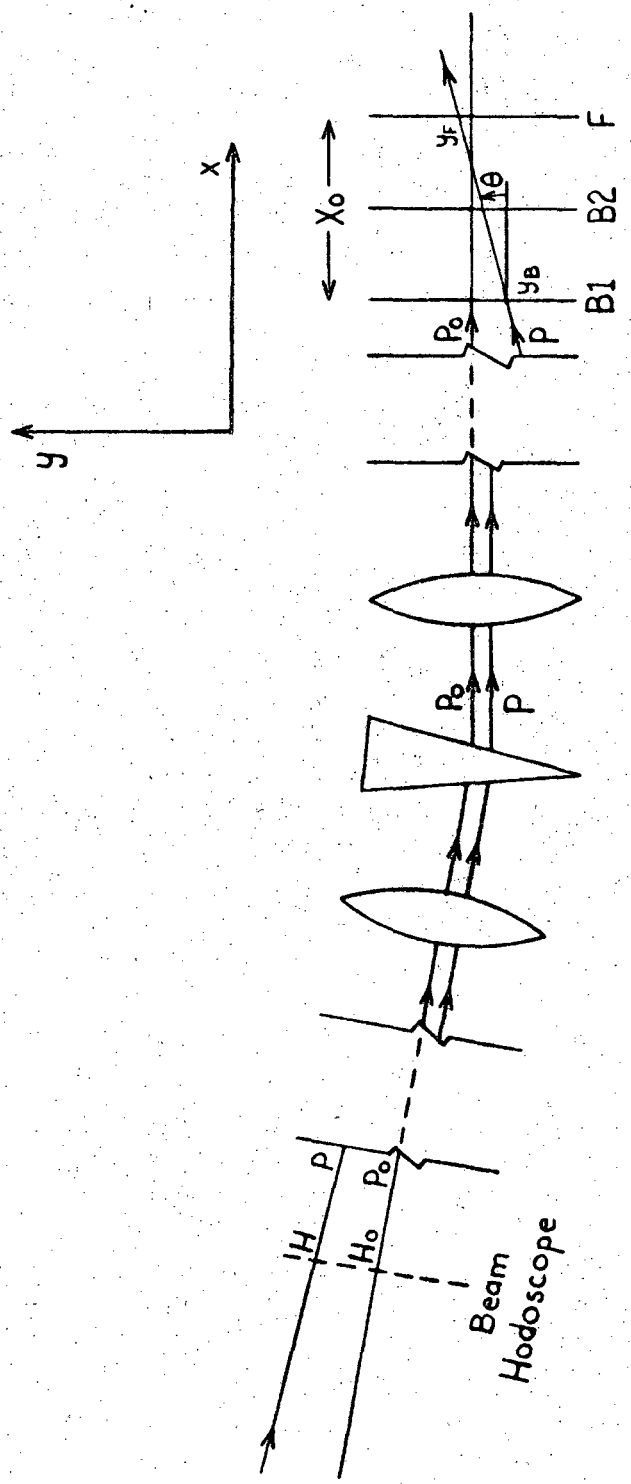

Fig. D1

APPENDIX D

Parameterization of Beam Momentum

In our beam spectrometer system the beam particle is specified by variables (y_B, θ_B, H) where (Fig. D1)

y_B = position at beam Chamber B1 exit angle

θ

H = position at beam hodoscope (digitized)

Let P_o be the momentum of the particle through H_o and travelling along the axis of the system. For a particle with momentum P the y coordinate at the focal plane in the target (for small θ) is given by

$$y_F \cong y_B + \theta \left[P \frac{dx}{dP} \left(\frac{\Delta P}{P}\right) + X_o \right] \qquad \text{(a)}$$

where $\Delta P = P - P_o$ and $\frac{dx}{dP}$ is the longitudinal dispersion (along the beam).

If the overall magnification of the beam spectrometer system is M and D the transverse dispersion then

$$y_F = M \left[H - H_o + D \frac{\Delta P}{P} \right] \qquad \text{(b)}$$

Equating (a) and (b) we have

$$\frac{\Delta P}{P} = \frac{\theta X_o + y_B - M \ (H - H_o)}{D - \theta \ P \ dx/dP}$$

or

$$P = P_o \left\{ 1 + \frac{M}{P_o \ dx/dP} \ \frac{H - H_o - \frac{1}{M}(y_B + \theta X_o)}{\theta - D/(P_o \ dx/dP)} \right\}$$

In general the central ray could be tilted relative to the axis of the downstream M5 magnet through an angle θ_o. then

$$P = P_o \left\{ 1 + \frac{M}{P_o \, dx/dP} \; \frac{H - H_o - \frac{1}{M}\left(y_B + X_o\,(\theta - \theta_o)\right)}{\theta - \theta_o - D/(P_o \, dx/dP)} \right\}$$

or

$$P \equiv P_o \left\{ 1 + A \, \frac{H - H_o' - \frac{1}{M}\left(y_B + \theta \, X_o\right)}{\theta - \theta_o'} \right\} \qquad \text{(c)}$$

If we now measure P for the individual beam tracks with the aid of the M5 magnet then, through a gradient minimization procedure, we can determine the parameters A, H_o', X_o, M, θ_o', P_o over a reasonably large sample of beam tracks. The parameters so determined along with Equation (c) will now give the beam momentum P (y_B, θ, H) for the selected events.

REFERENCES

1. H. Yukawa, Proc. Phys. Math. Soc. Japan 17, 48 (1935).
2. See Review by C. F. Powell, Reports on Progress in Physics 13, 350 (1950).
3. P. L. Csonka, CERN TH-831 (1967).
4. (a) International Symposium on Electron and Photon Interactions at High Energies. (Stanford Linear Accelerator Center, 1967).
   (b) Sixth International Conference on High Energy Accelerators (Cambridge Electron Accelerator, 1967).
   (c) V. L. Auslander, et al., Phys. Letters 25B, 433 (1967).
   (d) J. E. Augustin, et al., Phys. Letters 28B, 508 (1969); Lettre al Nuovo Cimento 2 Serie I, 214 (1969).
   (e) R. Wilson, Comments on Nuclear and Particle Physics 1, 201 (1967).
5. R. W. Birge, et al., Phys. Rev. 139B, 1600 (1965).
6. C. Goebel, Phys. Rev. Letters 1, 337 (1958).
7. (a) G. F. Chew and F. E. Low, Phys. Rev. 113, 1640 (1959).
   (b) G. F. Chew, S-matrix theory of strong interaction. (W. A. Benjamin 1961).
   (c) S. D. Drell, Rev. Mod. Phys. 33, 458 (1961), gives the historical development.
8. (a) J. P. Baton and Regnier, Nuovo Cimento 36, 1149 (1965).
   (b) L. J. Gutay, et al., Phys. Rev. Letters 18, 142 (1967).
   (c) P. B. Johnson, et al., Phys. Rev. 163, 1497 (1967).
   (d) P. E. Schlein, Phys. Rev. Letters 19, 1052 (1967).
   (e) E. Malamud and P. E. Schlein, Phys Rev. Letters 19, 1056 (1967).
   (f) A. R. Clark (Thesis) Phys. Rev. 139, B1556 (1965).
   (g) W. D. Walker, et al., Phys. Rev. Letters 18, 630 (1967).
   (h) L. B. Jones, et al., Phys. Rev. Letters 166, 1405 (1968).

REFERENCES

(i) C. F. Corbett, et al., Phys. Rev. 156, 1451 (1967).

For a nice review of the assumptions involved and the analysis procedures see:

(j) L. J. Gutay, et al., Nucl. Phys. B12, 31 (1969).

9. L. D. Jacobs (Thesis) UCRL-16877 (Aug. 1966). Particularly Table IX, p. 88 and references therein.

10. L. Durand III, and Y. T. Chiu, Phys. Rev. Letters 14, 329 (1965).

11. G. L. Schnurmacher, A. R. Clark and Leroy T. Kerth, Nucl. Inst. and Methods 61, 89 (1968).

12. B. Cork, D. R. George and T. N. Rangaswamy, Rev. Sci. Insts. 38, 221 (1967).

13. W. A. Wenzel, Focusing of Magnetic Elements for Charged Particle Beams; LRL Internal Report, Bev-834.

14. F. Solmitz, Ann. Rev. Nucl. Sci. 14, 375 (1964).

15. R. R. Bock, Kinematic Analysis of Bubble Chamber Events, CERN 61-29, Data Handling Division (1961).

16. W. A. Wenzel, Probability for Detecting a Dipion Event, LRL Internal Report, Bev-881.

17. W. A. Wenzel, Diboson Analysis - DSA, LRL Internal Report, Bev-1027.

18. W. A. Wenzel, Diboson Analysis - Rejection of Events through Detection of Recoil Neutrons, LRL Internal Report, Bev-1033.

19. M. Roos, Nucl. Phys. B2, 615 (1967); J. Pisut and M. Roos, Nucl. Phys. B6, 325 (1968).

20. R. T. Deck, Phys. Rev. Letters 13, 169 (1964): E. L. Berger, Phys. Rev. Letters 23, 1139 (1969).

21. K. Gottfried and J. D. Jackson, Nuovo Cimento 33, 309 (1964).

22. S. B. Treiman and C. N. Yang, Phys. Rev. Letters 8, 140 (1962).

REFERENCES

23. K. Gottfried and J. D. Jackson, Nuovo Cimento 34, 735 (1964); J. D. Jackson, Rev. Mod. Phys. 37, 484 (1965); also in High Energy Physics, Les Houches Lectures, p. 327 (1965), edited by C. Dewitt and M. Jacob and published by Gordon and Beach.

24. See references 23 and 8(j).

25. N. Schmitz, Nuovo Cimento 31, 255 (1964), J. Kirz, et al., Phys. Rev. 126, 763 (1963).

26. B. D. Hyams, et al., Nucl. Phys. B7, 1 (1968).

27. L. Durand and Y. T. Chiu, Phys. Rev. 139, 646 (1965).

28. N. J. Sopkovich, Nuovo Cimento 26, 186 (1962).

29. C. C. Ting, et al., Phys. Rev. Letters 9, 468 (1962); A. N. Diddens, et al., Phys. Rev. Letters 10, 262 (1963); M. L. Perl, et al., Phys. Rev. Letters 132, 1252 (1963).

30. We thank Dr. Chris Quigg (LRL, Berkeley) for letting us use his program on OPEA.

31. See Ref. 8(i).

32. B. D. Hyams,[26] et. al., find an enhancement at 946 MeV with $\Gamma \lesssim 15$ MeV.

33. D. H. Miller, et. al., Phys. Rev. Letters 21, 1489 (1968).

34. S. M. Flatte, UCRL 18687 (1969) to be published in Phys. Rev. D. Some other references for recent work on ω-ρ interference are G. Goldhaber, et. al., Phys. Rev. Letters 23, 1351 (1969).
M. Abramovich, et. al., CERN preprint CERN/D.Ph.II/Phys 70-5 (Jan. 10, 1970), to be published in Nucl. Phys.
W. W. M. Allison, et. al., Phys. Rev. Letters 24, 18 (1970).
For theoretical work on the subject, see

REFERENCES

A. S. Goldhaber et. al., Phys. Letters 30B, 249 (1969).

F. M. Renard, Nucl. Phys. B15, 118 (1970).

M. Gourdin et. al., Phys. Letters 30B, 347 (1969).

Robert G. Sachs and Gorge F. Wilkensen, The Enrico Fermi Institute and the Department of Physics, University of Chicago, Illinois, preprint COO 264-531.

35. R. J. Miller et. al., Phys. Rev. 178, 2061 (1969).

36. D. R. O. Morrison, Phys. Letters 22, 528 (1966).

37. We thank Dr. Frank Solmitz and Dr. Orin Dahl for clarifying the nature of the χ^2-distributions for various constrained fits to the kinematics.

38. Since the η' decays primarily through $\eta' \rightarrow \rho^0\gamma$ the contribution to the dipion mass range beyond 800 MeV is negligible. We thank Dr. A. Rittenberg, L.R.L., for bringing this to our attention.

TABLE IA

3 BEV/C $|t| \leq .10 (BEV/C)^2$

PIPI MASS (BEV)	R00-R11	R1-1	RE(R10)	R00 INT	R10 INT	WEIGHTED NO. OF EVENTS	F-B/F+B
.280 TO .360	-.0227	-.1069	.1391	-.0029	-.1667	206	-.0051
	(.1422)	(.0363)	(.0568)	(.0231)	(.0463)	(18)	(.0401)
.360 TO .440	.0380	-.0598	-.0509	.2420	-.1893	1458	.4191
	(.0201)	(.0145)	(.0018)	(.0022)	(.0043)	(58)	(.0037)
.440 TO .520	.0271	-.0552	-.0622	.2698	-.1581	4179	.4673
	(.0318)	(.0136)	(.0113)	(.0149)	(.0083)	(125)	(.0258)
.520 TO .560	.1593	-.0197	-.0839	.3123	-.1267	4246	.5409
	(.0317)	(.0155)	(.0138)	(.0149)	(.0088)	(154)	(.0258)
.560 TO .600	.1900	-.0688	-.1255	.2976	-.1189	6167	.5154
	(.0296)	(.0132)	(.0116)	(.0128)	(.0079)	(200)	(.0221)
.600 TO .640	.2302	-.0537	-.1407	.3261	-.1162	8059	.5648
	(.0280)	(.0114)	(.0103)	(.0111)	(.0072)	(243)	(.0192)
.640 TO .680	.2826	-.0264	-.1037	.3143	-.0781	11976	.5444
	(.0236)	(.0098)	(.0093)	(.0099)	(.0060)	(303)	(.0172)
.680 TO .720	.3300	-.0084	-.1072	.2842	-.0652	18854	.4922
	(.0199)	(.0080)	(.0075)	(.0085)	(.0048)	(389)	(.0148)
.720 TO .760	.3743	-.0010	-.0880	.2769	-.0585	27670	.4795
	(.0171)	(.0066)	(.0064)	(.0073)	(.0040)	(480)	(.0127)
.760 TO .800	.4182	.0031	-.0733	.2555	-.0524	33056	.4425
	(.0170)	(.0063)	(.0062)	(.0073)	(.0038)	(566)	(.0127)
.800 TO .840	.4656	-.0070	-.0600	.2572	-.0378	24814	.4455
	(.0193)	(.0072)	(.0076)	(.0089)	(.0044)	(509)	(.0154)
.840 TO .880	.3873	-.0169	-.0408	.2753	-.0396	12485	.4768
	(.0255)	(.0094)	(.0096)	(.0110)	(.0059)	(313)	(.0190)
.880 TO .920	.3913	-.0200	-.0256	.2578	-.0358	7564	.4465
	(.0292)	(.0106)	(.0114)	(.0132)	(.0068)	(218)	(.0228)
.920 TO .960	.2701	-.0297	-.0024	.3395	-.0308	4141	.5881
	(.0387)	(.0138)	(.0134)	(.0140)	(.0090)	(144)	(.0243)
.960 TO 1.000	.4003	-.0378	-.0321	.2146	-.0242	2694	.3718
	(.0484)	(.0179)	(.0177)	(.0219)	(.0112)	(122)	(.0380)
1.000 TO 1.040	.3787	-.0166	.0316	.0434	.0038	1839	.0752
	(.0657)	(.0241)	(.0221)	(.0296)	(.0140)	(102)	(.0513)
1.040 TO 1.080	.3351	-.0064	.0406	.0406	-.0037	1461	.0703
	(.0793)	(.0293)	(.0274)	(.0353)	(.0163)	(95)	(.0612)
1.080 TO 1.120	.1478	-.0790	-.0185	.0732	-.0467	1158	.1267
	(.1023)	(.0356)	(.0321)	(.0396)	(.0215)	(87)	(.0686)

TABLE IB

5 BEV/C $|t| \leq .10(BEV/C)^2$

PIPI MASS (BEV)	R00-R11	R1-1	RE(R10)	R00 INT	R10 INT	WEIGHTED NO. OF EVENTS	F-B/F+B
.280 TO .360	-.4638 (.1155)	.2833 (.0422)	.1905 (.0553)	.1651 (.0635)	-.2029 (.0122)	37 (8)	.2860 (.1100)
.360 TO .440	-.0198 (.0155)	-.0345 (.0538)	-.0314 (.0115)	.1911 (.0087)	-.1342 (.0258)	266 (25)	.3310 (.0151)
.440 TO .520	.1274 (.0737)	-.0238 (.0360)	-.0816 (.0229)	.2856 (.0360)	-.1599 (.0246)	784 (50)	.4947 (.0623)
.520 TO .560	.0844 (.0182)	-.0075 (.0251)	-.1179 (.0224)	.3507 (.0067)	-.1315 (.0057)	771 (50)	.6074 (.0117)
.560 TO .600	.2972 (.0602)	.0054 (.0259)	-.1016 (.0231)	.3254 (.0257)	-.0786 (.0160)	970 (65)	.5636 (.0445)
.600 TO .640	.3947 (.0468)	-.0035 (.0271)	-.1332 (.0491)	.3372 (.0439)	-.0855 (.0211)	1610 (104)	.5841 (.0760)
.640 TO .680	.4736 (.0382)	-.0080 (.0143)	-.1169 (.0146)	.3142 (.0178)	-.0771 (.0093)	2421 (120)	.5442 (.0308)
.680 TO .720	.4777 (.0294)	-.0304 (.0113)	-.1594 (.0115)	.2674 (.0149)	-.0838 (.0072)	4264 (166)	.4631 (.0258)
.720 TO .760	.5413 (.0236)	.0191 (.0090)	-.1321 (.0091)	.2728 (.0124)	-.0573 (.0053)	6623 (214)	.4725 (.0215)
.760 TO .800	.5399 (.0234)	.0254 (.0088)	-.1196 (.0092)	.2556 (.0126)	-.0499 (.0051)	7368 (229)	.4427 (.0218)
.800 TO .840	.5312 (.0279)	.0302 (.0104)	-.0770 (.0109)	.2383 (.0149)	-.0399 (.0061)	6068 (209)	.4127 (.0258)
.840 TO .880	.4932 (.0348)	.0290 (.0129)	-.0598 (.0136)	.2650 (.0174)	-.0456 (.0077)	4260 (173)	.4590 (.0301)
.880 TO .920	.3771 (.0466)	.0286 (.0177)	-.0220 (.0170)	.2648 (.0218)	-.0370 (.0106)	2930 (140)	.4587 (.0377)
.920 TO .960	.3171 (.0472)	.0202 (.0181)	-.0353 (.0173)	.3130 (.0215)	-.0392 (.0113)	2689 (131)	.5421 (.0373)
.960 TO 1.000	.5428 (.0557)	.0194 (.0215)	-.0069 (.0202)	.2921 (.0266)	-.0104 (.0129)	1778 (113)	.5059 (.0461)
1.000 TO 1.040	.6030 (.0604)	-.0245 (.0227)	-.0110 (.0276)	.1183 (.0363)	-.0298 (.0141)	1561 (110)	.2050 (.0629)
1.040 TO 1.080	.4532 (.0775)	.0156 (.0300)	-.0066 (.0301)	.1680 (.0394)	-.0196 (.0172)	1240 (97)	.2910 (.0683)
1.080 TO 1.120	.4679 (.0733)	-.0196 (.0290)	-.0735 (.0289)	.1053 (.0391)	-.0137 (.0172)	997 (74)	.1823 (.0678)

Table I C

$m_{\pi\pi}$ (BeV)	δ_0^0 (degress) †			
	3 BeV/c, $\lvert t\rvert$ <0.1		5 BeV/c, $\lvert t\rvert$ <0.1	
	Set I	Set II	Set I	Set II
0.36 → 0.44	15.20 (0.12)	1.03 (0.12)	21.87 (0.42)	0.90 (0.42)
0.44 → 0.52	32.92 (0.19)	3.14 (0.19)	34.39 (0.42)	3.81 (0.42)
0.52 → 0.56	44.33 (0.34)	6.77 (0.34)	42.86 (0.51)	8.14 (0.51)
0.56 → 0.60	57.20 (0.45)	9.18 (0.45)	56.69 (0.88)	11.60 (0.89)
0.60 → 0.64	63.17 (0.49)	14.91 (0.50)	64.33 (0.96)	17.49 (1.00)
0.64 → 0.68	73.73 (0.67)	20.80 (0.73)	75.87 (1.32)	23.05 (1.49)
0.68 → 0.72	86.78 (0.88)	27.56 (1.15)	91.19 (1.69)	27.78 (2.37)
0.72 → 0.76	98.15 (1.26)	41.02 (1.93)	100.14 (2.24)	42.04 (3.53)
0.76 → 0.80	116.83 (2.34)	54.87 (2.96)	116.61 (3.98)	54.68 (5.1)
0.80 → 0.84	132.10 (3.49)	69.99 (2.17)	133.61 (5.07)	64.50 (3.77)
0.84 → 0.88	140.62 (2.73)	82.49 (1.79)	139.37 (5.04)	78.38 (3.12)
0.88 → 0.92	150.73 (2.47)	85.09 (1.66)	146.79 (4.57)	83.88 (3.02)
0.92 → 0.96	144.80 (1.58)	103.03 (1.37)	145.19 (3.02)	96.03 (2.43)
0.96 → 1.00	162.53 (3.29)	86.44 (2.20)	152.18 (3.38)	94.99 (2.67)
1.00 → 1.04	176.83 (19.17)	68.48 (3.45)	170.39 (9.87)	74.29 (4.10)
1.04 → 1.08	177.34 (22.05)	70.53 (4.03)	167.64 (6.82)	82.66 (4.00)
1.08 → 1.12	175.64 (12.56)	76.19 (4.32)	172.88 (9.86)	77.07 (4.20)

† Note: $\delta_0^0 \pm n\pi$ are also solutions

TABLE IIA

3 BEV/C $|t| \leq .20 (BEV/C)^2$

PIPI MASS (BEV)	R00-R11	R1-1	RE(R10)	R00 INT	R10 INT	WEIGHTED NO. OF EVENTS	F-B/F+B
.280 TO .360	.0395 (.0552)	-.0852 (.0171)	.1159 (.0141)	-.0057 (.0236)	-.1704 (.0071)	263 (21)	-.0098 (.0409)
.360 TO .440	.0334 (.0369)	-.0644 (.0207)	-.0381 (.0270)	.1978 (.0295)	-.1955 (.0153)	2074 (76)	.3425 (.0510)
.440 TO .520	.0091 (.0243)	-.0578 (.0133)	-.0555 (.0098)	.2422 (.0116)	-.1592 (.0076)	6150 (158)	.4196 (.0200)
.520 TO .560	.1002 (.0272)	-.0244 (.0160)	-.0806 (.0120)	.2777 (.0130)	-.1320 (.0084)	6020 (184)	.4810 (.0226)
.560 TO .600	.1155 (.0251)	-.0734 (.0136)	-.1049 (.0104)	.2906 (.0111)	-.1180 (.0078)	8760 (239)	.5033 (.0192)
.600 TO .640	.1718 (.0228)	-.0534 (.0118)	-.1464 (.0089)	.2934 (.0099)	-.1197 (.0067)	12000 (303)	.5081 (.0171)
.640 TO .680	.1814 (.0201)	-.0375 (.0102)	-.1171 (.0083)	.2780 (.0088)	-.0921 (.0058)	17851 (382)	.4815 (.0152)
.680 TO .720	.2513 (.0171)	-.0170 (.0081)	-.1175 (.0067)	.2549 (.0075)	-.0769 (.0046)	28819 (503)	.4416 (.0129)
.720 TO .760	.2806 (.0148)	-.0026 (.0068)	-.1050 (.0057)	.2543 (.0063)	-.0736 (.0038)	42289 (620)	.4404 (.0109)
.760 TO .800	.2902 (.0149)	.0030 (.0066)	-.0872 (.0056)	.2358 (.0063)	-.0657 (.0037)	49725 (703)	.4084 (.0109)
.800 TO .840	.3047 (.0179)	-.0094 (.0078)	-.0632 (.0071)	.2312 (.0076)	-.0550 (.0045)	36146 (605)	.4004 (.0132)
.840 TO .880	.3050 (.0222)	-.0144 (.0093)	-.0320 (.0088)	.2430 (.0094)	-.0518 (.0055)	18586 (376)	.4209 (.0162)
.880 TO .920	.2670 (.0255)	-.0268 (.0104)	-.0154 (.0102)	.2344 (.0110)	-.0527 (.0063)	11455 (262)	.4059 (.0190)
.920 TO .960	.2180 (.0314)	-.0226 (.0125)	.0074 (.0114)	.3135 (.0121)	-.0448 (.0077)	7337 (204)	.5430 (.0210)
.960 TO 1.000	.3616 (.0394)	-.0394 (.0152)	-.0145 (.0152)	.1850 (.0184)	-.0332 (.0092)	5111 (182)	.3205 (.0318)
1.000 TO 1.040	.4293 (.0464)	-.0143 (.0181)	.0196 (.0178)	.0180 (.0232)	-.0245 (.0101)	3888 (166)	.0312 (.0401)
1.040 TO 1.080	.3943 (.0550)	-.0176 (.0207)	.0255 (.0211)	.0389 (.0267)	-.0315 (.0115)	3093 (151)	.0674 (.0462)
1.080 TO 1.120	.4205 (.0594)	-.0676 (.0213)	.0188 (.0220)	.0999 (.0274)	-.0320 (.0126)	2807 (147)	.1731 (.0474)

TABLE IIB

5 BEV/C $|t| \leq .20(BEV/C)^2$

PIPI MASS (BEV)	R00-R11	R1-1	RE(R10)	R00 INT	R10 INT	WEIGHTED NO. OF EVENTS	F-B/F+B
.280 TO .360	-.4258 (.0472)	.3821 (.0732)	.2127 (.0233)	.1876 (.0295)	-.2088 (.0090)	50 (10)	.3249 (.0511)
.360 TO .440	-.0810 (.0045)	-.0444 (.0528)	-.0391 (.0330)	.1453 (.0081)	-.1496 (.0273)	311 (27)	.2516 (.0140)
.440 TO .520	.0590 (.0532)	-.0337 (.0263)	-.0880 (.0199)	.2502 (.0258)	-.1619 (.0150)	915 (50)	.4334 (.0447)
.520 TO .560	.0042 (.0416)	-.0317 (.0280)	-.1487 (.0225)	.3116 (.0013)	-.1403 (.0171)	980 (57)	.5397 (.0022)
.560 TO .600	.1837 (.0615)	-.0367 (.0258)	-.1416 (.0223)	.2792 (.0296)	-.1006 (.0145)	1241 (72)	.4835 (.0513)
.600 TO .640	.2970 (.0400)	-.0187 (.0165)	-.1603 (.0027)	.3047 (.0022)	-.0991 (.0106)	1991 (94)	.5277 (.0037)
.640 TO .680	.4034 (.0328)	-.0159 (.0140)	-.1479 (.0125)	.2992 (.0154)	-.0862 (.0085)	3276 (131)	.5183 (.0267)
.680 TO .720	.3819 (.0265)	-.0300 (.0113)	-.1772 (.0098)	.2552 (.0127)	-.0955 (.0068)	5557 (178)	.4420 (.0219)
.720 TO .760	.4766 (.0218)	.0230 (.0091)	-.1489 (.0078)	.2509 (.0109)	-.0641 (.0050)	8613 (230)	.4345 (.0189)
.760 TO .800	.4801 (.0211)	.0332 (.0085)	-.1272 (.0080)	.2413 (.0108)	-.0536 (.0048)	10138 (260)	.4179 (.0186)
.800 TO .840	.4718 (.0248)	.0320 (.0098)	-.0984 (.0096)	.2380 (.0126)	-.0520 (.0056)	8334 (242)	.4123 (.0217)
.840 TO .880	.4872 (.0292)	.0329 (.0113)	-.0713 (.0115)	.2650 (.0142)	-.0534 (.0065)	6327 (216)	.4589 (.0246)
.880 TO .920	.3817 (.0383)	.0300 (.0151)	-.0379 (.0144)	.2720 (.0180)	-.0498 (.0090)	4368 (178)	.4710 (.0311)
.920 TO .960	.3506 (.0397)	.0279 (.0155)	-.0461 (.0147)	.3117 (.0181)	-.0461 (.0094)	3979 (171)	.5399 (.0314)
.960 TO 1.000	.5435 (.0441)	.0119 (.0173)	-.0305 (.0179)	.2828 (.0225)	-.0315 (.0106)	2791 (149)	.4898 (.0389)
1.000 TO 1.040	.6451 (.0457)	-.0151 (.0178)	-.0331 (.0217)	.1275 (.0285)	-.0315 (.0109)	2617 (152)	.2209 (.0494)
1.040 TO 1.080	.4674 (.0636)	.0083 (.0249)	-.0321 (.0252)	.1570 (.0327)	-.0351 (.0143)	1974 (130)	.2720 (.0566)
1.080 TO 1.120	.5183 (.0552)	-.0230 (.0222)	-.1056 (.0226)	.1490 (.0307)	-.0326 (.0135)	1579 (97)	.2581 (.0532)

TABLE IIIA

3 BEV/C $|t| \leq .40 (BEV/C)^2$

PIPI MASS (BEV)	R00-R11	R1-1	RE(R10)	R00 INT	R10 INT	WEIGHTED NO. OF EVENTS	F-B/F+B
.280 TO .360	.0414 (.0543)	-.0804 (.0197)	.1034 (.0160)	-.0240 (.0252)	-.1817 (.0145)	341 (26)	-.0416 (.0436)
.360 TO .440	.0284 (.0334)	-.0699 (.0186)	-.0361 (.0137)	.1741 (.0178)	-.1996 (.0101)	2583 (88)	.3016 (.0308)
.440 TO .520	.0192 (.0235)	-.0574 (.0135)	-.0639 (.0093)	.2199 (.0109)	-.1529 (.0073)	7584 (184)	.3808 (.0188)
.520 TO .560	.1017 (.0257)	-.0173 (.0157)	-.0728 (.0111)	.2729 (.0123)	-.1311 (.0082)	7391 (211)	.4727 (.0212)
.560 TO .600	.1072 (.0236)	-.0656 (.0139)	-.0979 (.0099)	.2748 (.0107)	-.1118 (.0077)	10684 (273)	.4760 (.0185)
.600 TO .640	.1249 (.0217)	-.0423 (.0125)	-.1307 (.0086)	.2791 (.0096)	-.1164 (.0068)	14135 (336)	.4835 (.0166)
.640 TO .680	.1262 (.0193)	-.0264 (.0109)	-.0935 (.0080)	.2574 (.0085)	-.0910 (.0059)	21245 (427)	.4458 (.0148)
.680 TO .720	.1696 (.0169)	-.0003 (.0088)	-.0956 (.0067)	.2394 (.0072)	-.0767 (.0047)	33495 (557)	.4146 (.0125)
.720 TO .760	.1929 (.0147)	.0116 (.0074)	-.0896 (.0056)	.2347 (.0061)	-.0748 (.0039)	49575 (696)	.4065 (.0106)
.760 TO .800	.2094 (.0146)	.0166 (.0071)	-.0782 (.0055)	.2199 (.0061)	-.0676 (.0038)	59316 (806)	.3810 (.0105)
.800 TO .840	.2381 (.0174)	-.0013 (.0083)	-.0563 (.0069)	.2159 (.0073)	-.0594 (.0045)	43742 (702)	.3739 (.0127)
.840 TO .880	.2495 (.0214)	-.0054 (.0097)	-.0311 (.0084)	.2291 (.0089)	-.0591 (.0055)	22381 (430)	.3968 (.0154)
.880 TO .920	.1977 (.0245)	-.0205 (.0110)	-.0053 (.0099)	.2170 (.0104)	-.0595 (.0064)	13598 (293)	.3759 (.0180)
.920 TO .960	.1380 (.0293)	-.0168 (.0134)	.0196 (.0111)	.2760 (.0120)	-.0541 (.0078)	8863 (229)	.4781 (.0208)
.960 TO 1.000	.2742 (.0378)	-.0387 (.0162)	.0095 (.0149)	.1592 (.0171)	-.0352 (.0093)	6265 (201)	.2757 (.0297)
1.000 TO 1.040	.3435 (.0459)	-.0122 (.0191)	.0411 (.0172)	.0024 (.0218)	-.0290 (.0103)	4684 (183)	.0041 (.0377)
1.040 TO 1.080	.2942 (.0548)	-.0140 (.0219)	.0499 (.0205)	.0231 (.0254)	-.0402 (.0118)	3737 (168)	.0400 (.0439)
1.080 TO 1.120	.2977 (.0609)	-.0708 (.0228)	.0384 (.0220)	.0729 (.0266)	-.0392 (.0130)	3377 (164)	.1263 (.0460)

TABLE IIIB

5 BEV/C $|t| \leq .40 (BEV/C)^2$

PIPI MASS (BEV)	R00-R11	R1-1	RE(R10)	R00 INT	R10 INT	WEIGHTED NO. OF EVENTS	F-B/F+B
.280 TO .360	-.5092 (.0453)	.4563 (.0269)	.2385 (.0447)	.2294 (.0257)	-.2029 (.0067)	55 (10)	.3974 (.0446)
.360 TO .440	-.1494 (.0106)	-.0681 (.0512)	-.0313 (.0314)	.1137 (.0072)	-.1579 (.0258)	351 (28)	.1969 (.0124)
.440 TO .520	.0279 (.0504)	-.0583 (.0256)	-.0941 (.0188)	.2387 (.0240)	-.1697 (.0143)	1024 (53)	.4134 (.0416)
.520 TO .560	-.0060 (.0056)	-.0492 (.0192)	-.1434 (.0046)	.2765 (.0018)	-.1405 (.0053)	1081 (58)	.4789 (.0031)
.560 TO .600	.1531 (.0683)	-.0535 (.0264)	-.1504 (.0236)	.2659 (.0363)	-.1018 (.0144)	1401 (77)	.4605 (.0629)
.600 TO .640	.2340 (.0454)	-.0271 (.0203)	-.1660 (.0176)	.2690 (.0222)	-.0968 (.0115)	2211 (102)	.4659 (.0385)
.640 TO .680	.3725 (.0313)	-.0159 (.0142)	-.1533 (.0120)	.2806 (.0149)	-.0885 (.0084)	3746 (138)	.4860 (.0259)
.680 TO .720	.3659 (.0248)	-.0297 (.0112)	-.1843 (.0092)	.2468 (.0119)	-.0960 (.0065)	6417 (189)	.4275 (.0206)
.720 TO .760	.4494 (.0215)	.0246 (.0094)	-.1478 (.0077)	.2299 (.0106)	-.0633 (.0050)	9747 (239)	.3982 (.0184)
.760 TO .800	.4279 (.0215)	.0406 (.0091)	-.1287 (.0079)	.2185 (.0105)	-.0540 (.0049)	11073 (263)	.3785 (.0182)
.800 TO .840	.4246 (.0251)	.0383 (.0103)	-.0892 (.0095)	.2215 (.0121)	-.0545 (.0057)	9143 (244)	.3837 (.0210)
.840 TO .880	.4463 (.0292)	.0420 (.0118)	-.0725 (.0111)	.2472 (.0137)	-.0566 (.0065)	6986 (218)	.4281 (.0238)
.880 TO .920	.3055 (.0379)	.0297 (.0159)	-.0345 (.0144)	.2510 (.0177)	-.0522 (.0093)	4766 (178)	.4347 (.0306)
.920 TO .960	.3261 (.0379)	.0249 (.0157)	-.0417 (.0146)	.2901 (.0181)	-.0518 (.0093)	4456 (177)	.5025 (.0313)
.960 TO 1.000	.5225 (.0434)	.0171 (.0178)	-.0379 (.0177)	.2646 (.0224)	-.0316 (.0104)	3109 (157)	.4584 (.0387)
1.000 TO 1.040	.6146 (.0462)	-.0095 (.0184)	-.0237 (.0210)	.1096 (.0276)	-.0360 (.0108)	3009 (164)	.1898 (.0478)
1.040 TO 1.080	.4768 (.0598)	.0182 (.0237)	-.0347 (.0236)	.1342 (.0312)	-.0413 (.0132)	2354 (145)	.2324 (.0540)
1.080 TO 1.120	.5296 (.0510)	-.0234 (.0211)	-.1163 (.0210)	.1478 (.0287)	-.0344 (.0125)	1891 (109)	.2560 (.0497)

TABLE IVA

3 BEV/C PIPI MASS (0.68,0.84) BEV

-T (BEV/C)^2	R00-R11	R1-1	RE(R10)	RCC INT	R10 INT	DSIG/DT (mb)	F-B/F+B
0. TO .020	.3711 (.0236)	-.0029 (.0083)	-.0520 (.0076)	.2905 (.0094)	-.0287 (.0051)	7.3646 (.1658)	.5031 (.0163)
.020 TO .060	.4370 (.0117)	.0009 (.0044)	-.0995 (.0043)	.2813 (.0051)	-.0552 (.0027)	7.4248 (.0942)	.4872 (.0089)
.060 TO .100	.3557 (.0163)	-.0172 (.0071)	-.1089 (.0067)	.2420 (.0072)	-.0725 (.0041)	4.1474 (.0704)	.4191 (.0125)
.100 TO .140	.2988 (.0216)	-.0300 (.0111)	-.0750 (.0101)	.2336 (.0095)	-.0861 (.0061)	2.4519 (.0550)	.4047 (.0165)
.140 TO .180	.4083 (.0261)	-.0751 (.0141)	-.0786 (.0141)	.2174 (.0129)	-.0880 (.0081)	1.6368 (.0502)	.3765 (.0224)
.180 TO .220	.5228 (.0334)	-.0868 (.0176)	-.0485 (.0190)	.2451 (.0172)	-.0543 (.0108)	1.1139 (.0437)	.4246 (.0298)
.220 TO .300	.5799 (.0182)	.0290 (.0059)	.0568 (.0156)	.2317 (.0180)	-.0474 (.0047)	.5123 (.0189)	.4013 (.0312)
.300 TO .400	.8611 (.0122)	.1480 (.0104)	.2885 (.0243)	.1690 (.0276)	-.0523 (.0042)	.2570 (.0109)	.2928 (.0478)
.400 TO .600	.9721 (.0398)	-.1810 (.0122)	.1563 (.0079)	.1115 (.0145)	-.0702 (.0034)	.1341 (.0061)	.1931 (.0252)
.600 TO .800	.5691 (.3763)	-.3555 (.0313)	.2113 (.0059)	-.0002 (.0086)	-.0756 (.0072)	.0788 (.0170)	-.0004 (.0149)
.800 TO 1.000	.6045 (.0944)	-.8341 (.0285)	.3454 (.0103)	-.0000 (.0151)	-.1101 (.0142)	.0420 (.0048)	-0. (.0262)

TABLE IVB

5 BEV/C PIPI MASS (0.68,0.84) BEV

-T (BEV/C)^2	ROO-R11	R1-1	RE(R10)	ROO INT	R10 INT	DSIG/DT (mb)	F-B/F+B
0. TO .020	.4783 (.0272)	.0006 (.0100)	-.0879 (.0108)	.2676 (.0139)	-.0523 (.0062)	1.3799 (.0440)	.4635 (.0240)
.020 TO .060	.5657 (.0174)	.0090 (.0067)	-.1300 (.0071)	.2606 (.0097)	-.0532 (.0040)	1.4590 (.0357)	.4514 (.0160)
.060 TO .100	.5166 (.0242)	.0332 (.0098)	-.1376 (.0090)	.2590 (.0123)	-.0665 (.0054)	.8633 (.0280)	.4486 (.0213)
.100 TO .140	.5152 (.0312)	.0218 (.0135)	-.1566 (.0119)	.2433 (.0157)	-.0706 (.0075)	.5287 (.0215)	.4214 (.0273)
.140 TO .180	.5040 (.0370)	.0081 (.0164)	-.1337 (.0169)	.2366 (.0199)	-.0568 (.0095)	.3477 (.0163)	.4099 (.0345)
.180 TO .220	.5325 (.0189)	.0352 (.0081)	-.1380 (.0167)	.2004 (.0229)	-.0658 (.0041)	.2352 (.0126)	.3471 (.0396)
.220 TO .300	.6885 (.0151)	-.0064 (.0068)	-.1456 (.0155)	.1816 (.0211)	-.0505 (.0037)	.1412 (.0070)	.3145 (.0365)
.300 TO .400	.6191 (.0661)	.0261 (.0350)	-.0967 (.0292)	.1010 (.0321)	-.0379 (.0169)	.0828 (.0049)	.1749 (.0555)
.400 TO .600	.4597 (.0858)	-.0849 (.0408)	-.0504 (.0312)	.0874 (.0335)	-.0792 (.0232)	.0365 (.0025)	.1514 (.0581)
.600 TO .800	.2755 (.0275)	.1170 (.0221)	-.0556 (.0114)	.1988 (.0022)	-.1653 (.0084)	.0173 (.0019)	.3444 (.0038)
.800 TO 1.000	.5748 (.0478)	.0529 (.0394)	-.1371 (.0265)	-.1316 (.0200)	-.1691 (.0369)	.0076 (.0012)	-.2280 (.0346)

TABLE IVC

3 BEV/C PIPI MASS (0.60,0.90) BEV

-T (BEV/C)^2	R00-R11	R1-1	RE(R10)	R0C INT	R1C INT	DSIG/DT (mb)	F-B/F+B
0. TO .020	.3752 (.0195)	-.0024 (.0069)	-.0613 (.0064)	.3027 (.0078)	-.0392 (.0043)	10.1621 (.1967)	.5243 (.0136)
.020 TO .060	.3977 (.0100)	-.0089 (.0038)	-.1002 (.0037)	.2822 (.0043)	-.0600 (.0023)	9.1366 (.0974)	.4888 (.0075)
.060 TO .100	.3382 (.0135)	-.0260 (.0060)	-.1079 (.0057)	.2474 (.0060)	-.0754 (.0035)	5.2214 (.0738)	.4286 (.0105)
.100 TO .140	.3357 (.0176)	-.0420 (.0088)	-.0755 (.0083)	.2319 (.0080)	-.0867 (.0049)	3.2635 (.0605)	.4017 (.0139)
.140 TO .180	.4001 (.0229)	-.0634 (.0121)	-.0402 (.0121)	.2248 (.0109)	-.0799 (.0070)	2.0358 (.0505)	.3893 (.0189)
.180 TO .220	.5028 (.0288)	-.0587 (.0155)	-.0062 (.0159)	.2437 (.0142)	-.0665 (.0091)	1.3466 (.0422)	.4221 (.0245)
.220 TO .300	.6075 (.0105)	.0069 (.0054)	.0726 (.0055)	.2372 (.0142)	-.0566 (.0019)	.6804 (.0191)	.4108 (.0246)
.300 TO .400	.6698 (.0094)	-.0176 (.0064)	.1515 (.0093)	.1641 (.0501)	-.0483 (.0059)	.3922 (.0132)	.2841 (.0868)
.400 TO .600	.8608 (.0094)	-.2762 (.0080)	.1421 (.0044)	.1133 (.0051)	-.0722 (.0038)	.1888 (.0065)	.1963 (.0088)
.600 TO .800	.3708 (.0486)	-.2587 (.0271)	.1260 (.0124)	.0187 (.0151)	-.0804 (.0073)	.1163 (.0075)	.0323 (.0261)
.800 TO 1.000	.0720 (.0287)	-.3908 (.0257)	.2552 (.0195)	-.0103 (.0225)	-.0650 (.0106)	.0923 (.0081)	-.0178 (.0390)

TABLE IVD

5 BEV/C PIPI MASS (0.60,0.90) BEV

-T (BEV/C)^2	R00-R11	R1-1	RE(R10)	R0C INT	R10 INT	DSIG/DT (mb)	F-B/F+B
0. TO .020	.4552	.0020	-.0780	.2826	-.0535	1.9213	.4896
	(.0230)	(.0085)	(.0090)	(.0113)	(.0053)	(.0508)	(.0196)
.020 TO .060	.5320	.0127	-.1230	.2725	-.0562	1.9813	.4720
	(.0152)	(.0059)	(.0060)	(.0080)	(.0035)	(.0406)	(.0139)
.060 TO .100	.5093	.0229	-.1389	.2697	-.0730	1.1719	.4670
	(.0200)	(.0080)	(.0074)	(.0101)	(.0046)	(.0314)	(.0174)
.100 TO .140	.4878	.0197	-.1466	.2561	-.0727	.7180	.4436
	(.0259)	(.0111)	(.0101)	(.0130)	(.0063)	(.0240)	(.0225)
.140 TO .180	.4886	.0062	-.1338	.2374	-.0663	.4742	.4111
	(.0314)	(.0140)	(.0143)	(.0167)	(.0081)	(.0187)	(.0290)
.180 TO .220	.5243	.0084	-.1431	.2161	-.0731	.3447	.3743
	(.0413)	(.0212)	(.0177)	(.0207)	(.0124)	(.0156)	(.0359)
.220 TO .300	.6334	-.0184	-.1498	.1984	-.0617	.1984	.3436
	(.0360)	(.0157)	(.0157)	(.0194)	(.0096)	(.0083)	(.0336)
.300 TO .400	.5959	.0341	-.1026	.0986	-.0440	.1139	.1709
	(.0561)	(.0454)	(.0291)	(.0279)	(.0201)	(.0058)	(.0483)
.400 TO .600	.4925	-.0560	-.0393	.0517	-.0671	.0515	.0895
	(.0716)	(.0346)	(.0253)	(.0282)	(.0187)	(.0029)	(.0488)
.600 TO .800	.1805	.0073	-.1164	.1252	-.1209	.0257	.2168
	(.1180)	(.0168)	(.0081)	(.0407)	(.0073)	(.0025)	(.0705)
.800 TO 1.000	.1471	.1124	-.0681	-.0953	-.1680	.0125	-.1651
	(.1826)	(.0718)	(.0282)	(.0588)	(.0250)	(.0019)	(.1019)

TABLE V

Absorption Parameters for $\pi^- p \rightarrow \rho^o n$

P (BeV/c)	q_i (BeV/c)	q_f (BeV/c)	σ_T (mb)	A $(GeV/c)^{-2}$	C_i	γ_i
3.0	1.101	0.946	32.16	7.5	0.876	0.064
5.0	1.463	1.353	29.10	7.8	0.843	0.032

($C_f = 1$ and $\gamma_f = 3/4\ \gamma_i$ are assumed)

TABLE VI

Functions used to fit the dipion mass distributions at 3 and 5 BeV/c

I. a. $PS\left[a_o + a_1\, BW_i(m, m_1, \Gamma_1, \ell=1)\right]$ $\quad i = 0, 1, 2$

b. $PS\left[a_o + a_1\, BW_i(m, m_1, \Gamma_1, \ell=1) + a_2\, BW_i(m, m_2\, \Gamma_2, \ell=0)\right]$ $\quad i = 0, 1, 2$

II. a. $a_o + a_1 m + a_2\, BW_i(m, m_1, \Gamma_1, \ell=1)$ $\quad i = 0, 1, 2$

b. $a_o + a_1 m + a_2\, BW_i(m, m_1, \Gamma_1, \ell=1) + a_3\, BW_i(m, m_2, \Gamma_2, \ell=0)$ $\quad i = 0, 1, 2$

III. a. $a_o + a_1 m + a_2 m^2 + a_3\, BW_i(m, m_1, \Gamma_1, \ell=1)$ $\quad i = 0, 1, 2$

b. $a_o + a_1 m + a_2 m^2 + a_3\, BW_i(m, m_1, \Gamma_1, \ell=1) + a_4\, BW_i(m, m_2, \Gamma_2, \ell=0)$ $\quad i = 0, 1, 2$

c. Function III(b) $+ a_5\, BW_i(m, m_3, \Gamma_3, \ell=0)$ $\quad i = 0, 1, 2$

IV. a. $$a_o \frac{q}{D_B} \int_T^{t_{min}(m)} \exp(D_B t)\,dt + \frac{a_1}{q}\, BW_3(m, m_1, \Gamma_1, \ell=1) \int_{t_{min}(m)}^{T} \exp(D_\rho t)\,dt$$

with $D_B = 2.0(\mathrm{GeV}/c)^{-2}$, $D_\rho = 10.25(\mathrm{GeV}/c)^{-2}$ and T is the t-value at which the cut is imposed on the data. See reference 19

V. a. $$\left[a_1 + a_2 |B_\rho(m)|^2 + a_3 |B_\omega(m)|^2 + a_4\, \mathrm{Re}\, B_\rho(m) + a_5\, \mathrm{Re}\, B_\omega(m)\right] * \left[1 + a_6(m-m_\omega) + a_7\,(m-m_\omega)^2\right]$$

b. $$\left[a_1 + a_2 |B_o(m)|^2 + a_3 |B_\rho(m)|^2 + a_4 |B_\omega(m)|^2 + a_5\, \mathrm{Re}\, B_\rho(m) + a_6\, \mathrm{Re}\, B_\omega(m)\right] * \left[1 + a_7(m-m_\omega) + a_8(m-m_\omega)^2\right]$$

See reference (34)

In the above formulae:

$$PS = \frac{\pi^2 q}{E_{cm}^2} \sqrt{2(E_{cm}^2, m^2, m_n^2)}$$: is the dipion mass distribution from phase-space

$$\lambda(x, y, z) = x^2 + y^2 + z^2 - 2xy - 2yz - 2zx$$

$q = \frac{1}{2}(m^2 - 4\mu^2)^{1/2}$: is the decay momentum of each of the pions (mass μ) in the dipion rest frame

$E_{cm}^2 = \mu^2 + m_p^2 + 2E_{lab}m_p$: is the square of the c.m. energy

$$BW_o(m, m_o, \Gamma_o, \ell) = \frac{\Gamma_o}{4(m - m_o)^2 + \Gamma_o}$$: Simple non-relativistic Breit-Wigner distribution

$$BW_1(m, m_o, \Gamma_o, \ell) = \frac{m_o m\, \Gamma(m)}{(m_o^2 - m^2)^2 + m_o^2 \Gamma^2(m)}$$

with $\Gamma(m) = \Gamma_o \frac{m_o}{m} \left(\frac{q}{q_o}\right)^{2\ell+1}$

$$q_o = q\big|_{m=m_o}$$

: mass and angular momentum dependent Breit-Wigner distribution.

$$BW_2(m, m_o, \Gamma_o, \ell) = \frac{m_o m\, \Gamma_B(m)}{(m_o^2 - m^2)^2 + m_o^2\, \Gamma_B^2(m)}$$

with $\Gamma_B(m) = \Gamma(m) \left(\frac{1 + q_o^2/4\mu^2}{1 + q^2/4\mu^2} \right)^{\ell}$: Same as above but including barrier penetration factors

$$BW_3(m, m_o, \Gamma_o, \ell) = \frac{m_o^2\, m^2\, \Gamma_B^2(m)}{(m_o^2 - m^2)^2 + m_o^2\, \Gamma_B^2(m)}$$: See reference (19)

$$|B_\rho(m)|^2 = \left| \frac{m_\rho\, \Gamma_\rho^o}{(m_\rho^2 - m^2) - i m_\rho \Gamma} \right|^2 \left(\frac{q}{q_\rho} \right),$$

with $\Gamma_\rho = \Gamma_\rho^o \frac{m_\rho}{m} \left(\frac{q}{q_\rho} \right)^3$

$$|B_\omega(m)|^2 = \left| \frac{m_\omega\, \Gamma_\omega^o}{(m_\omega^2 - m^2) - i\, m_\omega \Gamma_\omega^o} \right|^2 \left(\frac{q}{q_\omega} \right)^2$$

$$|B_o(m)|^2 = \left| \frac{m_o \Gamma_o^o}{(m_o^2 - m^2 - i\, m_o \Gamma(m))} \right|^2$$

$$\mathrm{Re}\, B_\rho(m) = \frac{m_\rho \Gamma_\rho^o\, (m_\rho^2 - m^2)}{\left[(m_\rho^2 - m^2)^2 + m_\rho^2 \Gamma_\rho^2 \right]}$$ and similarly for $\mathrm{Re}\, B_\omega(m)$

TABLE VIIA

FUNCTION	P BEV/C	$\lvert t \rvert$ $(BEV/C)^2$	M_ρ (MEV)	Γ_ρ (MEV)	M_1 (MEV)	Γ_1 (MEV)	M_2 (MEV)	Γ_2 (MEV)	χ^2	D.F	†χ^2/D.F
III(B,I=2)	3.	.LT.0.10	770.53	120.86	639.98	283.39	---	---	159.69	33	4.84
			(1.21)	(3.10)	(7.74)	(14.80)	---	---			
III(B,I=2)	3.	.LT.0.22	768.68	124.37	645.52	301.17	---	---	133.79	33	4.05
			(.50)	(.64)	(8.78)	(17.96)	---	---			
III(B,I=2)	3.	.LT.0.40	770.10	123.01	645.86	304.59	---	---	142.32	33	4.31
			(.87)	(2.41)	(8.54)	(18.34)	---	---			
III(B,I=2)	5.	.LT.0.10	771.75	172.81	936.21	25.87	---	---	55.16	25	2.21
			(1.60)	(6.61)	(6.39)	(29.50)	---	---			
III(C,I=2)	5.	.LT.0.22	778.82	172.29	936.98	54.64	1029.05	25.12	34.83	29	1.20
			(1.29)	(4.19)	(4.46)	(19.18)	(5.92)	(17.47)			
III(C,I=2)	5.	.LT.0.40	774.77	172.30	936.68	47.64	1029.60	27.67	40.55	29	1.40
			(1.31)	(4.20)	(4.06)	(18.64)	(5.37)	(18.38)			

†Degrees of Freedom

Table VII B

Function	P (BeV/c)	$\lvert t \rvert$ $(BeV/c)^2$	Back-ground (%)	σ_ρ (mb)	σ_1 (mb)	σ_2 (mb)	σ_ρ/total (%)	σ_2/σ_ρ (%)	σ_3/σ_ρ (%)
III (B, i=2)	3	≤ 0.1	−6.27	0.680	0.211	–	81.15	30.95	–
			(7.21)	(0.019)	(0.016)		(2.28)	(2.40)	
"	3	≤ 0.22	−3.89	1.031	0.297	–	80.67	28.79	–
			(4.42)	(0.022)	(0.030)		(1.69)	(2.93)	
"	3	≤ 0.4	−3.58	1.211	0.370	–	79.33	30.57	–
			(4.67)	(0.035)	(0.039)		(2.24)	(3.19)	
"	5	≤ 0.1	13.67	0.756	0.019	–	84.20	2.54	–
			(6.08)	(0.026)	(0.009)		(2.92)	(1.28)	
III (C, i=2)	5	≤ 0.22	8.06	0.778	0.032	0.010	87.26	4.06	1.30
			(5.11)	(0.017)	(0.008)	(0.004)	(1.87)	(1.11)	(0.52)
"	5	≤ 0.40	9.25	0.860	0.032	0.013	86.25	3.69	1.52
			(5.34)	(0.019)	(0.008)	(0.005)	(1.87)	(1.01)	(0.61)

TABLE VIII

M_ω = 783.4 MEV Γ_ω = 12.7 MEV ESTIMATED DIPION MASS RESOLUTION AT M_ω = 22.5 MEV

P BEV/C	$\lvert t \rvert$ (BEV/C)^2		M_ρ (MEV)	Γ_ρ (MEV)	M_ϕ (MEV)	Γ_ϕ (MEV)	χ^2	D.F†	χ^2/D.F	$(d\sigma_\omega)$‡ (mb)	R X10^3
3.	.LT.0.10	ω	792.46	159.82	574.33	87.08	41.51	30	1.384	.0550	.470
			(1.55)	(3.78)	(6.45)	(13.83)				(.0795)	(.580)
		—	793.69	159.89	574.37	84.33	42.76	32	1.336		
			(.87)	(1.54)	(2.40)	(10.83)					
3.	.LT.0.22	ω	786.84	158.10	580.26	108.81	55.01	30	1.834	.2360	.669
			(2.02)	(3.90)	(13.81)	(30.36)				(.2205)	(.534)
		—	788.77	156.93	581.01	103.95	58.87	32	1.840		
			(1.00)	(.85)	(1.03)	(11.19)					
3.	.LT.0.40	ω	788.27	157.96	581.12	115.39	56.14	30	1.871	.3085	.624
			(2.09)	(4.76)	(9.86)	(25.07)				(.2100)	(.363)
		—	790.18	156.45	582.12	111.37	60.69	32	1.897		
			(.69)	(2.02)	(6.57)	(8.51)					
5.	.LT.0.10	ω	794.27	173.88	932.56	54.39	39.23	24	1.635	.2570	4.668
			(6.30)	(10.02)	(7.36)	(31.03)				(.3515)	(6.392)
		—	790.19	170.56	931.50	56.33	40.98	26	1.576		
			(4.44)	(9.16)	(7.32)	(30.91)					
5.	.LT.0.22	ω	797.34	182.89	935.17	40.54	31.13	24	1.297	.4370	2.681
			(4.20)	(7.46)	(5.60)	(29.18)				(.3890)	(2.387)
		—	792.12	179.36	933.85	44.33	34.41	26	1.323		
			(3.18)	(7.36)	(6.26)	(29.92)					
5.	.LT.0.40	ω	791.63	187.46	936.88	21.89	35.97	24	1.499	.2905	1.267
			(1.62)	(4.27)	(2.11)	(10.36)				(.0520)	(.227)
		—	787.47	183.79	936.63	20.60	38.46	26	1.479		
			(1.86)	(4.03)	(2.34)	(3.11)					

† D.F = Degrees of freedom

‡ Lower limits.

TABLE IX

P BEV/C	|T| (BEV/C)^2	A1	A2 $\|BW_\rho\|^2$	A3 $\|BW_f\|^2$	A4 $\|BW_\omega\|^2$	A5 RE BW_f	A6 RE BW_ω	A7	A8	χ^2/D.F †
3.	.LT.0.1	8.51	297.70	16240.90	144.690	-1048.94	-596.18	-4.46	7.65	1.393
		(4.21)	(49.46)	(294.00)	(582.18)	(81.90)	(430.95)	(.15)	(.52)	
		9.61	288.11	16330.90	---	-1149.75	---	-4.54	7.91	1.336
		(2.17)	(27.26)	(88.42)	---	(32.05)	---	(.09)	(.33)	
3.	.LT.0.2	5.27	442.28	23889.90	992.750	-1581.51	-1188.60	-3.81	7.98	1.835
		(13.67)	(100.00)	(402.48)	(819.76)	(114.09)	(647.12)	(.18)	(.62)	
		8.84	415.14	24329.30	---	-1778.01	---	-3.98	8.53	1.839
		(8.87)	(66.62)	(161.85)	---	(55.61)	---	(.10)	(.31)	
3.	.LT.0.4	-2.72	592.11	28452.10	1256.450	-1855.88	-1473.18	-3.85	8.23	1.871
		(14.20)	(76.45)	(510.67)	(1009.50)	(126.84)	(82.60)	(.10)	(.33)	
		1.64	561.45	29038.80	---	-2100.33	---	-4.02	8.80	1.895
		(4.27)	(60.75)	(188.91)	---	(41.09)	---	(.07)	(.31)	
5.	.LT.0.1	386.11	310.29	3164.26	.004	1509.55	376.55	3.28	2.49	1.634
		(102.10)	(65.91)	(192.02)	(.0014)	(279.46)	(257.46)	(.36)	(.75)	
		355.03	317.56	3262.35	---	1453.23	---	3.15	2.21	1.576
		(95.47)	(65.34)	(169.58)	---	(288.38)	---	(.39)	(.83)	
5.	.LT.0.2	548.98	321.49	4220.74	.004	1879.46	571.20	3.57	3.12	1.297
		(100.08)	(70.23)	(178.60)	(.0010)	(255.70)	(253.84)	(.21)	(.47)	
		507.76	328.01	4349.83	---	1807.06	---	3.46	2.89	1.323
		(96.73)	(70.95)	(164.77)	---	(271.87)	---	(.24)	(.52)	
5.	.LT.0.4	501.79	367.44	4890.83	.005	1726.97	486.90	3.31	2.57	1.498
		(42.18)	(39.15)	(67.70)	(.0001)	(109.95)	(43.45)	(.09)	(.20)	
		475.78	381.40	5001.94	---	1635.83	---	3.20	2.33	1.475
		(55.09)	(48.03)	(89.73)	---	(146.37)	---	(.17)	(.35)	

† D.F = Degrees of freedom

TABLE X

P (Bev/c)	$d\sigma\ (\pi^- p \rightarrow \omega^0 n)$ mb		
	$t \leq 0.1\ (BeV/c)^2$	$t \leq 0.22\ (BeV/c)^2$	$t \leq 0.4\ (BeV/c)^2$
2.7†	0.137	0.412	0.578
3.0	0.117	0.352	0.494
5.0	0.055	0.163	0.229

†$d\sigma$ values at 3 and 5 BeV/c are obtained from $d\sigma$ at 2.7 BeV/c.

FIGURE CAPTIONS

Fig. 1(a) Layout of the π^- beam at the Bevatron floor.

Fig. 1(b) Optical analogue of the π^- beam.

Fig. 2 Schematic representation of the target assembly showing the target anti-counters and the inner target counters around the liquid hydrogen target.

Fig. 3 Details of the Diboson Spectrometer (camera not shown).

Fig. 4 Electronic trigger logic demanding one π^- beam particle and two charged secondaries through the Diboson spectrometer system.

Fig. 5 Cross-section of the 'Foam plate' spark chambers (A) and the 'Hollow plate' spark chamber (B).

Fig. 6 Details of the mirror construction. The front silvered thin mirror and the back plate are of the same material so that thermal stresses are balanced out.

Fig. 7 Photograph of the calibration grids and fiducials taken at the beginning and end of each run. The film coordinates of the fiducials determine the scan lines and the film coordinates of the individual grid marks are used in the spatial reconstruction of the sparks.

Fig. 8(a) Example of an event accepted by SASS as a 'good 2-prong event' (Chamber 5 is <u>not</u> scanned in this part of the data processing).

Figs. 8(b,c) Example of (b) Multi-prong events, and (c) forward π^0 events (Trigger background) rejected while scanning. SASS rejects events with multiple beam tracks (not shown) as well.

Fig. 9 Flow Chart giving the major details of the data processing program. Section A analyzes the grid mark data and sets up the parameters for the spatial reconstruction. Section B (M5 off) analyzes the corrections to the chamber locations while (M5 off) determines the parameters of the beam momentum representation (Appendix D). Section C deals with the processing of the 2-prong events which fit the $(\pi^+\pi^-n)$ hypothesis.

Fig. 10 'Far Grids' and 'Near' Grids' (associated with each chamber) used as reference for spatial reconstruction of the sparks.

Fig. 11 Notations used in the spatial reconstruction: y_G, z_G are the measured coordinates of the far grids in the two views. y_F, z_F are the projected film coordinates as seen by the camera for a spark with coordinates (y,z) in real space. θ_V, θ_H are the projected inclinations of the line of sight.

Fig. 12 Convexity test in the xy plane (top view) demanding that θ_1, θ_{12}, θ_2 change monotonically separates the track segments which belong to different trajectories in the orbit determination. θ_1, θ_2 refer to the projected angles of the tracks in any two successive chambers.

Fig. 13(a) Histograms of the unconstrained missing mass at 3 BeV/c for events kinematically constrained to the hypothesis $\pi^- p \rightarrow \pi^+ \pi^- n$ and with different cuts on the χ^2 for the kinematic fit. Events with $\chi^2 < 50$ are accepted in the analysis. The neutron peak clearly visible in all the histograms has very little background for the selected sample of events.

Fig. 13(b) Histograms of the unconstrained missing mass at 5 BeV/c. Events with $\chi^2 < 25$ are used in the analysis.

Fig. 14(a) Unweighted dipion mass distribution at 3 BeV/c for events fitted to the $(\pi^+ \pi^- n)$ hypothesis.

Fig. 14(b) Unweighted dipion mass distribution at 5 BeV/c for fitted events.

Fig. 14(c) Unweighted dipion mass distributions at 3 GeV/c for different regions in $|t|$ and Cos $\theta_{\pi\pi}$.

Fig. 14(d) Unweighted dipion mass distributions at 5 GeV/c for different regions in $|t|$ and Cos $\theta_{\pi\pi}$.

Fig. 15(a) Unweighted Chew-Low plot at 3 BeV/c: $s_{\pi\pi} = m^2_{\pi\pi}$ in $(\text{BeV})^2$ vs $-t$ in $(\text{BeV/c})^2$. The events are dominantly 'peripheral'. The solid line represents the kinematic boundary.

Fig. 15(b) Unweighted Chew-Low plot at 5 BeV/c. $s_{\pi\pi} = m^2_{\pi\pi}$ in $(\text{BeV})^2$ vs $-t$ in $(\text{BeV/c})^2$.

Fig. 16 One pion exchange diagram. $\Delta^2 = -t$ is the square of the 4-momentum exchanged between the two vertices and s is the square of the c.m. energy of the initial or final state.

Fig. 17(a) Unweighted mass distribution at 3 BeV/c for the $(\pi^- n)$ system.

Fig. 17(b) Unweighted mass distribution at 5 BeV/c for the $(\pi^- n)$ system.

Fig. 17(c) Unweighted mass distribution at 3 BeV/c for the $(\pi^+ n)$ system.

Fig. 17(d) Unweighted mass distribution at 5 BeV/c for the $(\pi^+ n)$ system.

Fig. 18(a) Unweighted Dalitz plot at 3 BeV/c: $s_{\pi\pi}$ vs $s_{n\pi^+}$.

Fig. 18(b) Unweighted Dalitz plot at 3 BeV/c: $s_{\pi\pi}$ vs $s_{n\pi^-}$.

Fig. 18(c) Unweighted Dalitz plot at 5 BeV/c: $s_{\pi\pi}$ vs $s_{n\pi^+}$.

Fig. 18(d) Unweighted Dalitz plot at 5 BeV/c: $s_{\pi\pi}$ vs $s_{n\pi^-}$.

Fig. 19 The Gottfried-Jackson Frame of reference used for the analysis of the dipion angular distribution. This is the rest frame of the dipion, the quantization axis being along the direction of the incident pion in this frame.

Fig. 20 Forward-backward ratios at 3 and 5 BeV/c for $|t| \leq 0.1\ (\mathrm{BeV/c})^2$ as a function of $m_{\pi\pi}$ (BeV) indicating strong interference of the S-wave amplitude with the P-wave amplitude in the $\pi^+\pi^-$ channel in the dipion mass range 400 to 1000 MeV.

Fig. 21 S-wave (Isospin T = 0) phase shifts at 3 and 5 BeV/c for the $\pi^+\pi^-$ system derived from the forward-backward ratios for $|t| \leq 0.1\ (\mathrm{BeV/c})^2$ (neglecting δ_0^2, the S-wave phase shift in the T = 2 state).

Fig. 22(a-f) Density matrix elements vs $m_{\pi\pi}$ (BeV) at 3 and 5 BeV/c for different ranges in $|t|$.

Fig. 23(a,b) Density matrix elements vs $|t|\ (\mathrm{BeV/c})^2$ for $m_{\pi\pi}$ in the range 0.68 to 0.84 BeV. The solid lines are predictions based on OPEA.

Fig. 24(a,b) Density matrix elements vs $|t|\ (\mathrm{BeV/c})^2$ for $m_{\pi\pi}$ in the range 0.6 to 0.9 BeV. The solid lines are predictions based on OPEA.

Fig. 25(a,b) Forward-backward ratios at 3 and 5 BeV/c for $m_{\pi\pi}$ in the range 0.68 to 0.84 and 0.6 to 0.9 BeV.

Fig. 26 $d\sigma/dt$ (mb) vs $|t|\ (\mathrm{BeV/c})^2$ for $m_{\pi\pi}$ in the range 0.68 to 0.84 BeV. The solid lines represent predictions based on OPEA. The curves are normalized to the data points at $|t| = 0.04\ (\mathrm{BeV/c})^2$.

Fig. 27 $d\sigma/dt$ (mb) vs $|t|\ (\mathrm{BeV/c})^2$ for $m_{\pi\pi}$ in the range 0.6 to 0.9 BeV. The solid lines represent predictions based on OPEA. The curves are normalized to the data points at $|t| = 0.04\ (\mathrm{BeV/c})^2$.

Fig. 28 One pion exchange diagram with absorption in the initial and final channels. $C_{i,f}$ and $\gamma_{i,f}$ are the absorption parameters. C_i and γ_i are derived from the total and elastic πN cross-sections. $C_f = 1$ and $\gamma_f = 3/4\ \gamma_i$ is assumed as per the Gottfried-Jackson prescription.

Fig. 29 (a,b,c) Weighted histograms of the dipion mass at 3 BeV/c for diffrent ranges in $|t|$. The solid line A represents the fitted curve (Function III(b), i = 2 in Table) and B, C are the contributions from the ρ^o and the added Breit-Wigner enhancement respectively. The background (not shown) is in this case small but negative.

Fig. 30 (a,b,c) Weighted histograms of the dipion mass at 5 BeV/c for different ranges in $|t|$. A is the fitted curve (Function III(c) i = 2 in Table). B, C, D are the contributions from ρ^o, the enhancement around 930 MeV, and the enhancement around 1030 MeV respectively. The dotted curve E represents the background.

Fig. 31 (a,b,c) Fits to the weighted dipion mass distribution at 3 BeV/c, using function V(b) in Table and excluding the ω^o contribution. Solid line A represents the fitted function V(b) in Table and represents the contribution from the enhancement around 570 MeV.

Fig. 32 (a,b,c) Fits to the weighted dipion mass distribution at 5 BeV/c using function V(b) in Table and excluding the ω^o contribution. Solid line A is the fitted function V(b) in Table and B represents the contribution from the incoherent enhancement at 930 MeV.

Fig. 33 (a,b,c) Fits to the weighted dipion mass distribution at 3 BeV/c using the ω-ρ interference model and an added incoherent enhancement (function V(b). ω^o is included. Curve A is the fitted function and B the contribution from the added enhancement at 570 MeV.

Fig. 34 (a,b,c. Fits to the weighted dipion mass distribution at 5 BeV/c using the ω-ρ interference model and an added incoherent enhancement (function V(b). ω^o is included. Curve A is the fitted function and B the contribution from the added enhancement at 930 MeV.

XBL 691-129

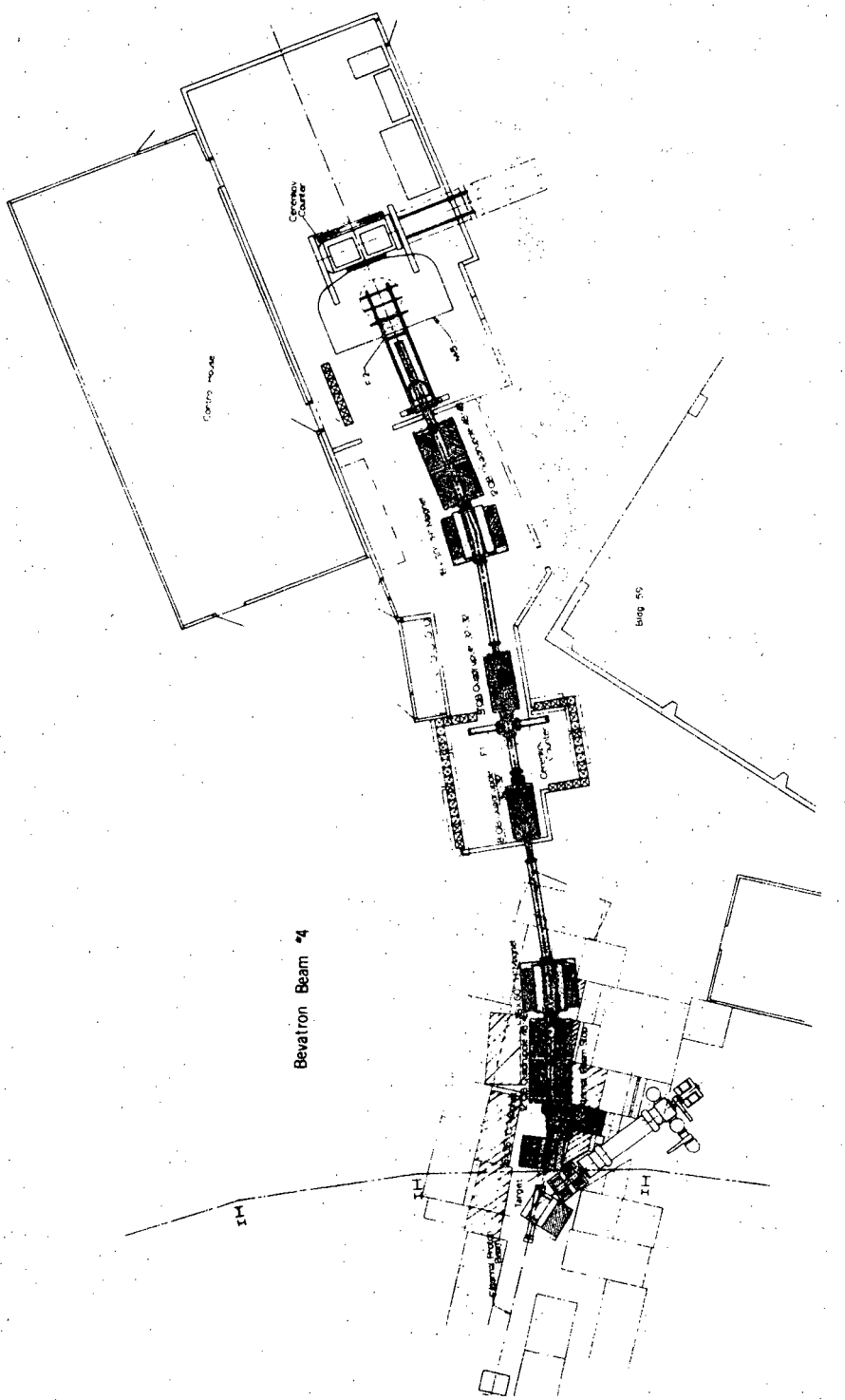

Fig. 1a

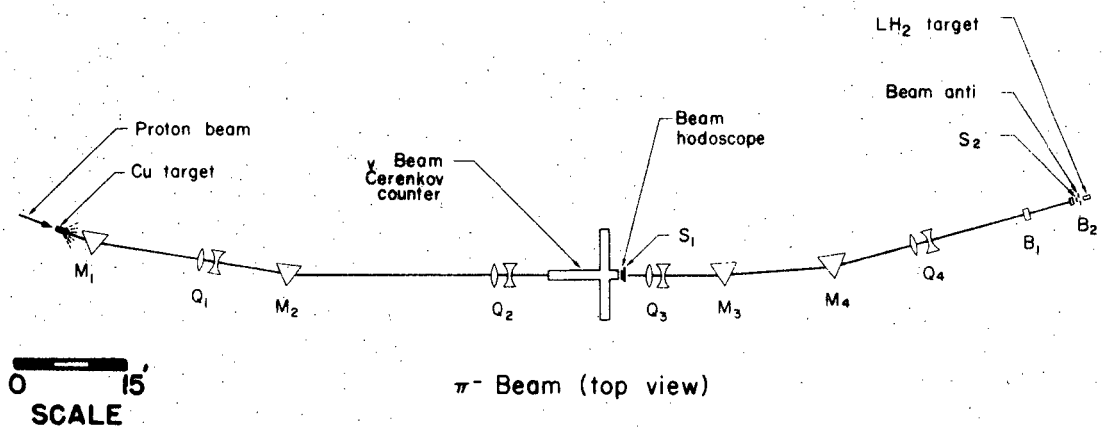

XBL 688-3526

Fig. 1b

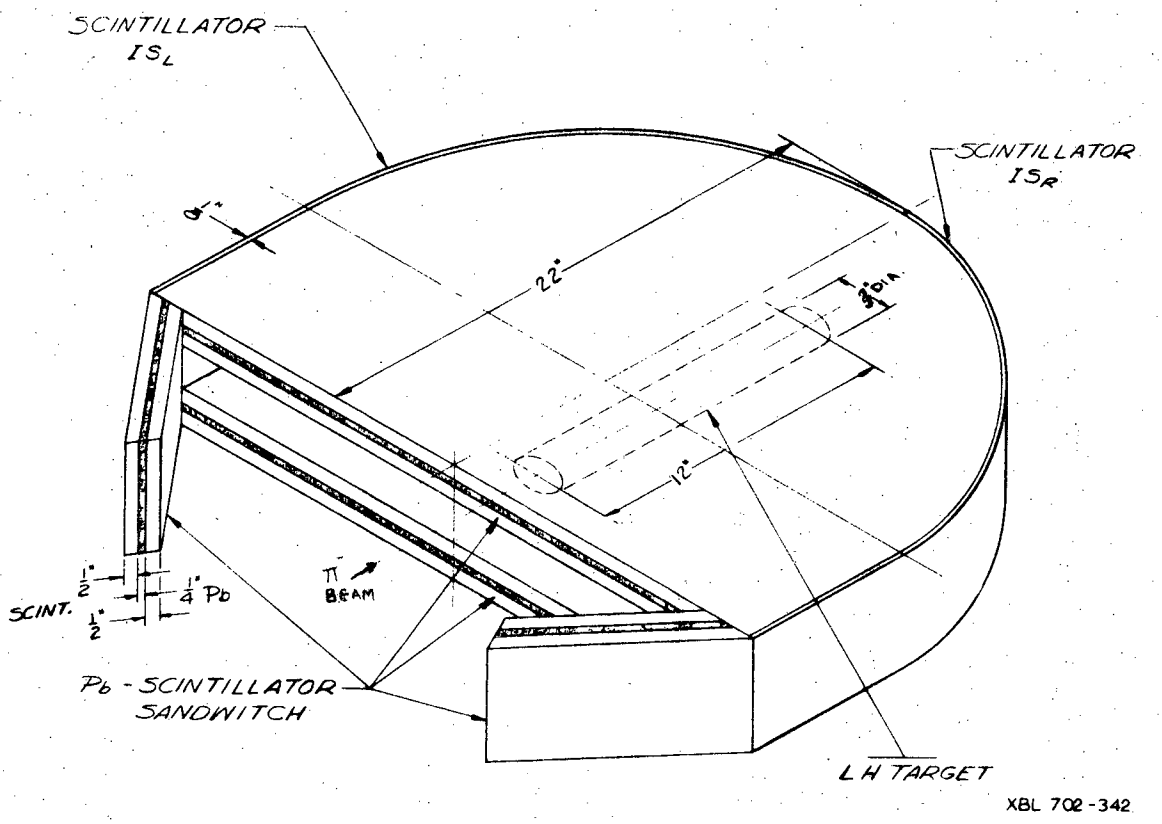
SCINTILLATOR
IS_L
SCINTILLATOR
IS_R
22"
12"
$\frac{3}{8}$" DIA.
$\frac{1}{2}$"
$\frac{1}{4}$" Pb
SCINT.
$\frac{1}{2}$"
π^-
BEAM
Pb - SCINTILLATOR
SANDWITCH
LH TARGET
XBL 702-342

Fig. 2

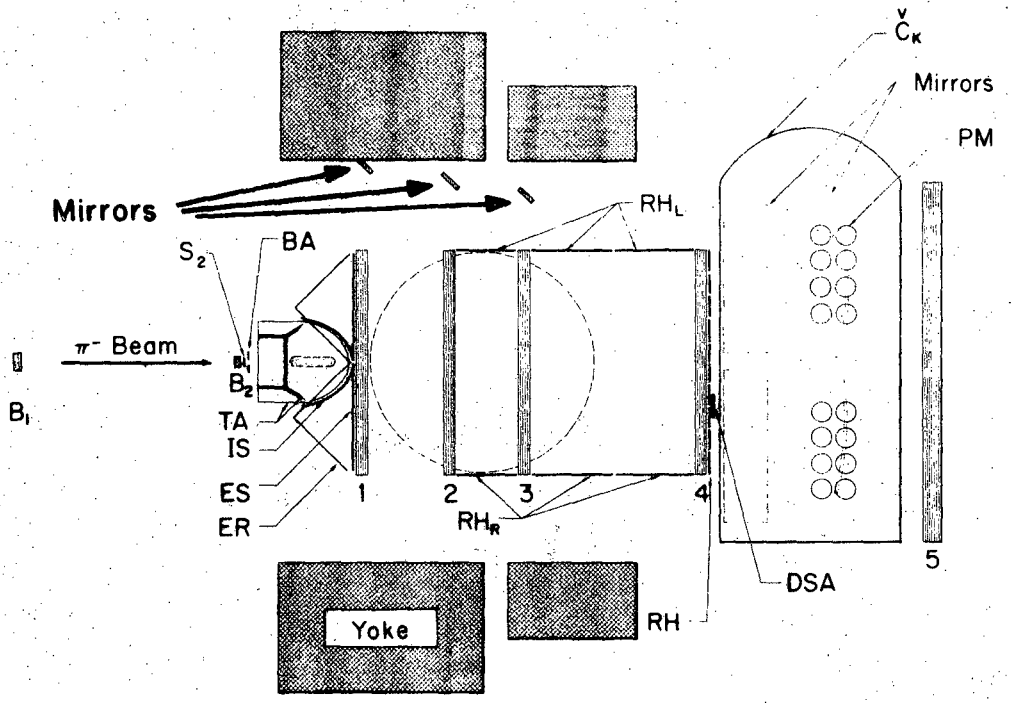

DIBOSON SPECTROMETER
(top view)

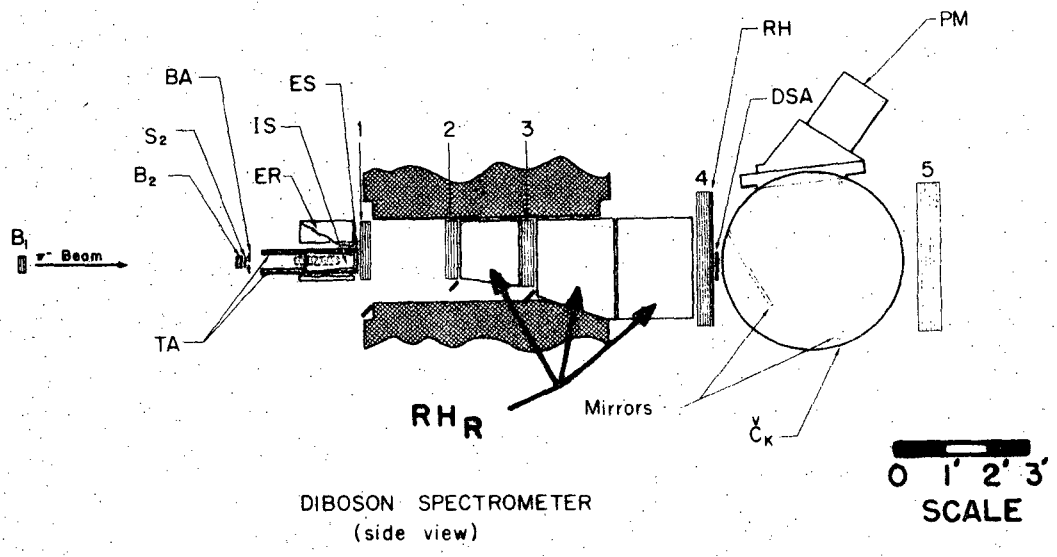

DIBOSON SPECTROMETER
(side view)

XBL 688-3527

Fig. 3

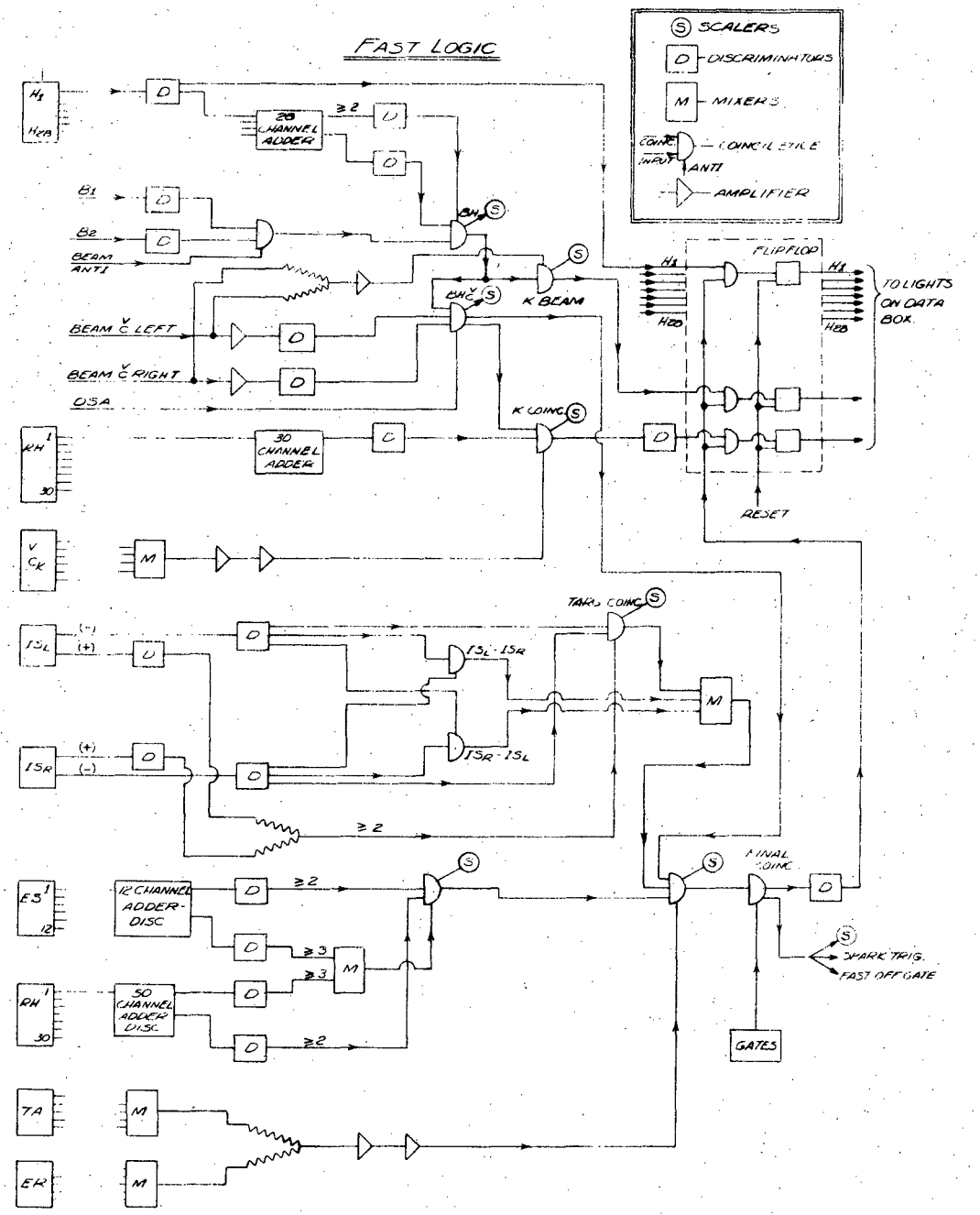
FAST LOGIC
SCALERS
DISCRIMINATORS
MIXERS
COINCIDENCE
ANTI
AMPLIFIER
20 CHANNEL ADDER
≥ 2
B1
B2
BEAM ANTI
BEAM C̄ LEFT
BEAM C̄ RIGHT
DSA
K BEAM
FLIPFLOP
TO LIGHTS ON DATA BOX.
RESET
30 CHANNEL ADDER
K COINC.
TARG. COINC.
ISL - ISR
ISR - ISL
12 CHANNEL ADDER-DISC
≥ 3
50 CHANNEL ADDER DISC
FINAL COINC.
SPARK TRIG.
FAST OFF GATE
GATES
XBL 702-382

Fig. 4

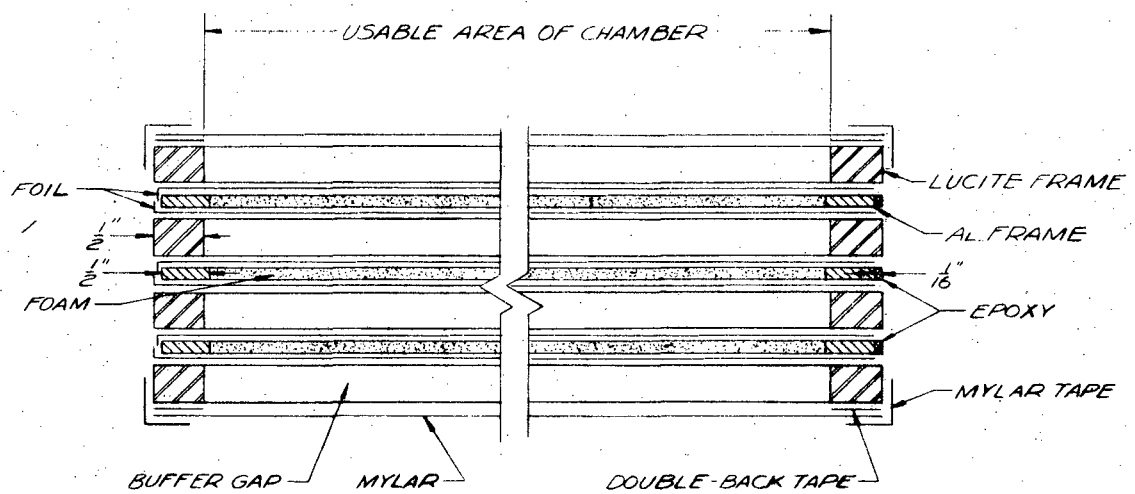

FIG. A

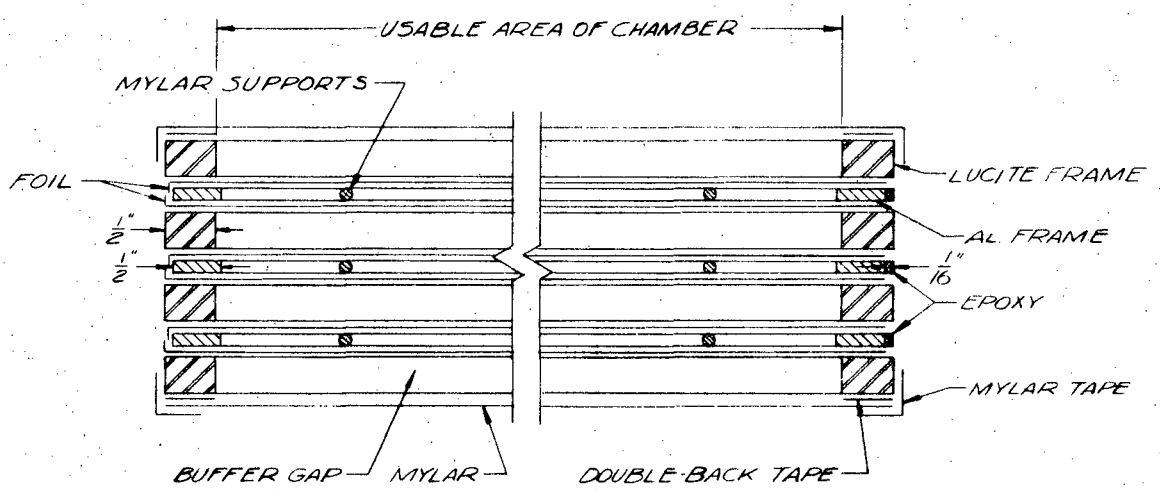

XBL 702-340

FIG. B

Fig. 5

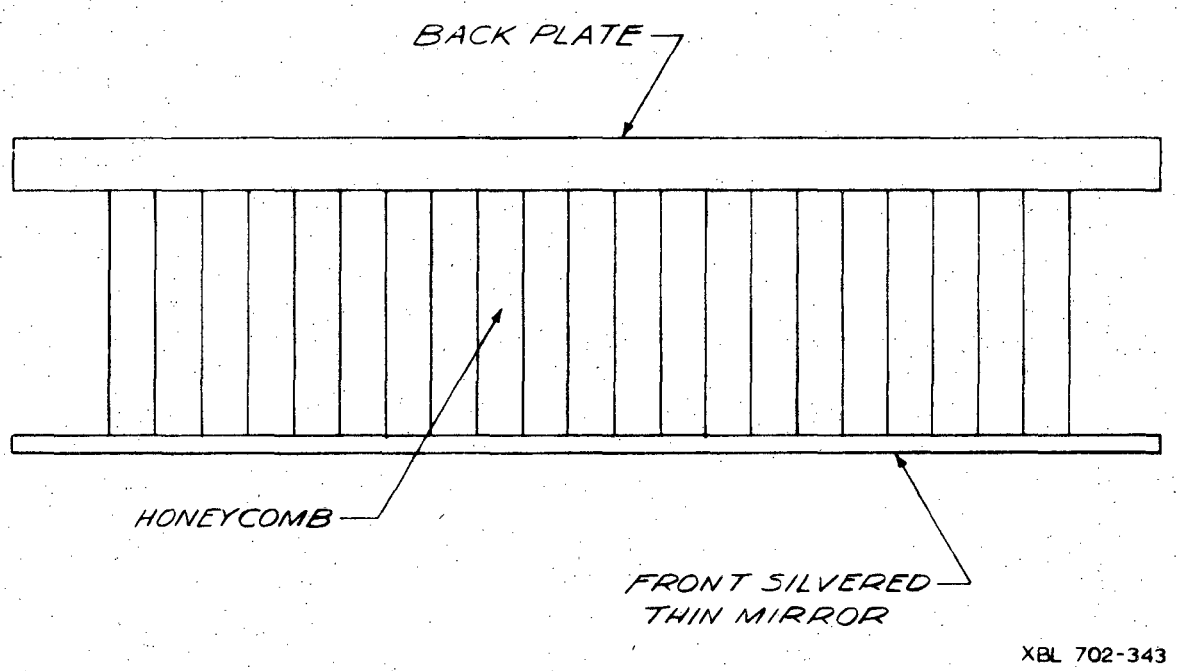
BACK PLATE
HONEYCOMB
FRONT SILVERED
THIN MIRROR
XBL 702-343

Fig. 6

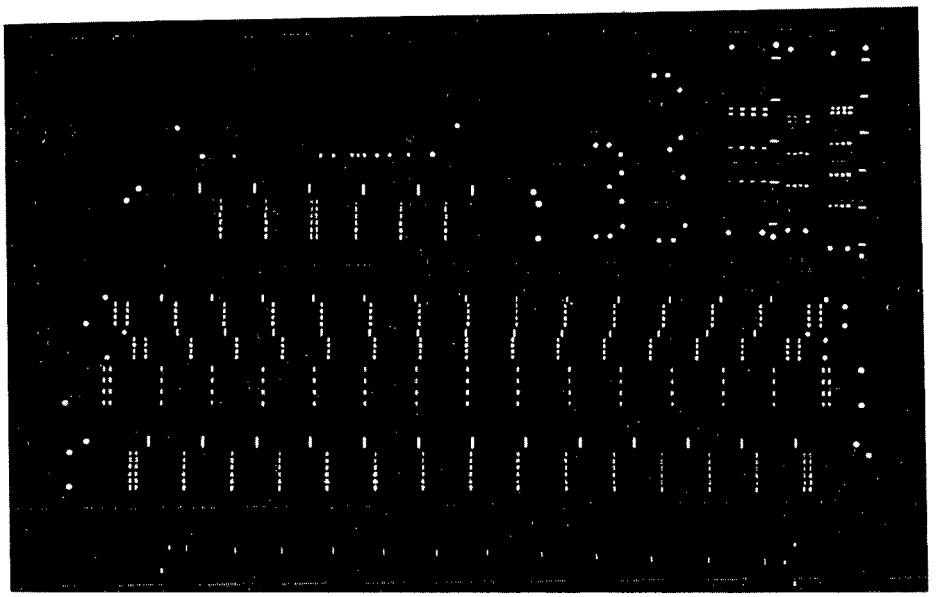

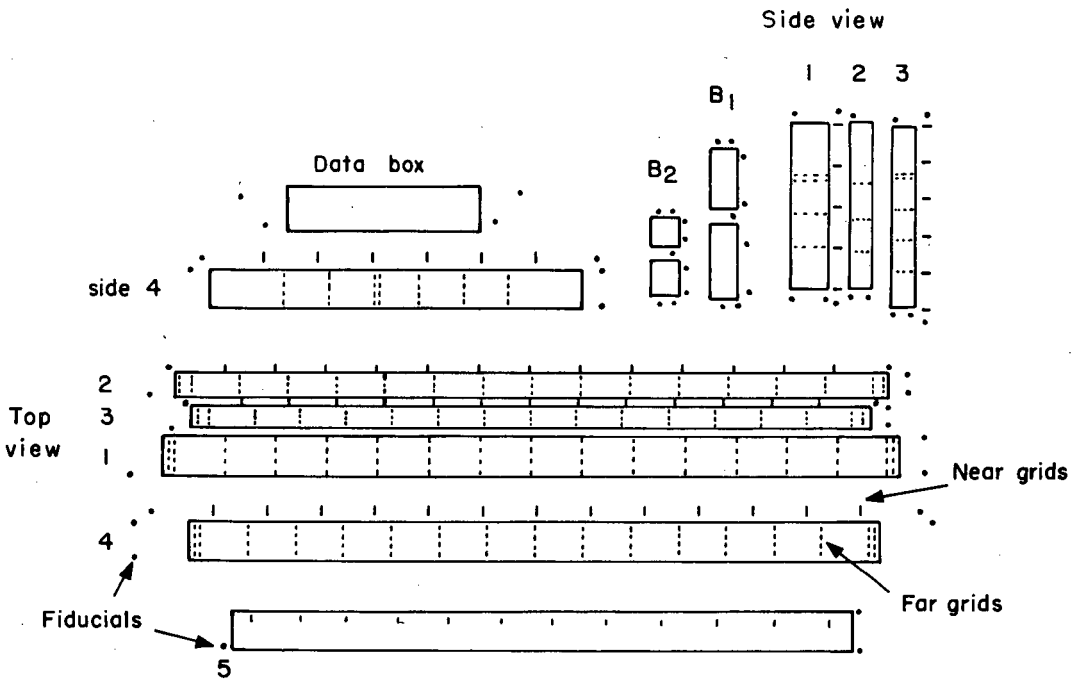

XBB 702-777

Fig. 7

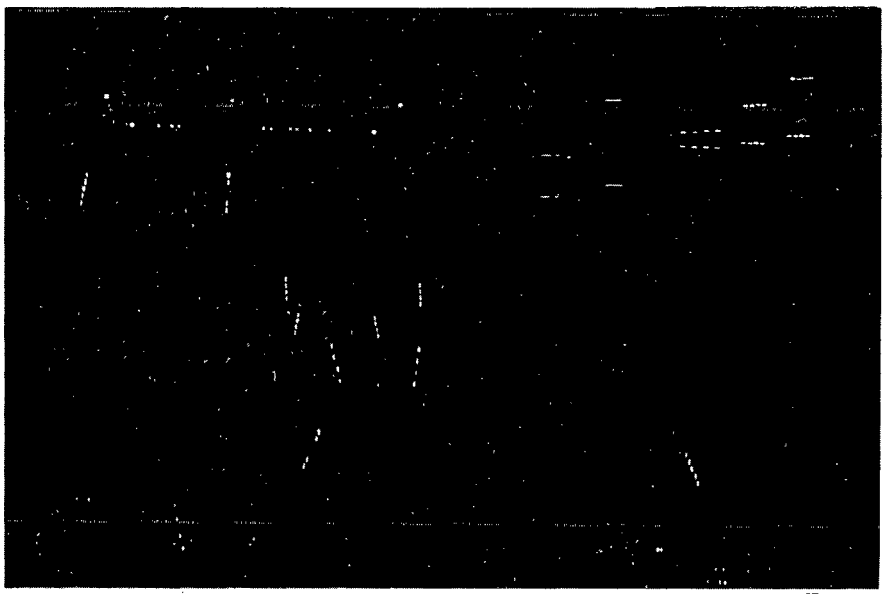

XBB 691-102

Fig. 8a

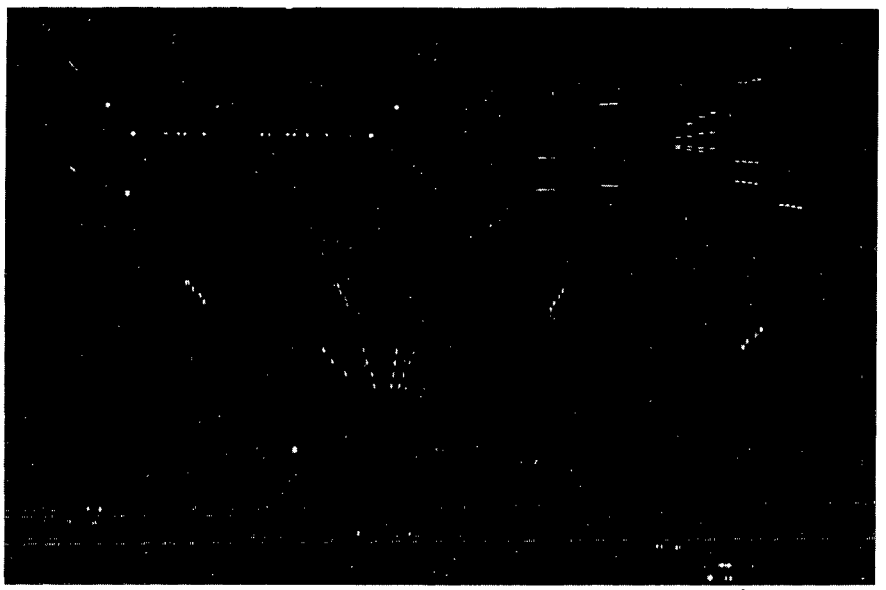

(b)

XBB 691-105

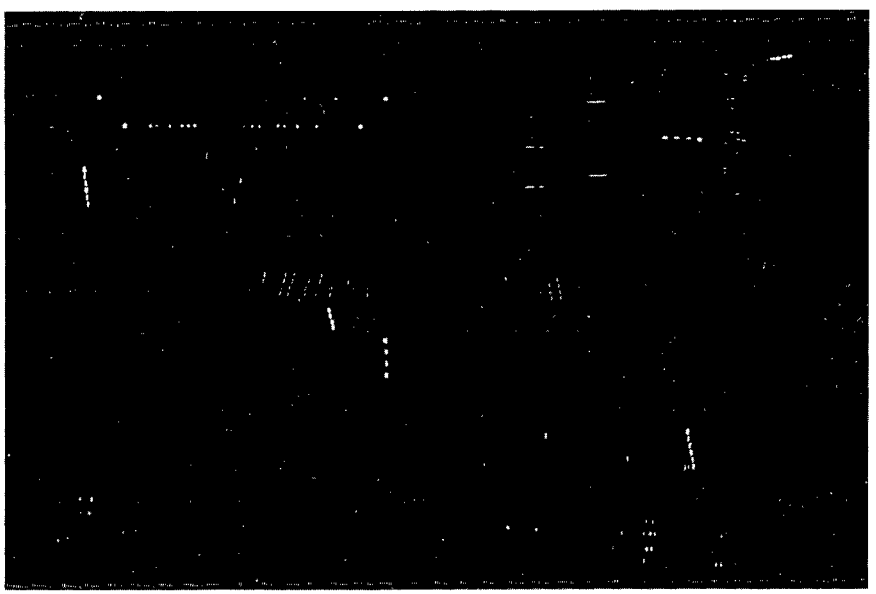

(c)

XBB 691-106

Fig. 8 b,c

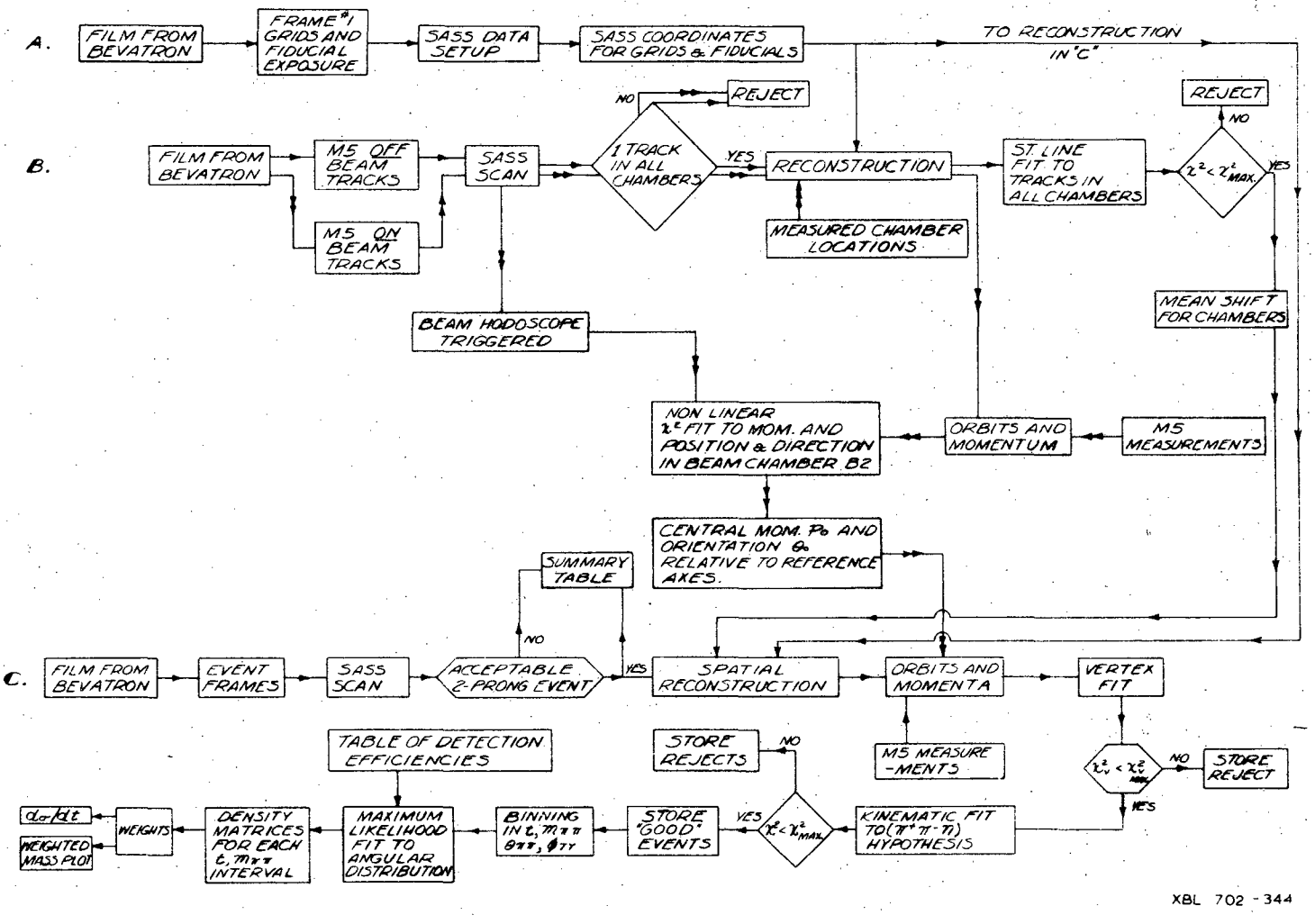
A.
FILM FROM BEVATRON
FRAME #1 GRIDS AND FIDUCIAL EXPOSURE
SASS DATA SETUP
SASS COORDINATES FOR GRIDS & FIDUCIALS
TO RECONSTRUCTION IN "C"
B.
FILM FROM BEVATRON
M5 OFF BEAM TRACKS
M5 ON BEAM TRACKS
SASS SCAN
1 TRACK IN ALL CHAMBERS
NO
REJECT
YES
RECONSTRUCTION
MEASURED CHAMBER LOCATIONS
ST. LINE FIT TO TRACKS IN ALL CHAMBERS
REJECT
NO
YES
MEAN SHIFT FOR CHAMBERS
BEAM HODOSCOPE TRIGGERED
NON LINEAR χ² FIT TO MOM. AND POSITION & DIRECTION IN BEAM CHAMBER B2
ORBITS AND MOMENTUM
M5 MEASUREMENTS
CENTRAL MOM. P₀ AND ORIENTATION θ₀ RELATIVE TO REFERENCE AXES.
SUMMARY TABLE
NO
C.
FILM FROM BEVATRON
EVENT FRAMES
SASS SCAN
ACCEPTABLE 2-PRONG EVENT
YES
SPATIAL RECONSTRUCTION
ORBITS AND MOMENTA
VERTEX FIT
TABLE OF DETECTION EFFICIENCIES
STORE REJECTS
NO
M5 MEASURE-MENTS
NO
STORE REJECT
YES
dσ/dt
WEIGHTED MASS PLOT
WEIGHTS
DENSITY MATRICES FOR EACH t, m_ππ INTERVAL
MAXIMUM LIKELIHOOD FIT TO ANGULAR DISTRIBUTION
BINNING IN t, m_ππ θ_ππ, φ_TY
STORE "GOOD" EVENTS
YES
KINEMATIC FIT TO (π⁺π⁻η) HYPOTHESIS
XBL 702 - 344

Fig. 9

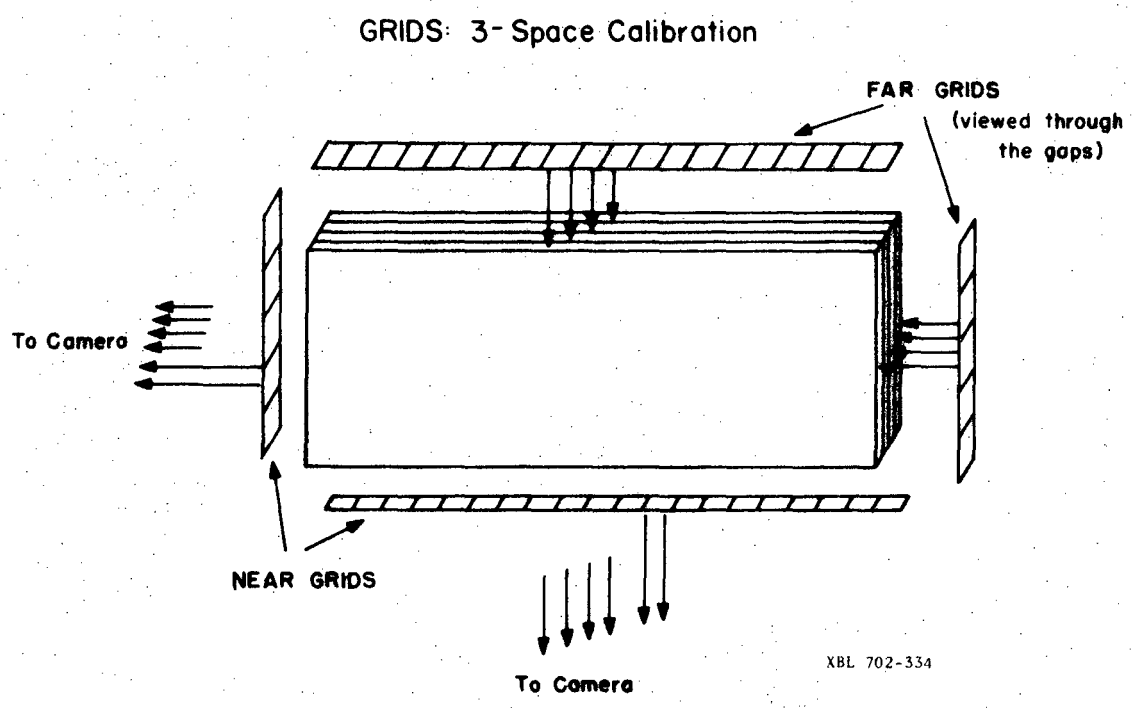
GRIDS: 3-Space Calibration
FAR GRIDS
(viewed through the gaps)
To Camera
NEAR GRIDS
To Camera
XBL 702-334

Fig. 10

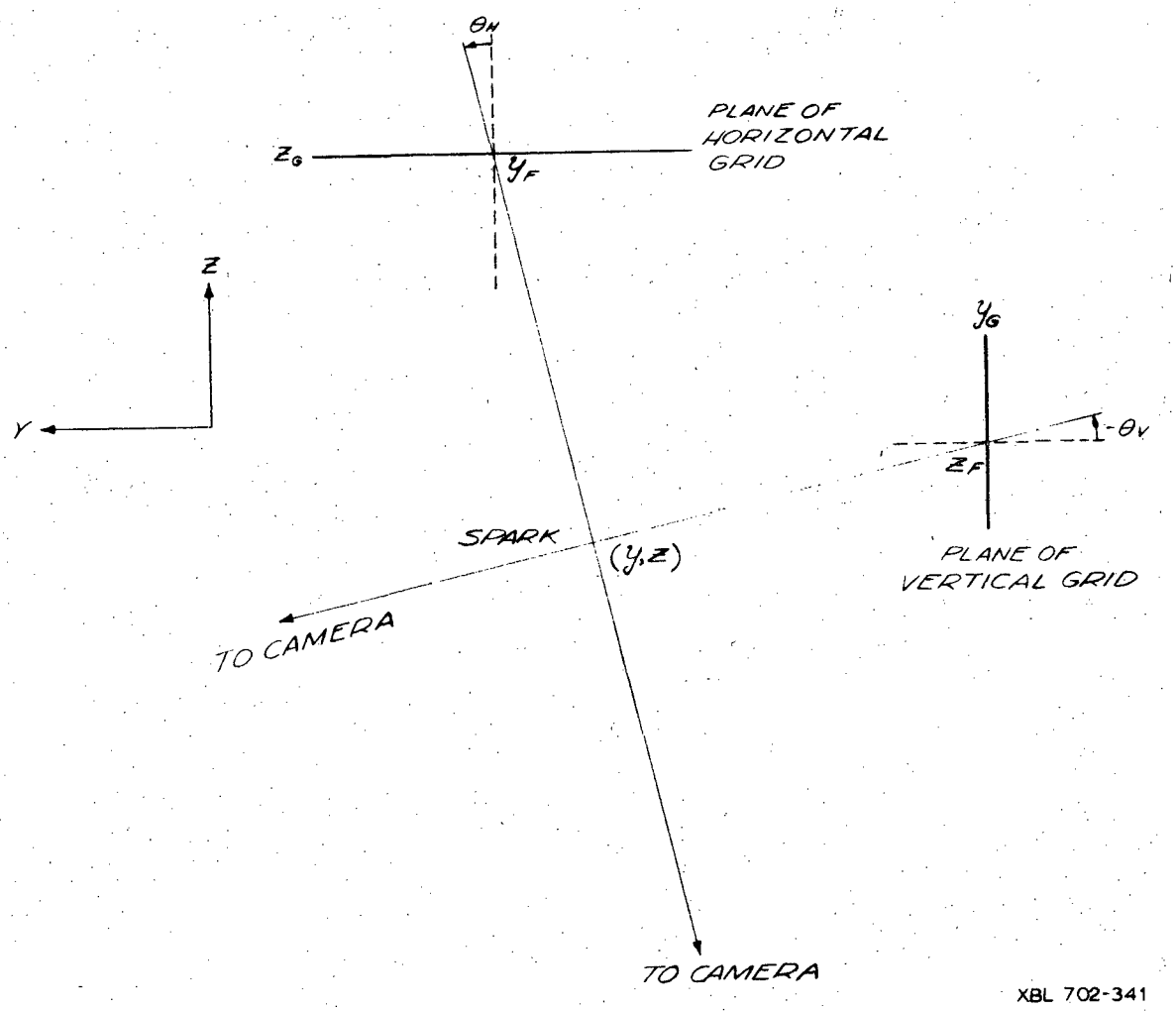
θH
PLANE OF
HORIZONTAL
GRID
ZG
yF
Z
Y
yG
-θV
zF
SPARK
(y,z)
PLANE OF
VERTICAL GRID
TO CAMERA
TO CAMERA
XBL 702-341

Fig. 11

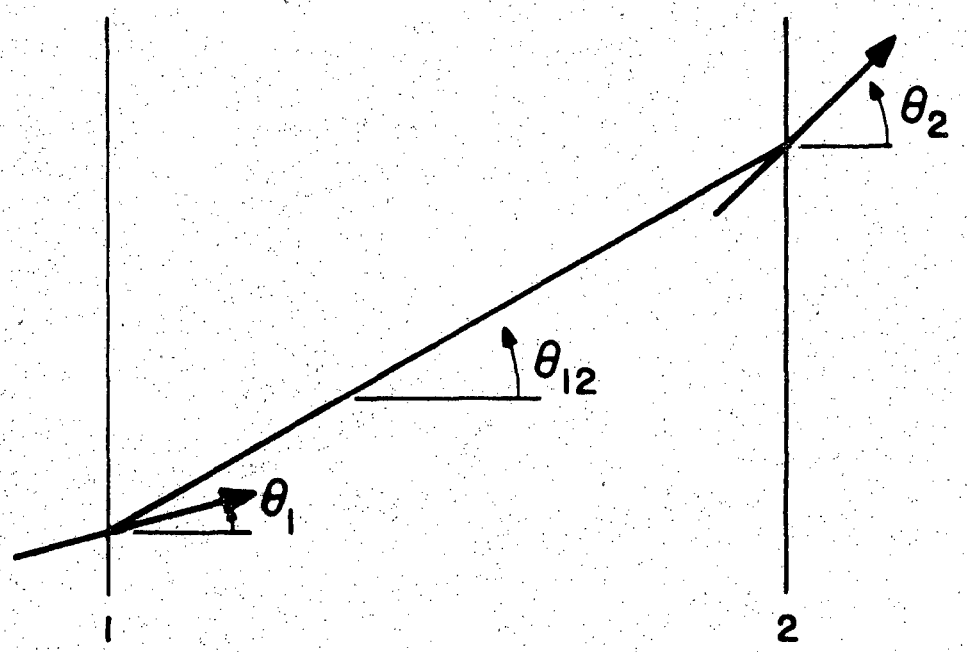

XBL 702-332

Fig. 12

3.0 BEV/C

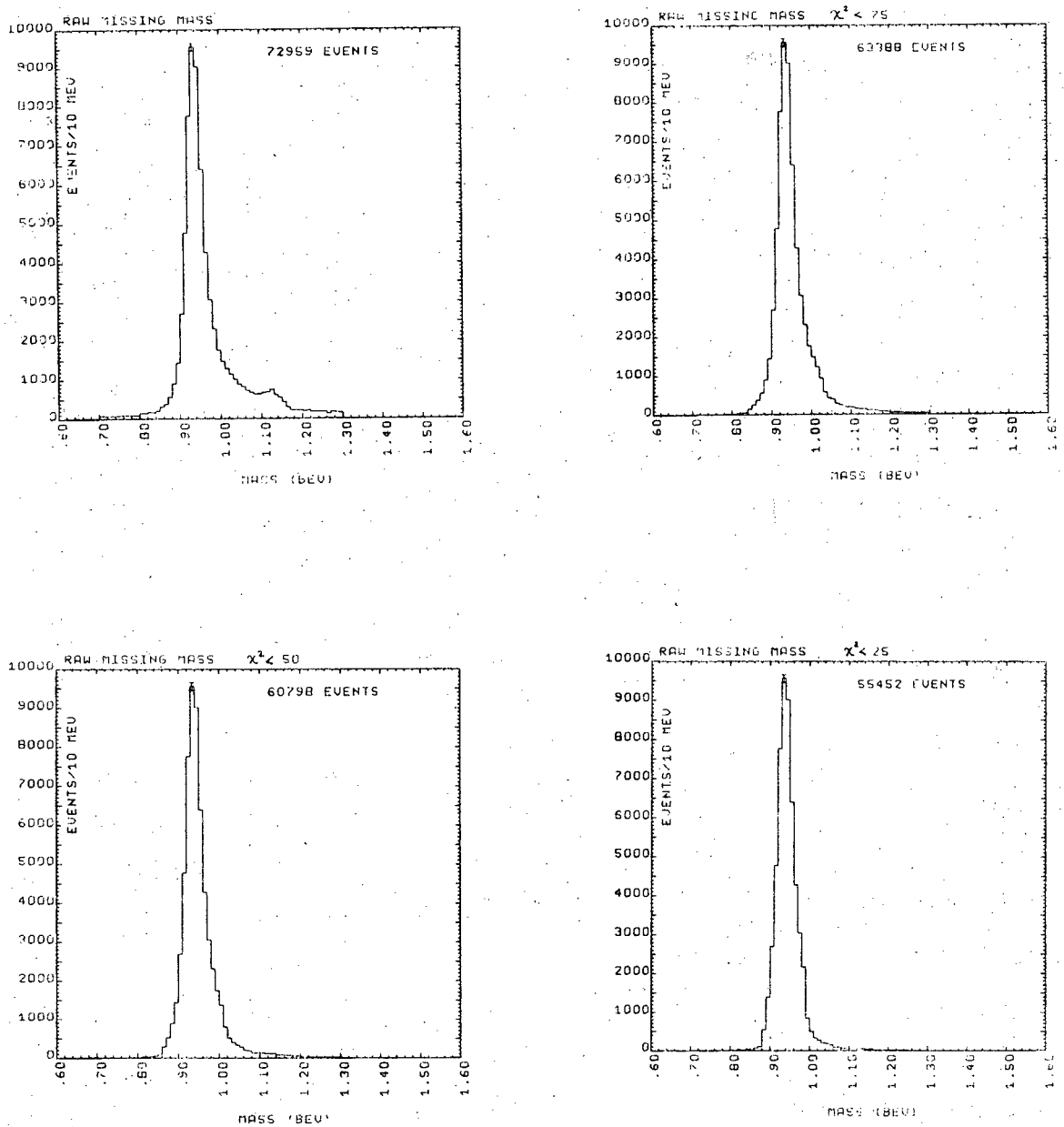

XBL 703-568

Fig. 13a

5.0 BEV/C

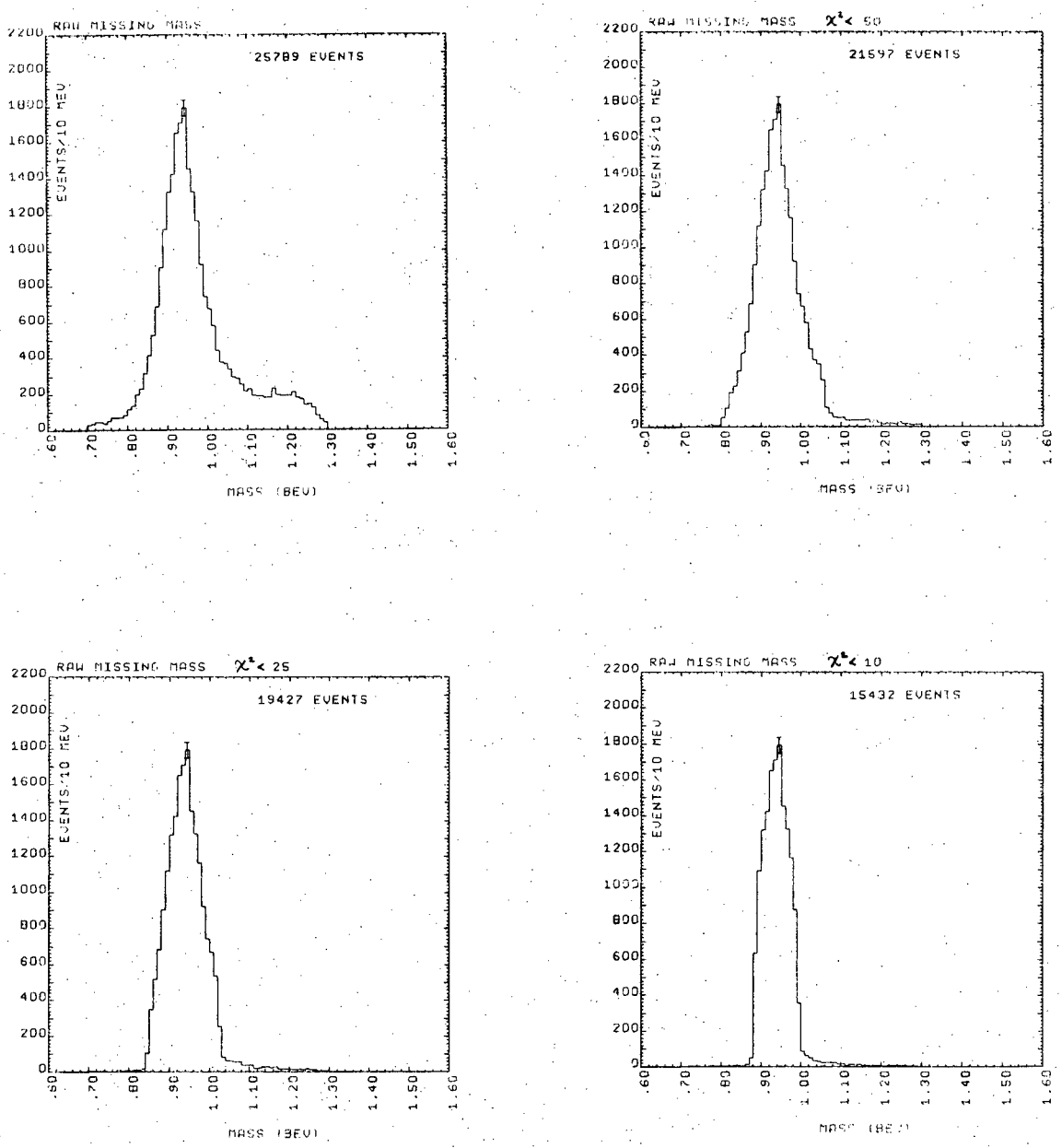

XBL 703-569

Fig. 13b

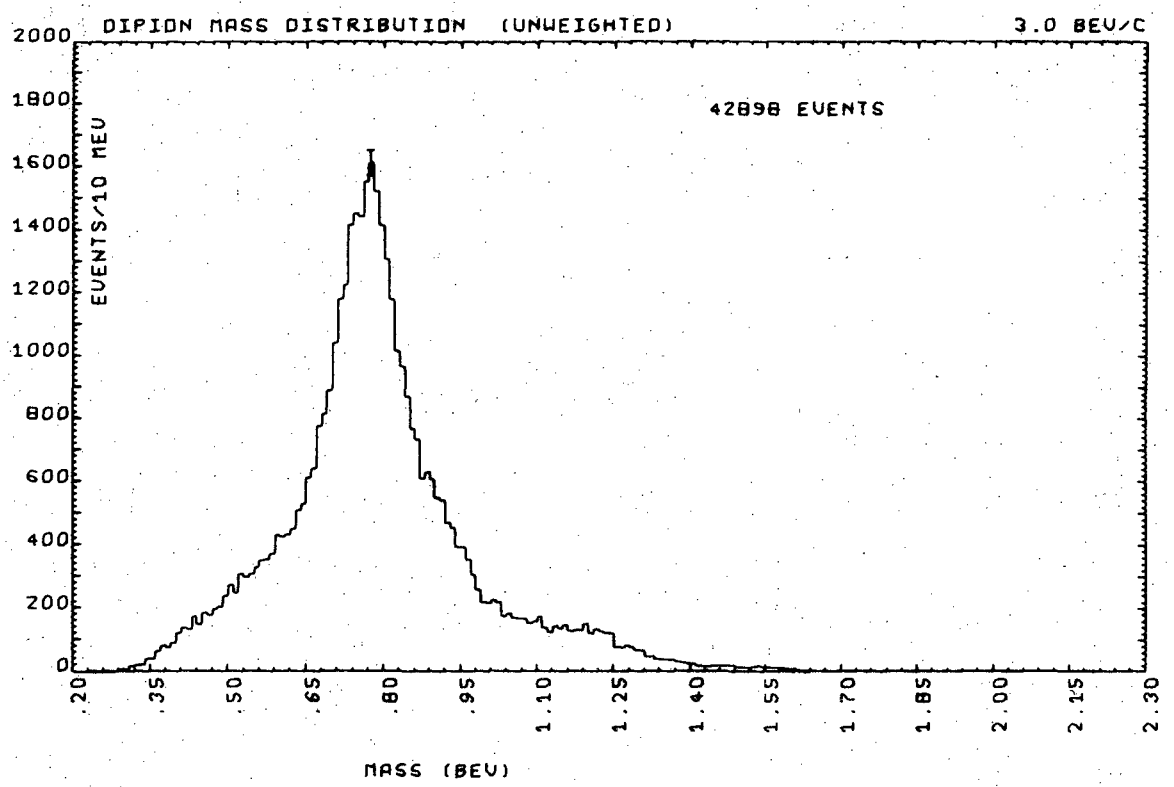

XBL 702-339

Fig. 14a

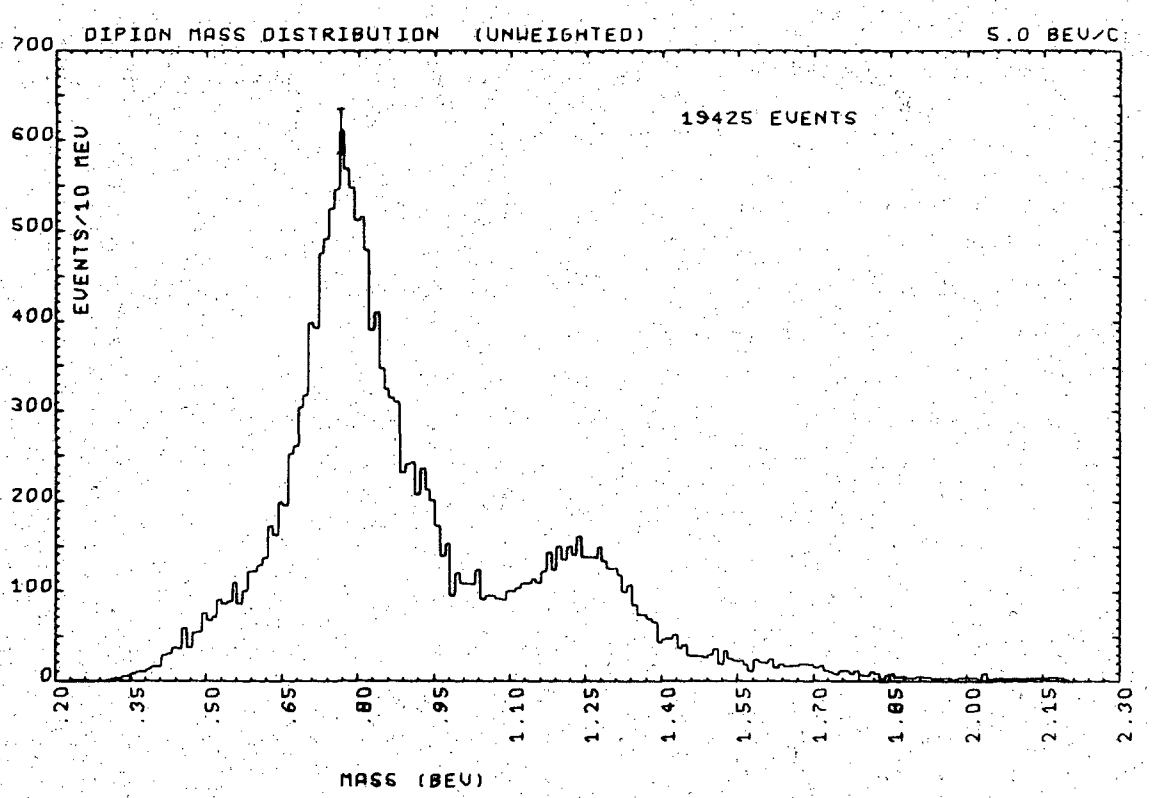

XBL 702-338

Fig. 14b

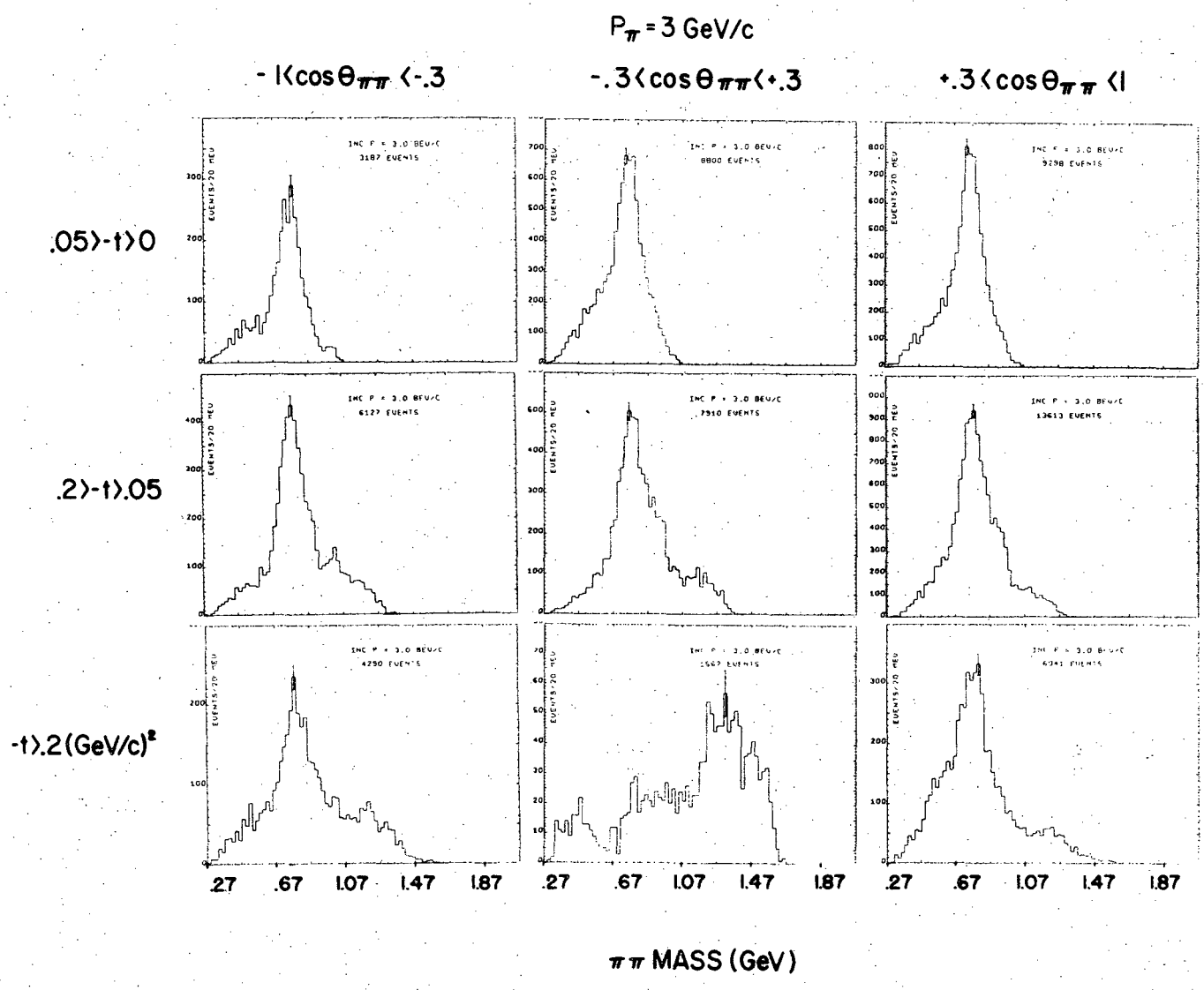

Fig. 14c

XBL 702-330

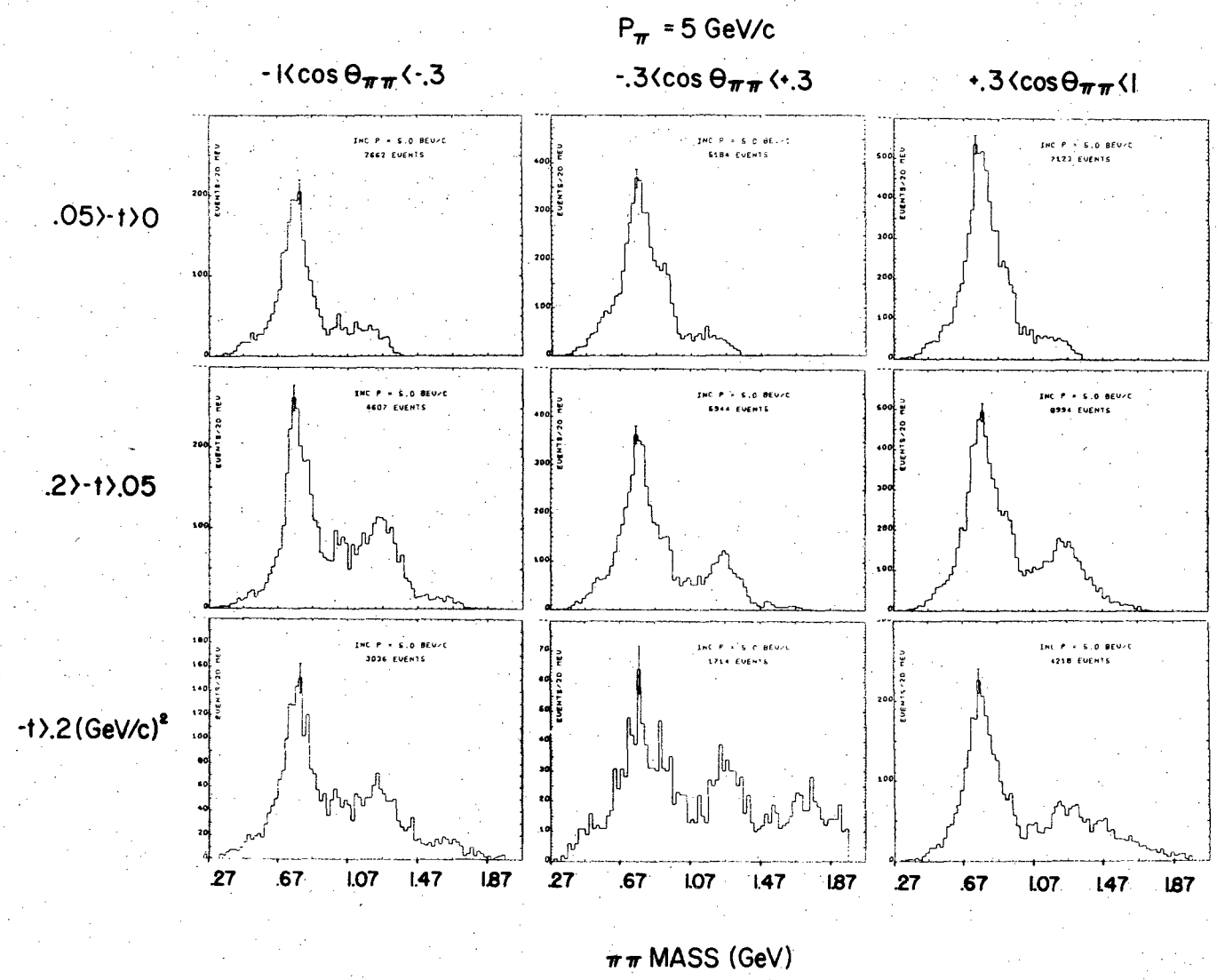

XBL 702-331

Fig. 14d

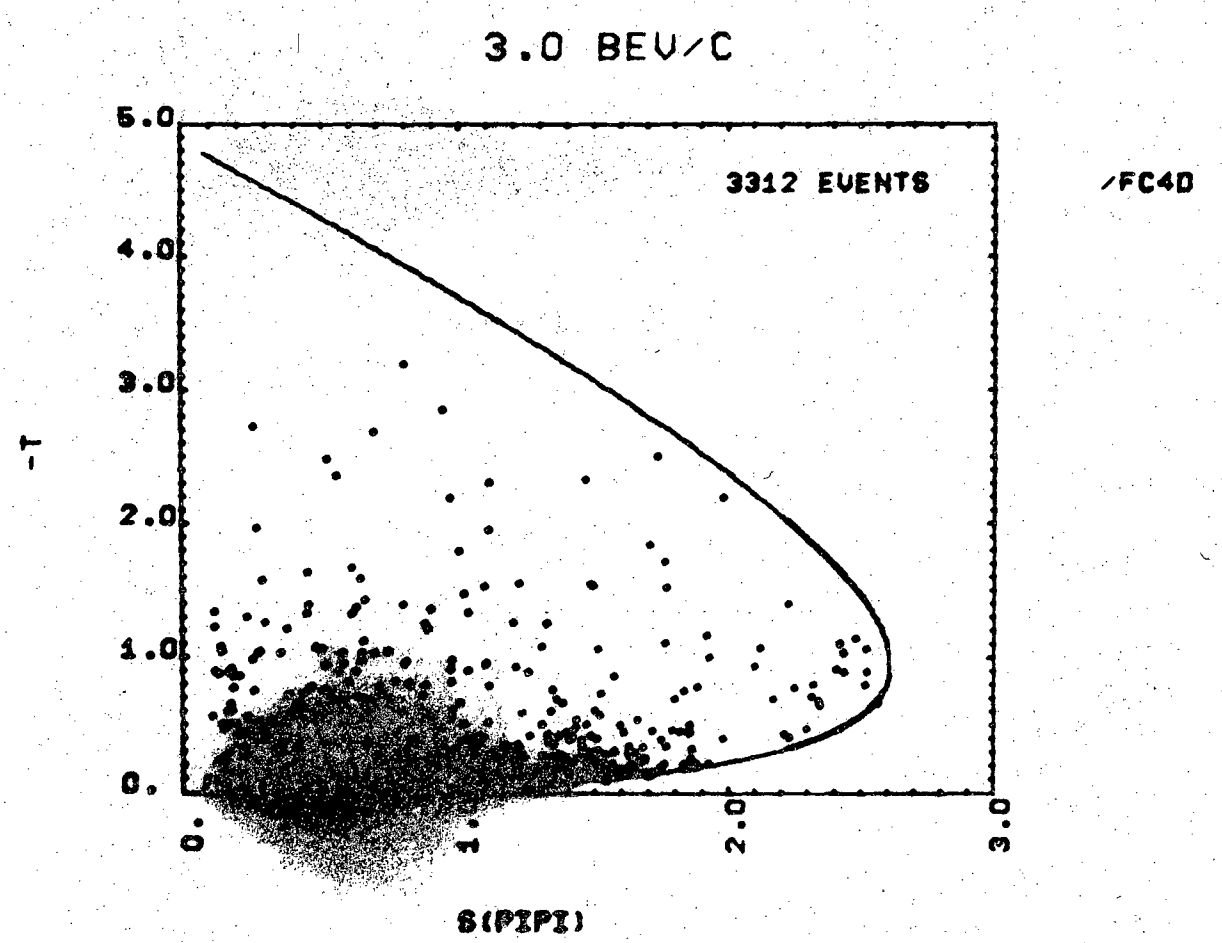

Fig. 15a

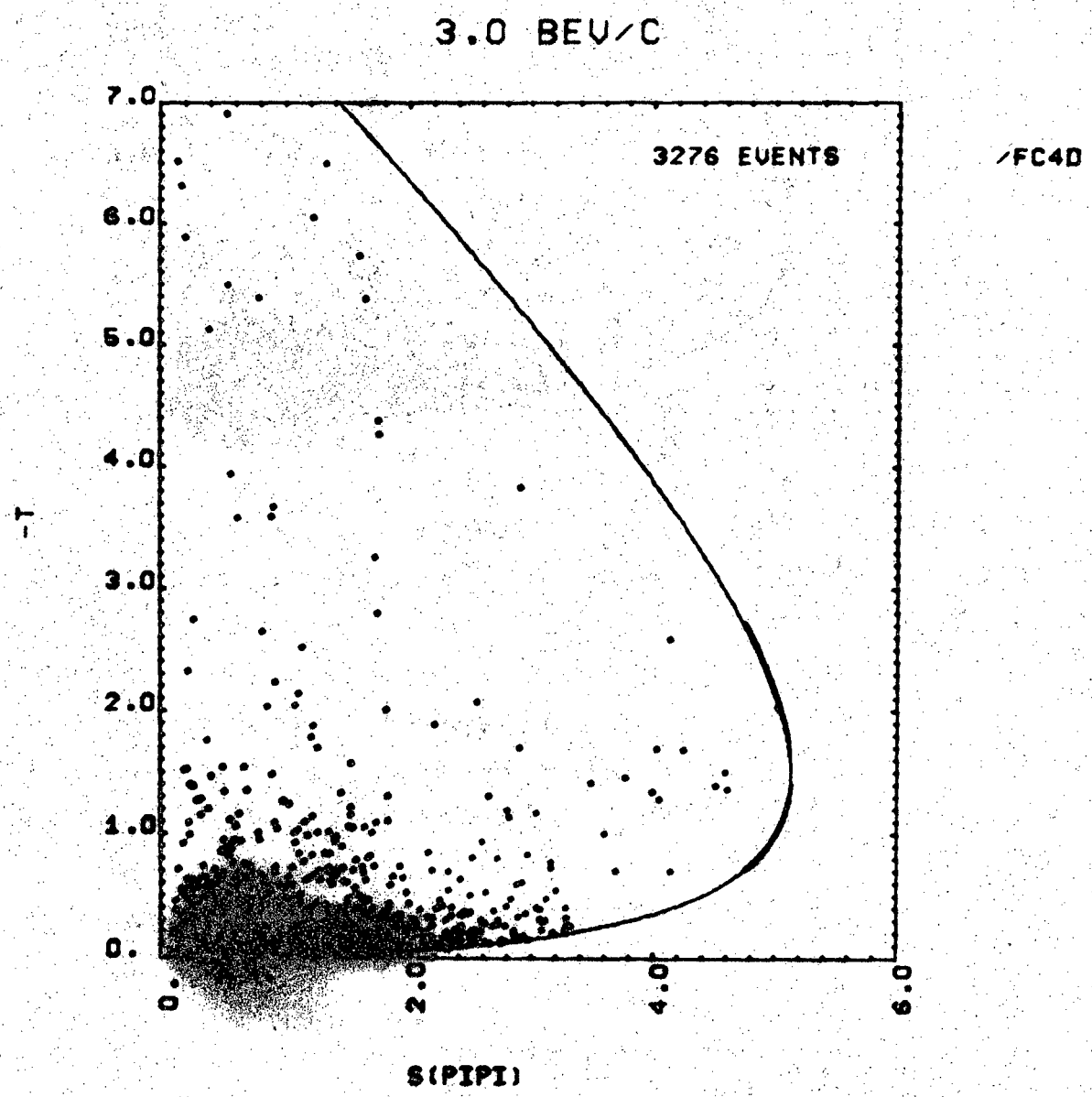

Fig. 15b

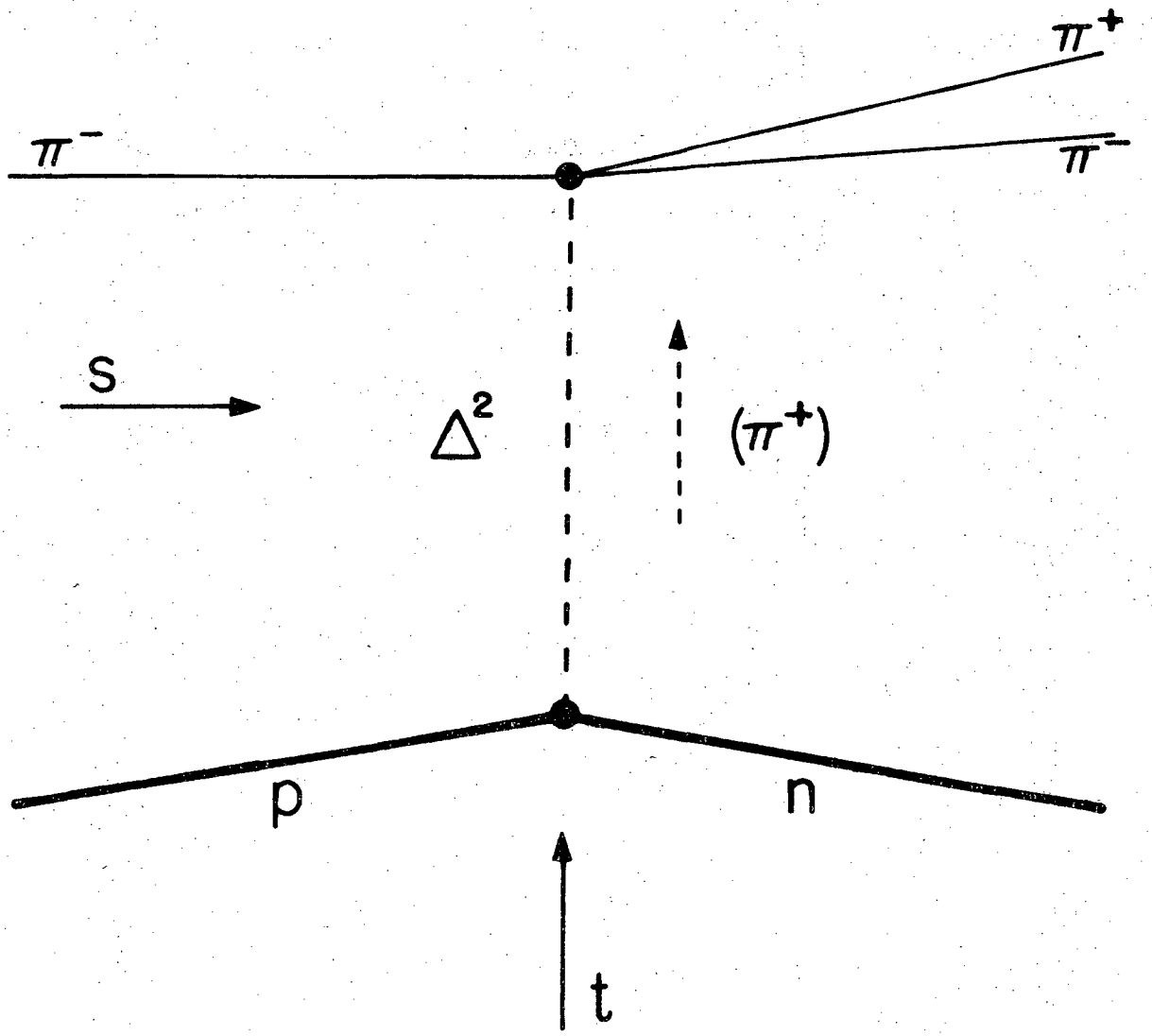

XBL 702-336

Fig. 16

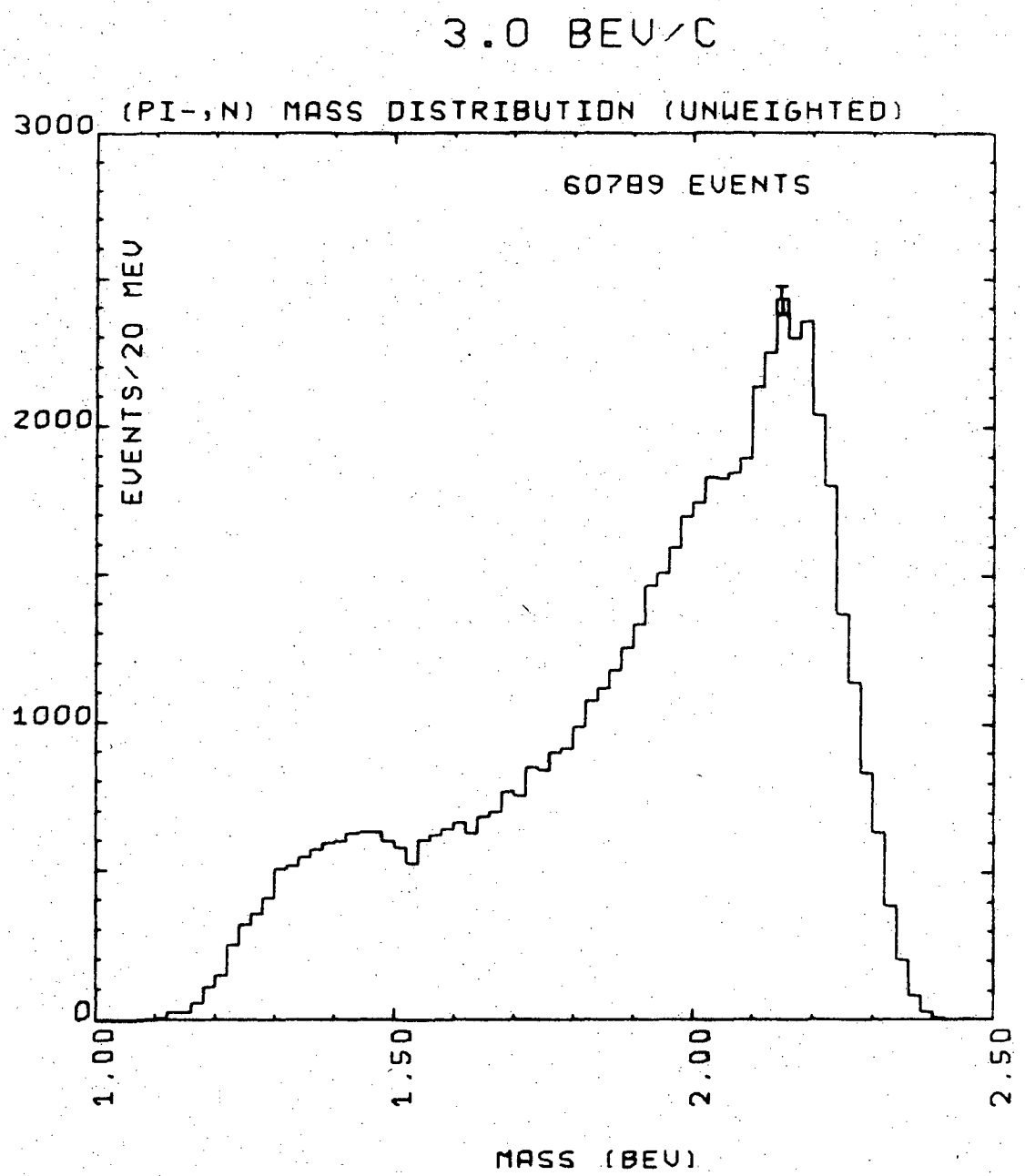

XBL 702-357

Fig. 17a

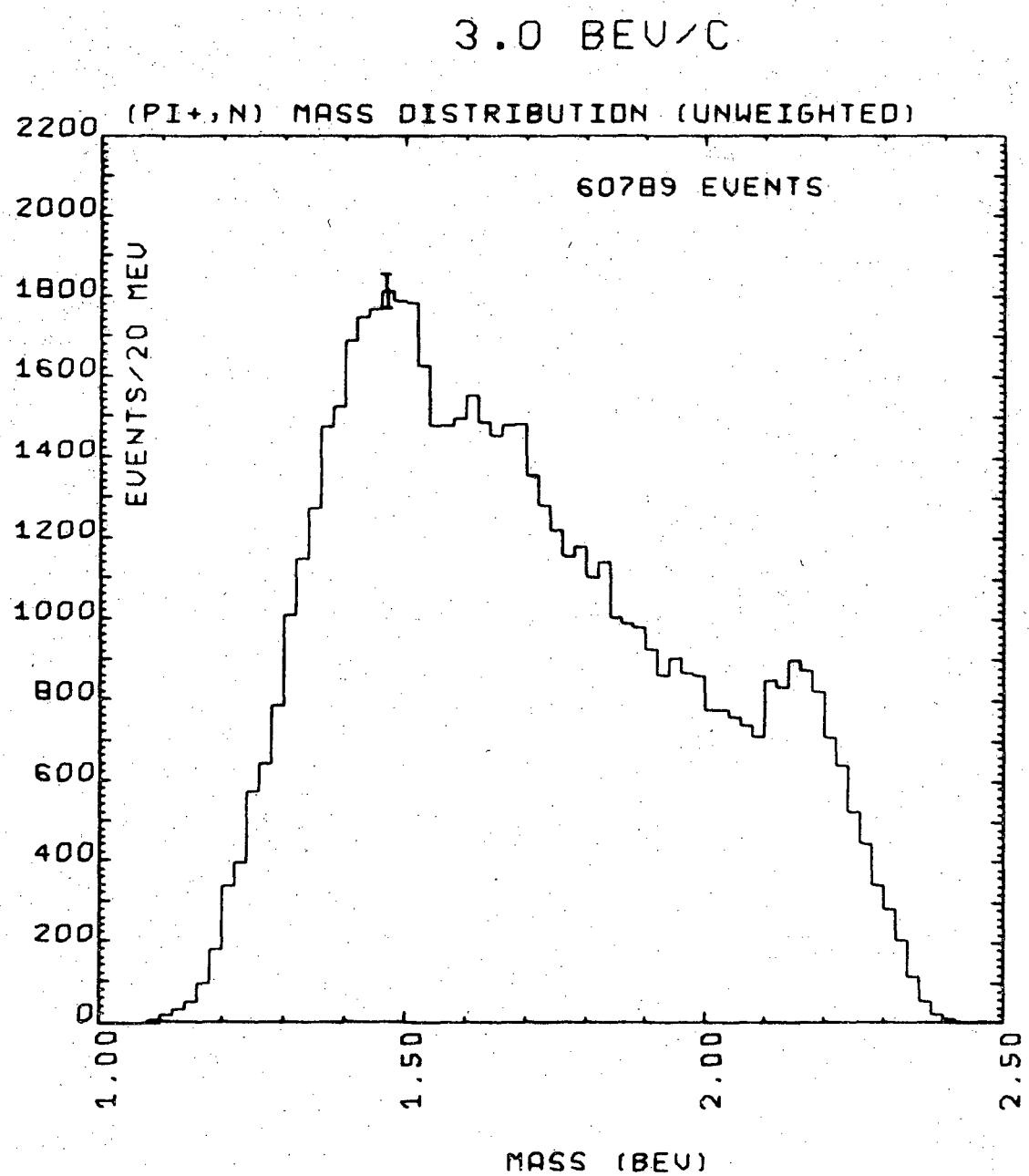

XBL 702-360

Fig. 17b

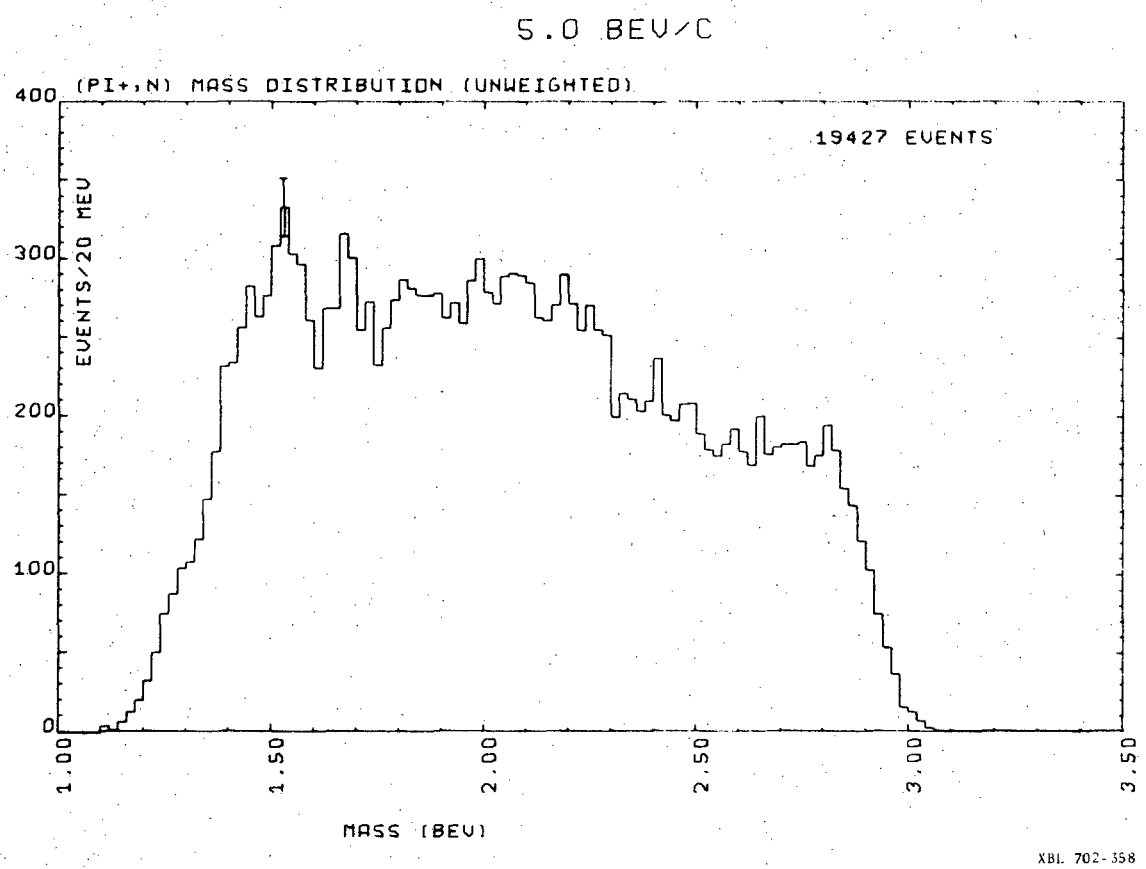
5.0 BEV/C
(PI+,N) MASS DISTRIBUTION (UNWEIGHTED)
19427 EVENTS
EVENTS/20 MEV
400
300
200
100
0
1.00
1.50
2.00
2.50
3.00
3.50
MASS (BEV)
XBL 702-358

Fig. 17c

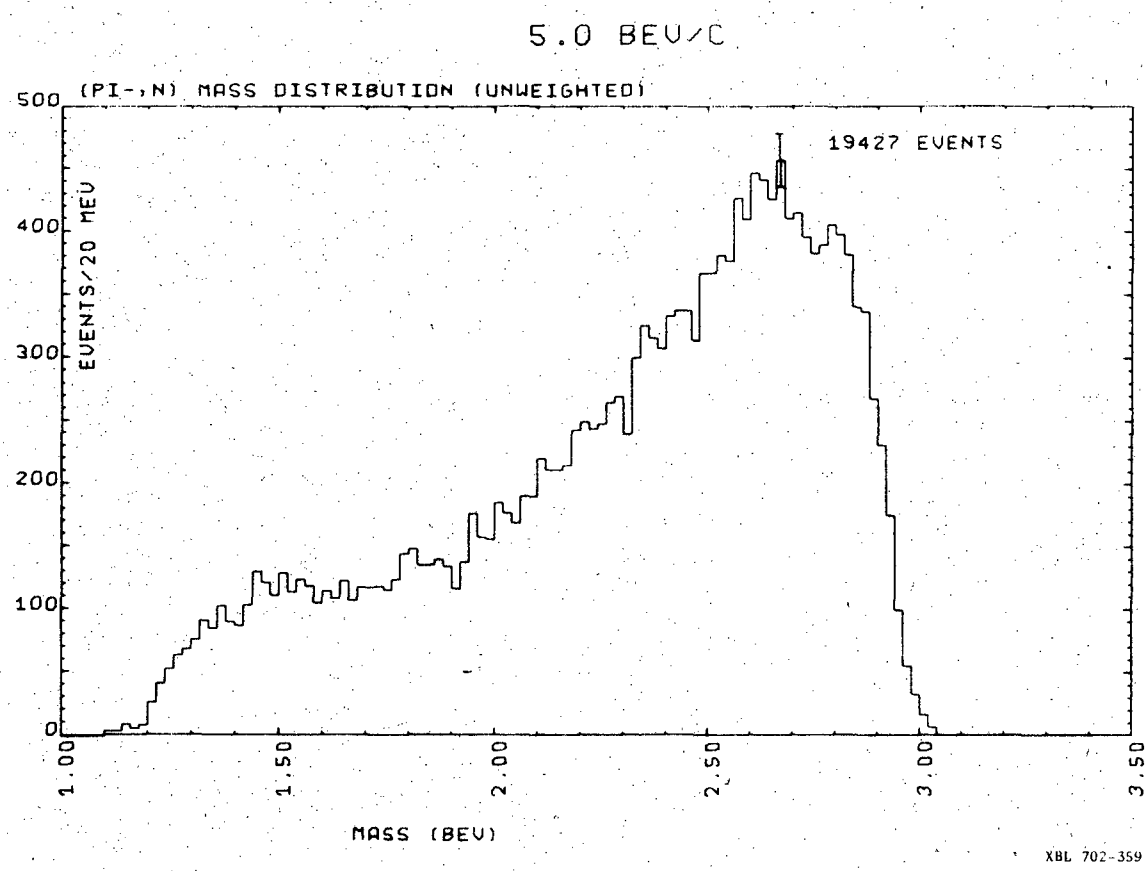
5.0 BEV/C
(PI-,N) MASS DISTRIBUTION (UNWEIGHTED)
19427 EVENTS
EVENTS/20 MEV
500
400
300
200
100
0
1.00
1.50
2.00
2.50
3.00
3.50
MASS (BEV)
XBL 702-359

Fig. 17d

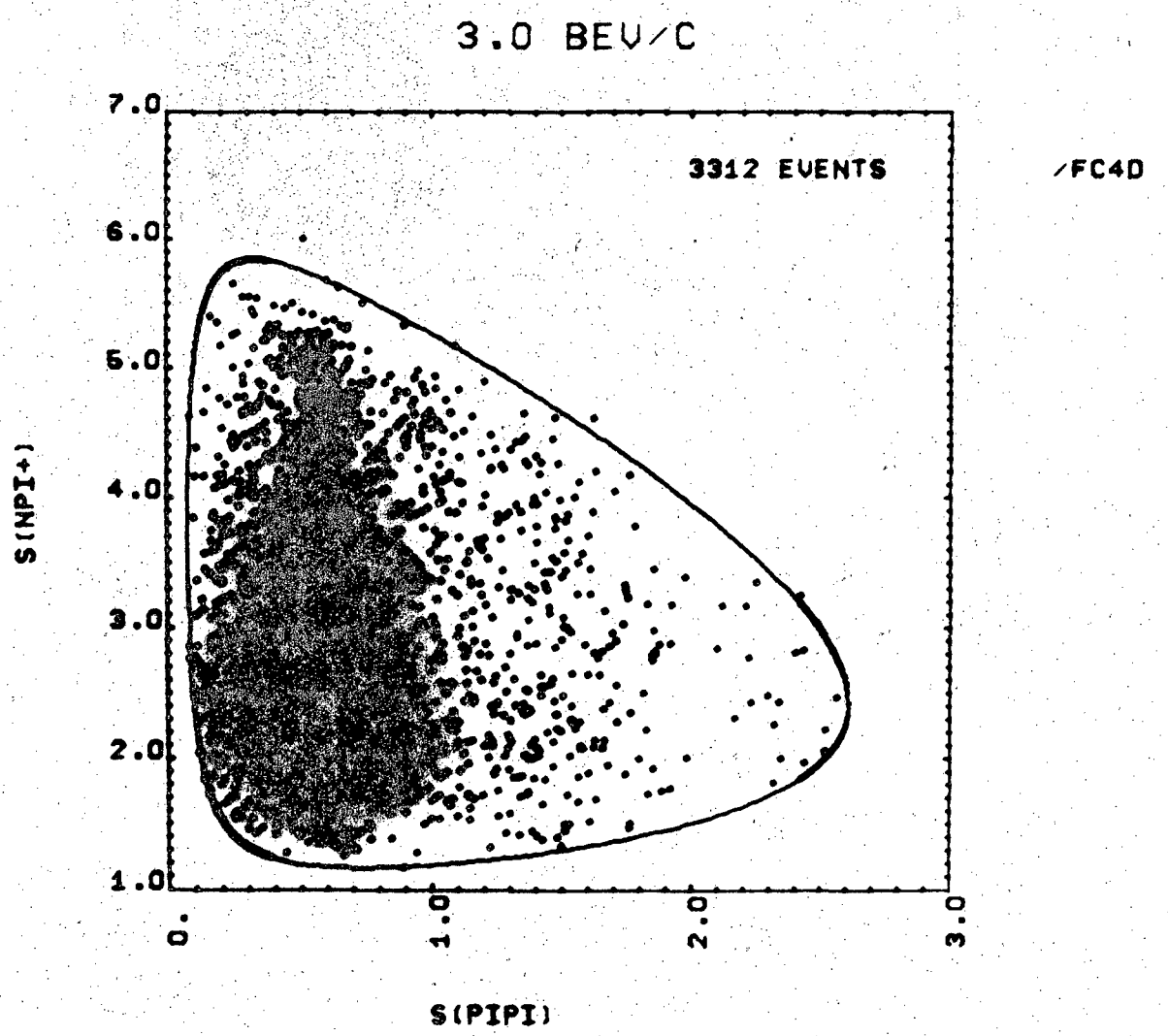
3.0 BEV/C
3312 EVENTS
/FC4D
7.0
6.0
5.0
4.0
3.0
2.0
1.0
S(NPI+)
0.
1.0
2.0
3.0
S(PIPI)

Fig. 18a

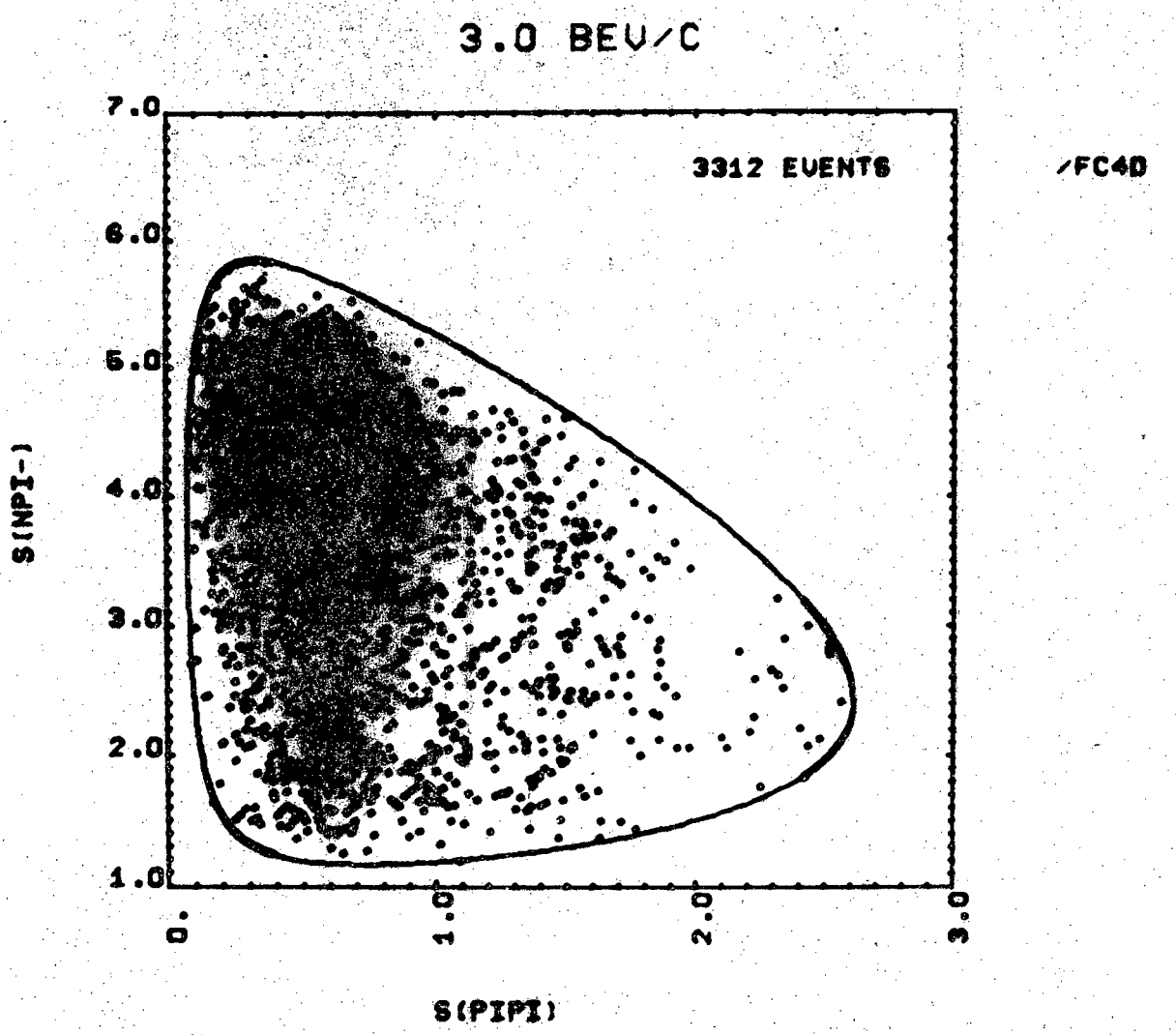
3.0 BEV/C
3312 EVENTS
/FC4D
7.0
6.0
5.0
4.0
3.0
2.0
1.0
S(NPI-)
0.
1.0
2.0
3.0
S(PIPI)

Fig. 18b

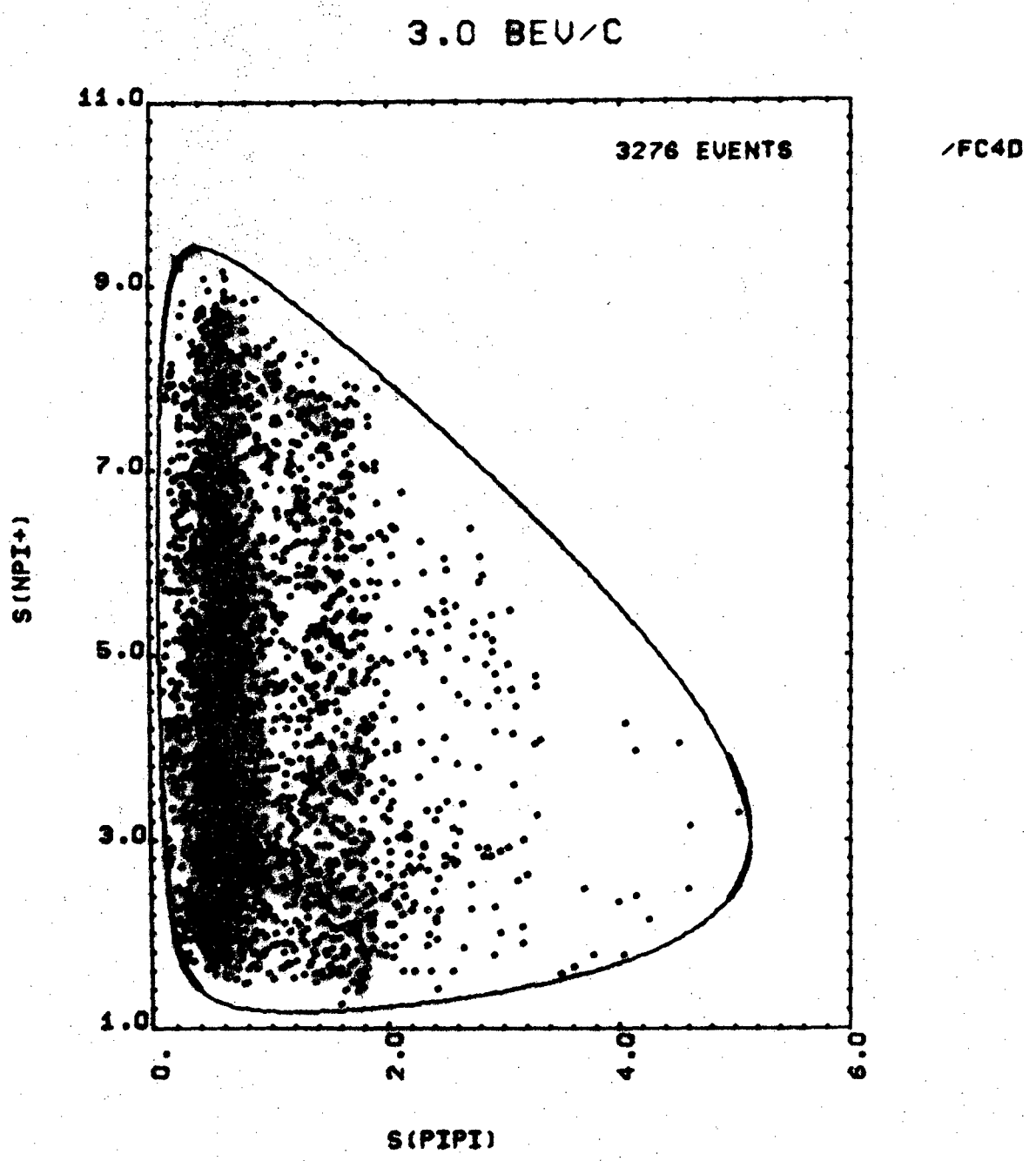

Fig. 18c

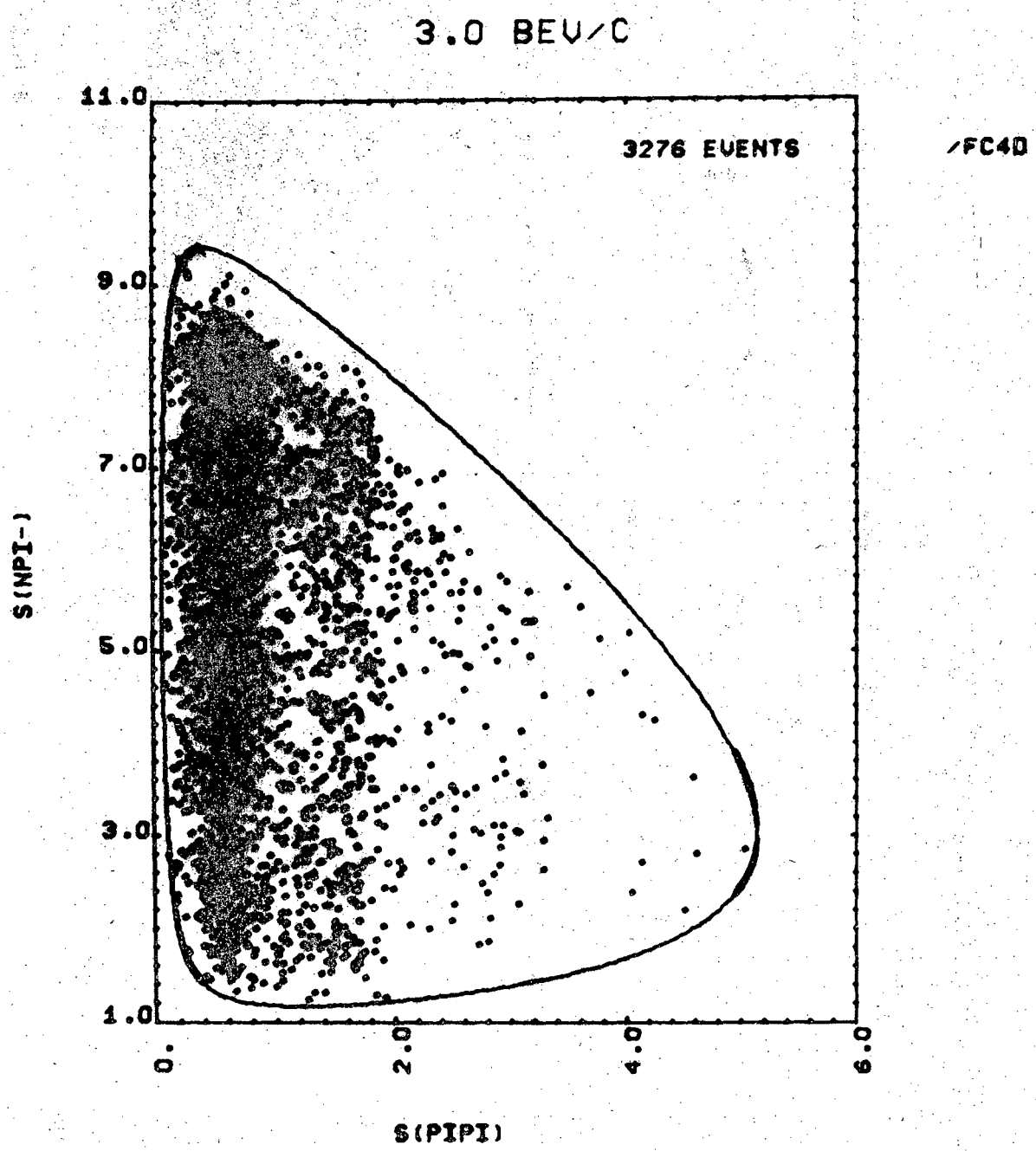

Fig. 18d

Gottfried-Jackson Frame

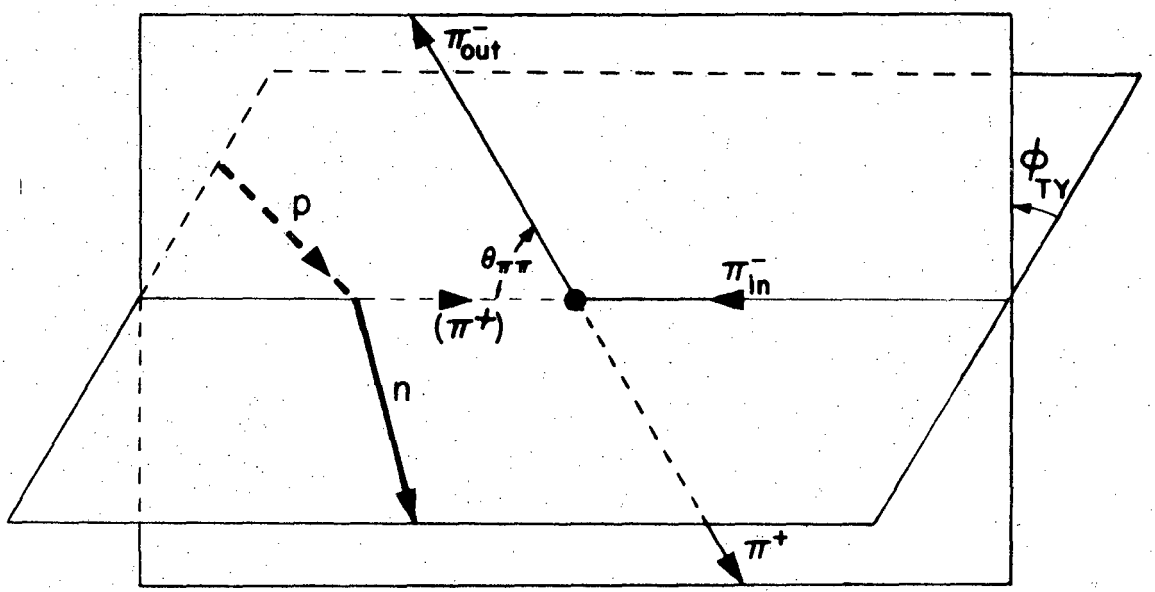

XBL 702-335

Fig. 19

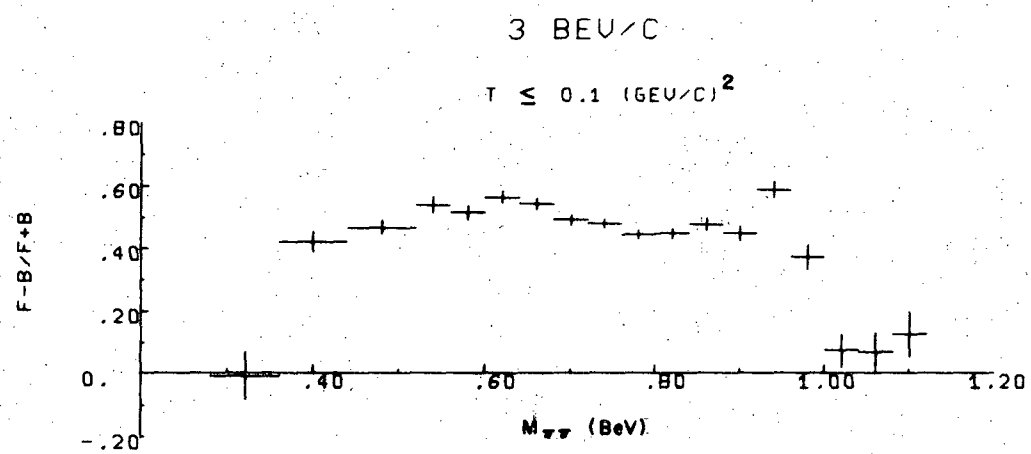

Fig. 20a

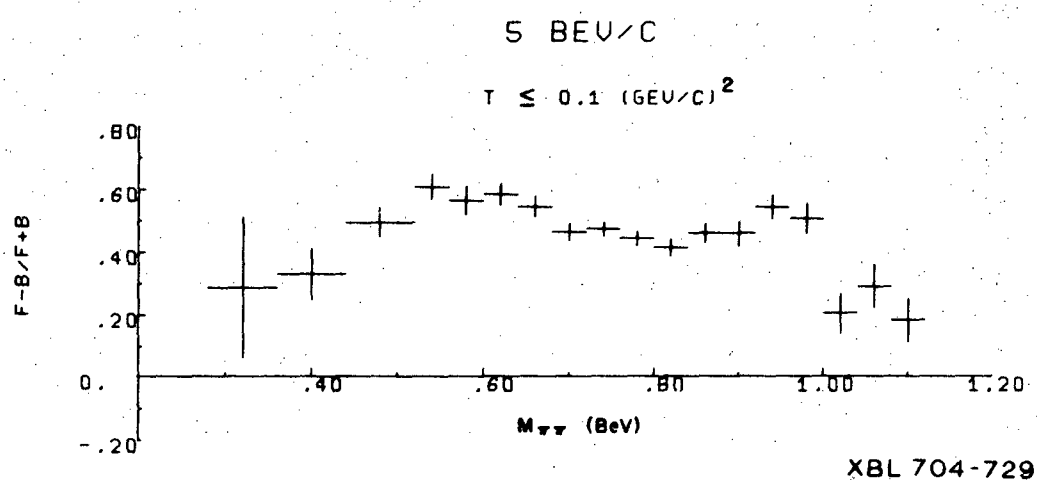

XBL 704-729

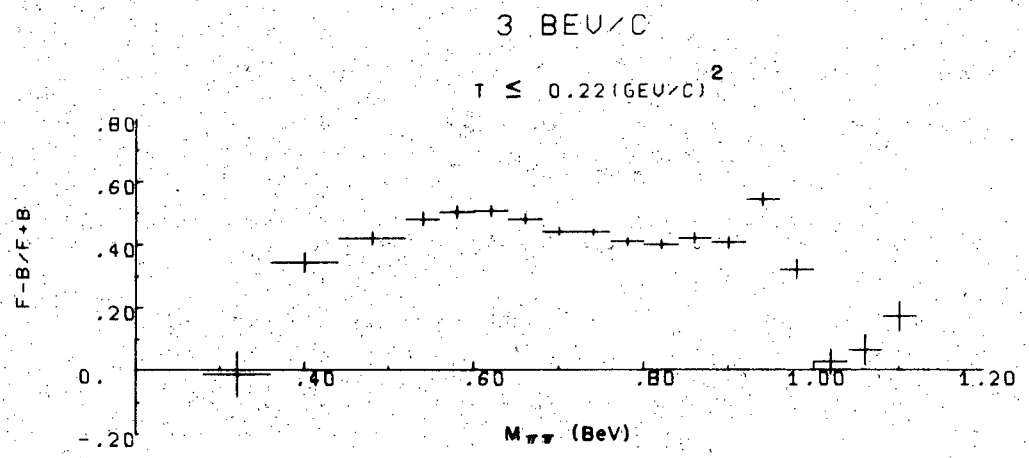
3 BEV/C
T ≤ 0.22(GEV/C)²
F-B/F+B
.80
.60
.40
.20
0.
-.20
.40
.60
.80
1.00
1.20
Mππ (BeV)

Fig. 20b

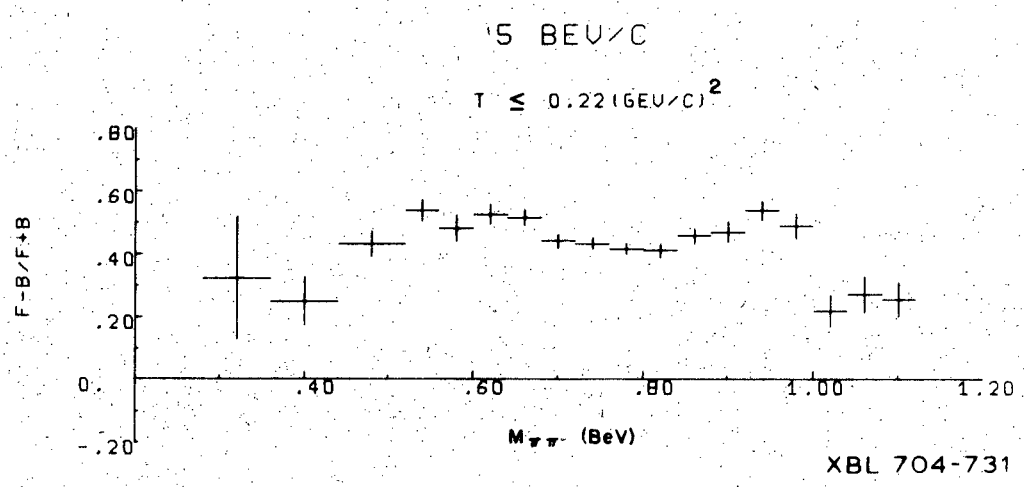
5 BEV/C
T ≤ 0.22(GEV/C)²
F-B/F+B
.80
.60
.40
.20
0.
-.20
.40
.60
.80
1.00
1.20
Mππ (BeV)
XBL 704-731

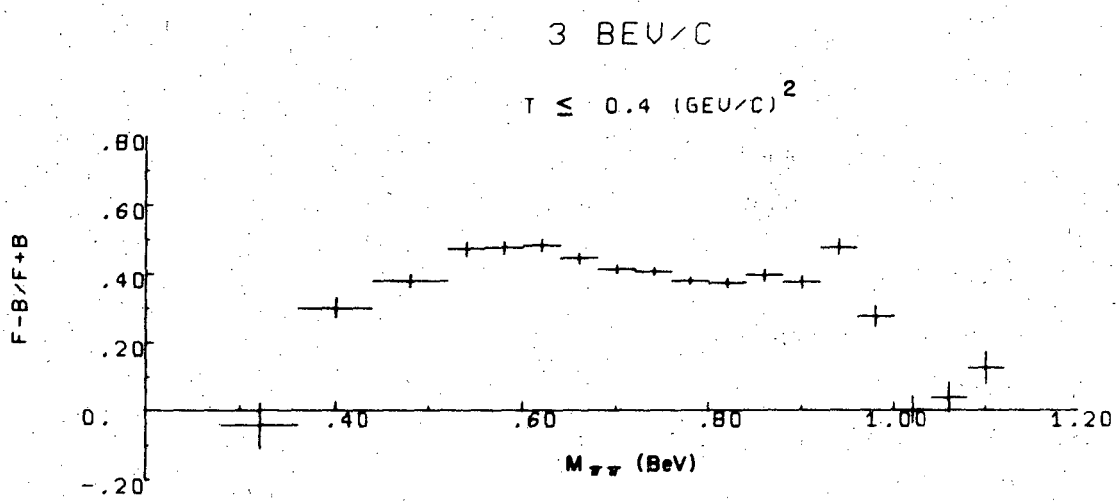

Fig. 20c

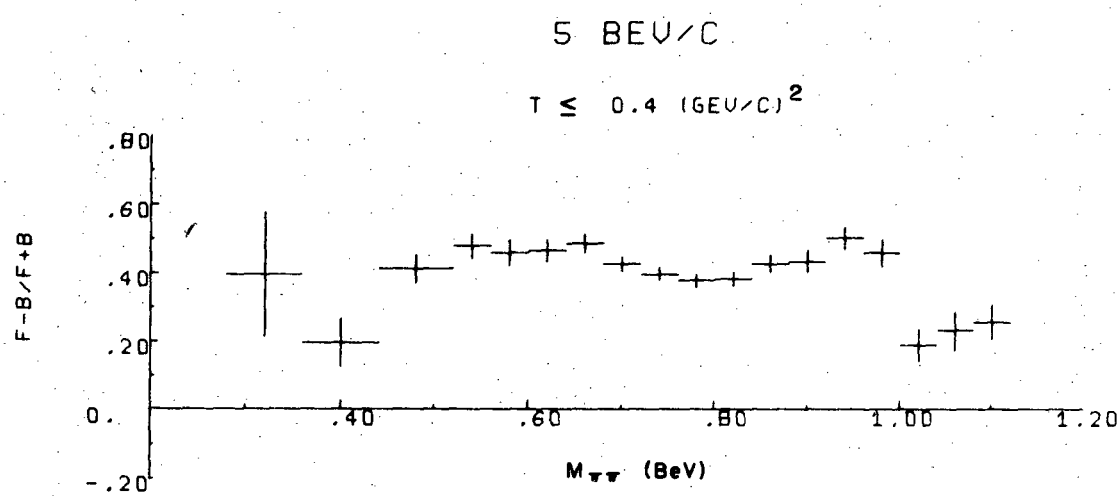

XBL 704-730

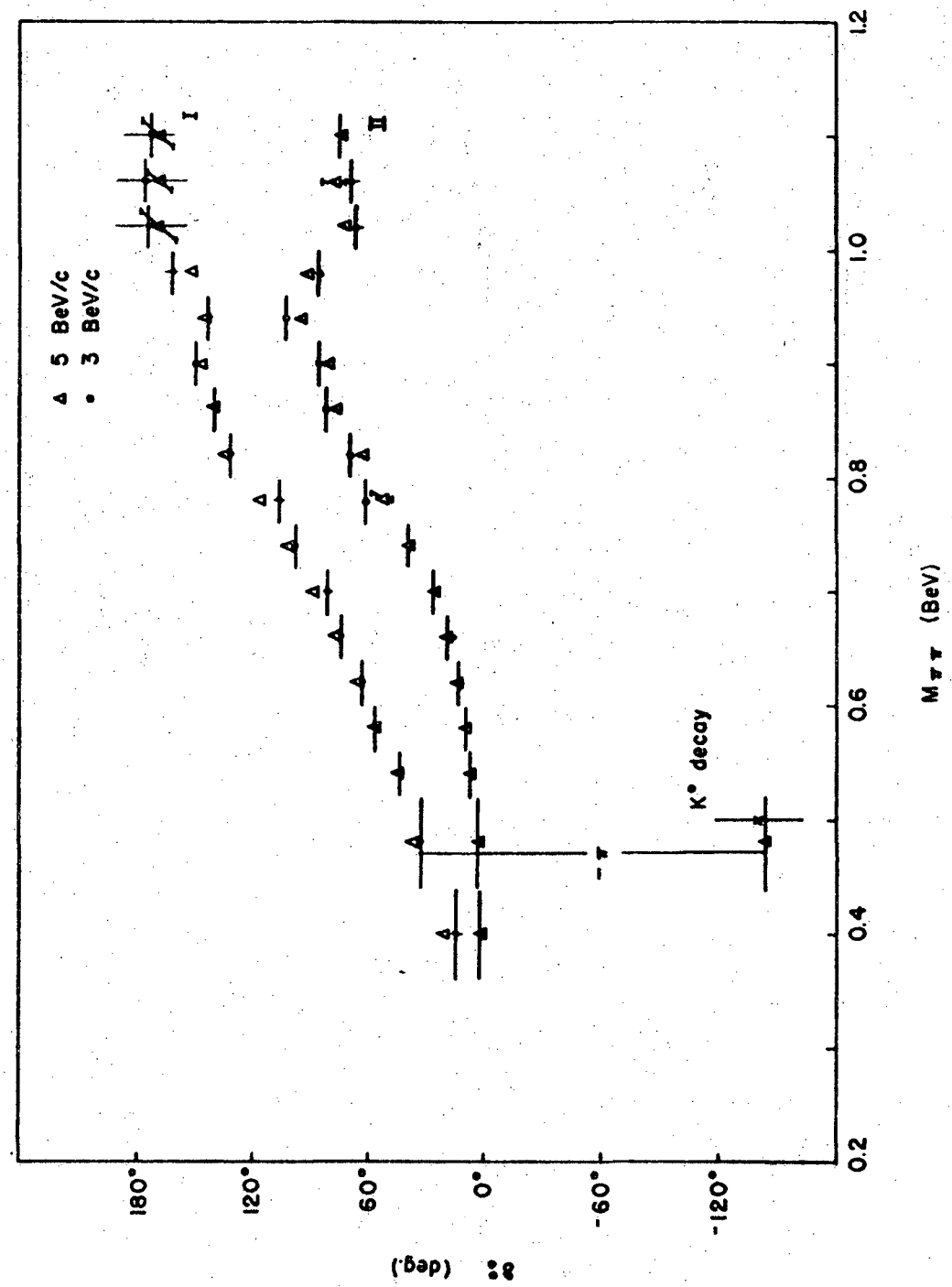
Δ 5 BeV/c
• 3 BeV/c
I
II
K° decay
180°
120°
60°
0°
-60°
-120°
0.2
0.4
0.6
0.8
1.0
1.2
$M_{\pi\pi}$ (BeV)

Fig. 21

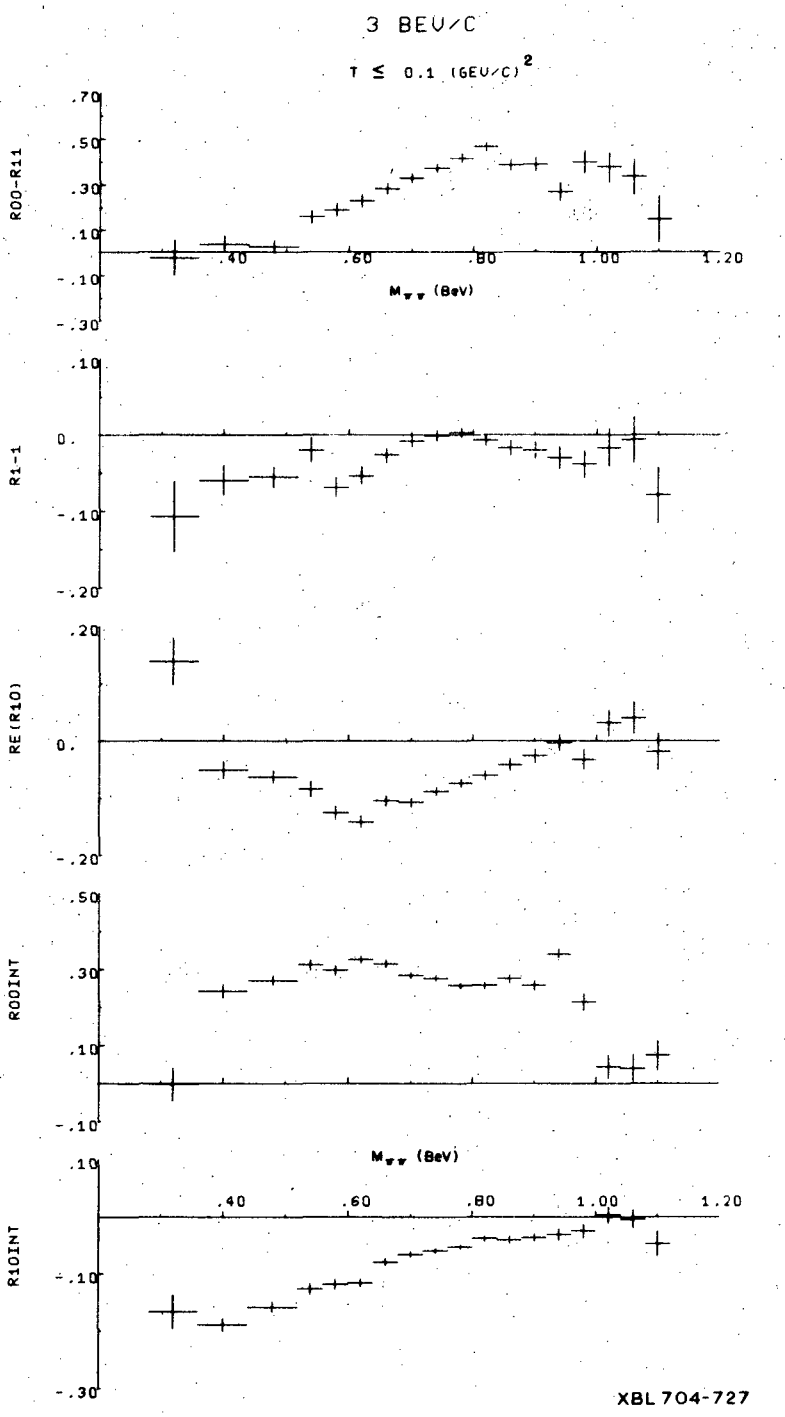
3 BEV/C
T ≤ 0.1 (GEV/C)²
R00-R11
R1-1
RE(R10)
R00INT
R10INT
M_ππ (BeV)
XBL 704-727

Fig. 22a

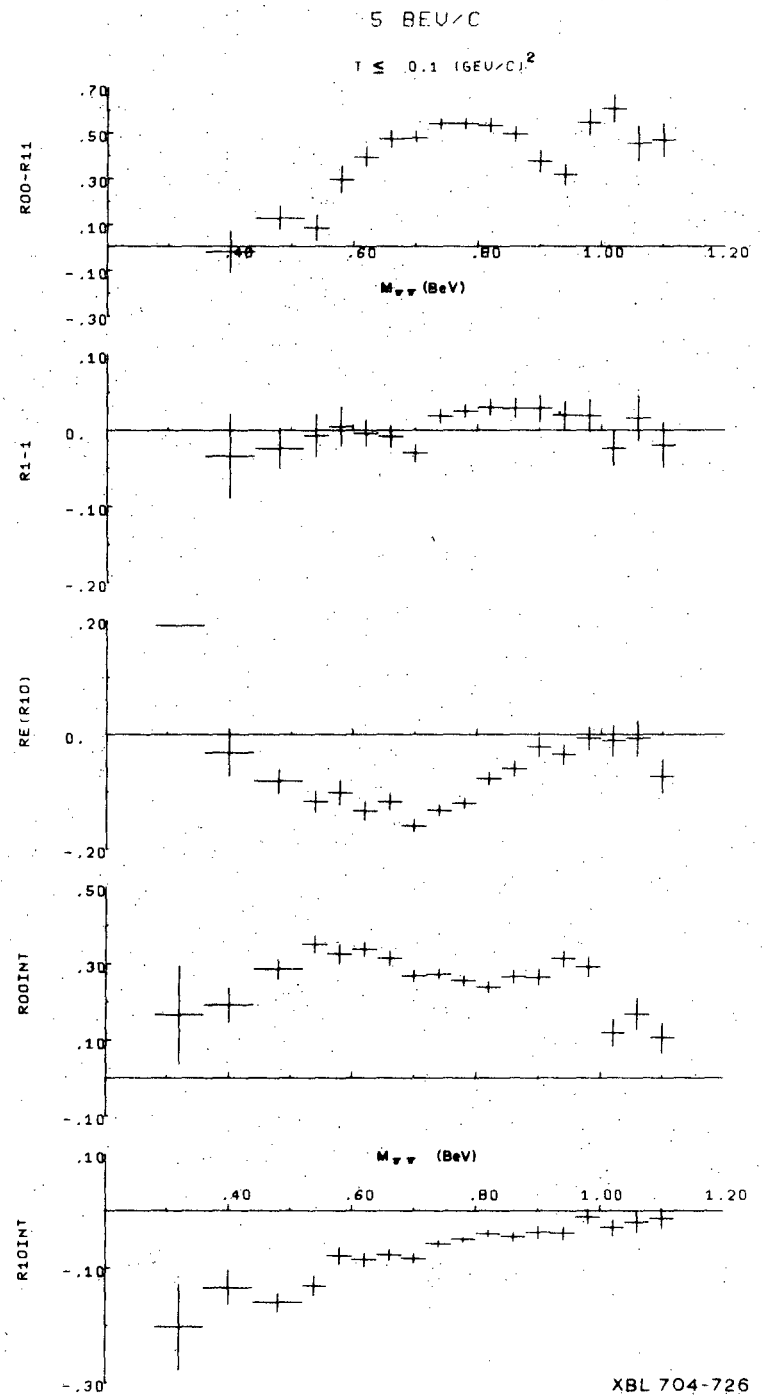
5 BEV/C
T ≤ 0.1 (GEV/C)²
ROO-R11
R1-1
RE(R10)
ROOINT
R10INT
M_ππ (BeV)
.40
.60
.80
1.00
1.20
XBL 704-726

Fig. 22b

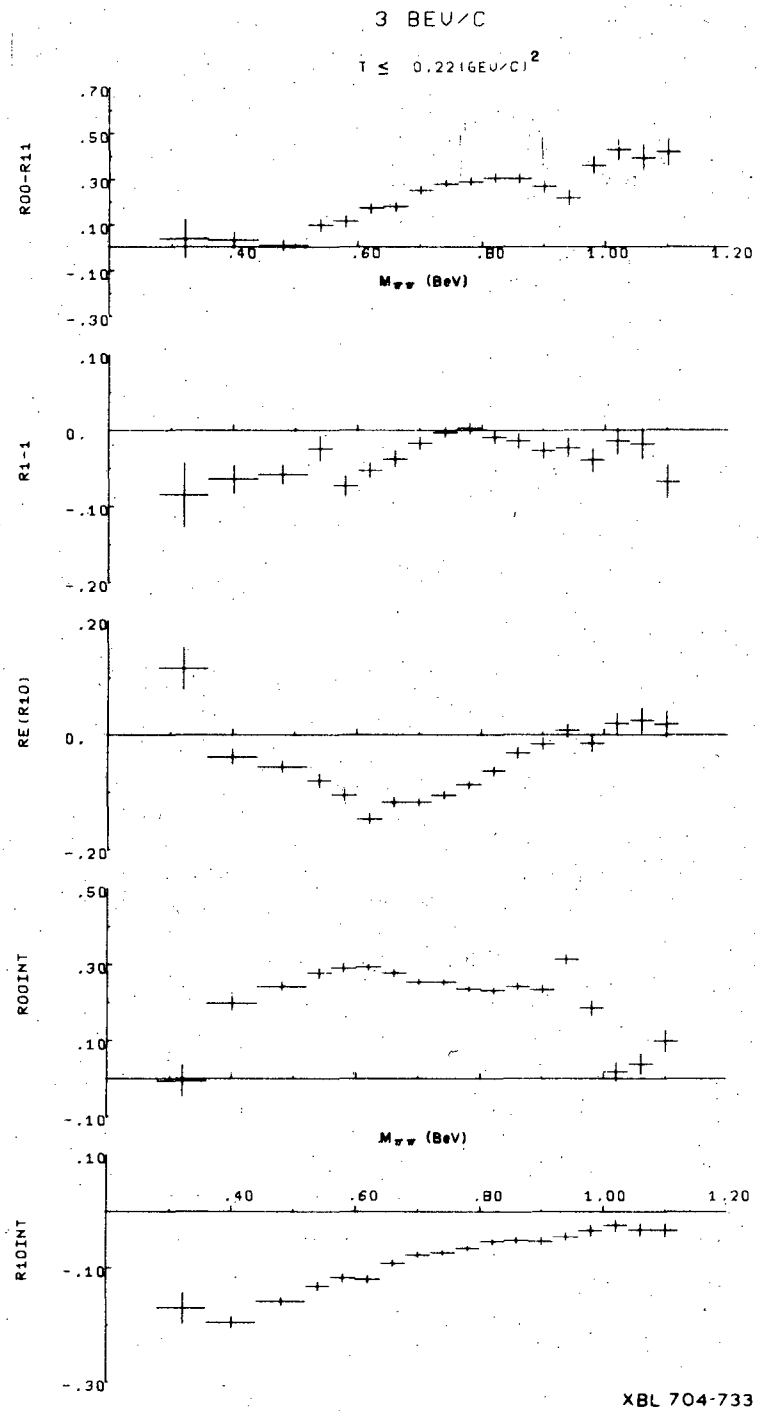
3 BEV/C
T ≤ 0.22(GEV/C)²
R00-R11
R1-1
RE(R10)
R00INT
R10INT
M_ππ (BeV)
XBL 704-733

Fig. 22c

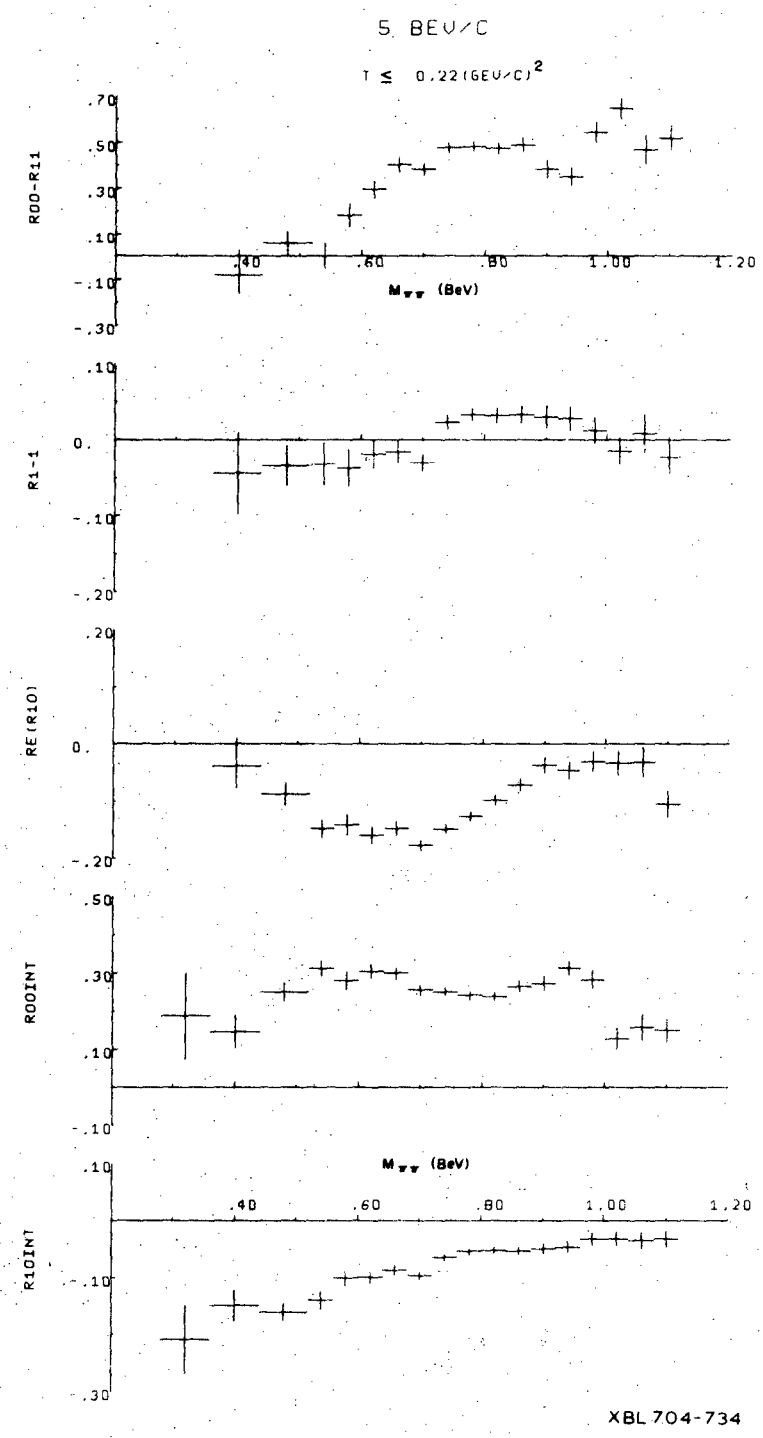
5 BEV/C
T ≤ 0.22(GEV/C)²
R00-R11
.70
.50
.30
.10
-.10
-.30
.40
.60
.80
1.00
1.20
M_ππ (BeV)
R1-1
.10
0.
-.10
-.20
RE(R10)
.20
0.
-.20
R00INT
.50
.30
.10
-.10
M_ππ (BeV)
.40
.60
.80
1.00
1.20
R10INT
.10
-.10
-.30
XBL 704-734

Fig. 22d

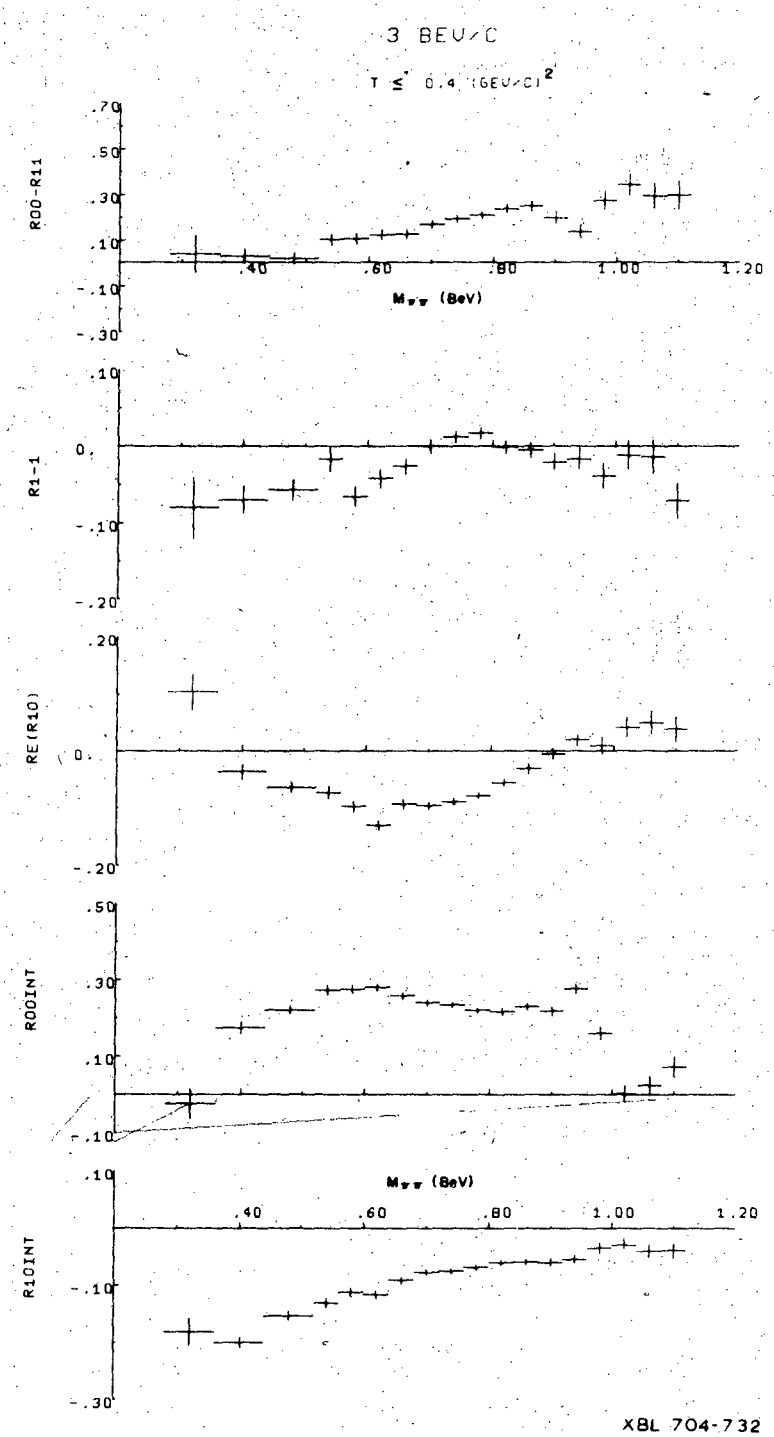
3 BEV/C
T ≤ 0.4 (GEV/C)²
R00-R11
.70
.50
.30
.10
-.10
-.30
.40
.60
.80
1.00
1.20
Mππ (BeV)
R1-1
.10
0.
-.10
-.20
RE(R10)
.20
0.
-.20
R00INT
.50
.30
.10
-.10
Mππ (BeV)
.40
.60
.80
1.00
1.20
R10INT
.10
-.10
-.30
XBL 704-732

Fig. 22e

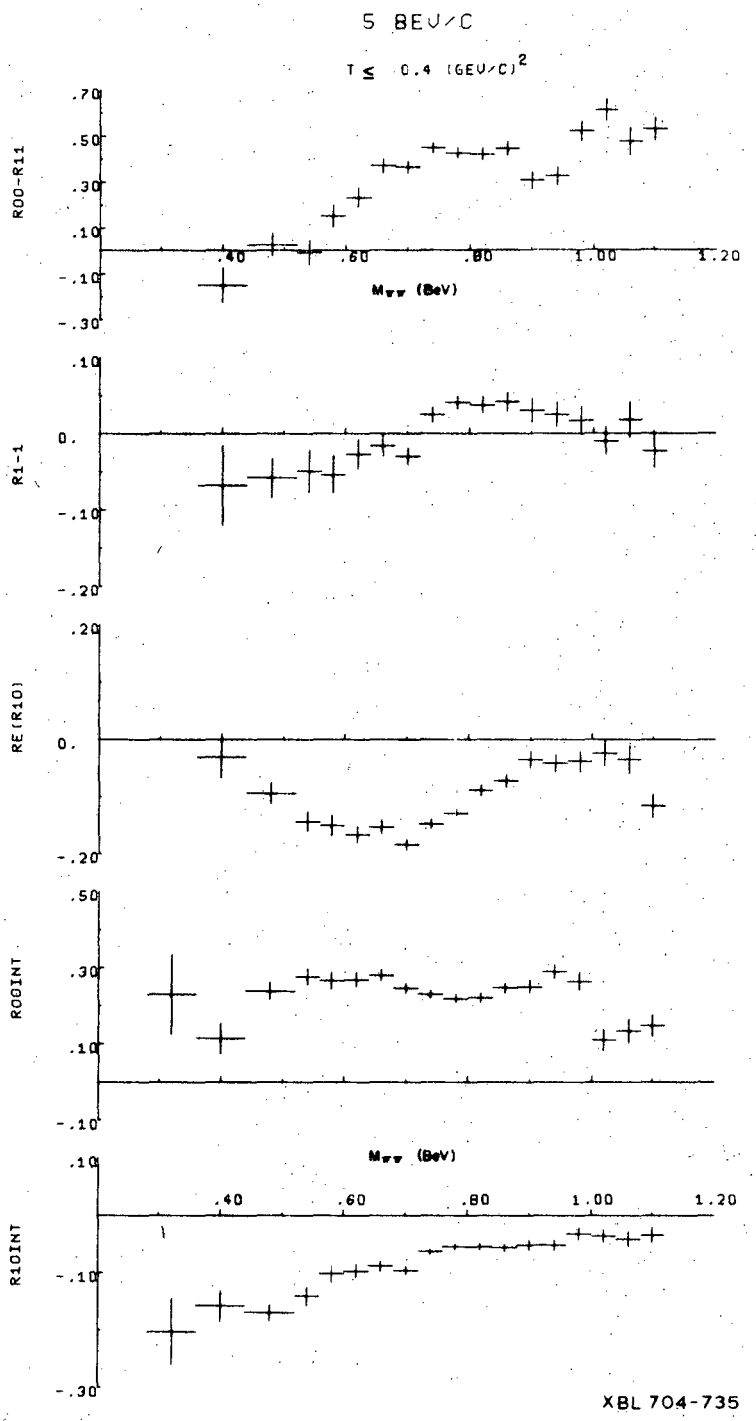
5 BEV/C
T ≤ 0.4 (GEV/C)²
ROO-R11
R1-1
RE(R10)
ROOINT
R10INT
Mππ (BeV)
.40
.60
.80
1.00
1.20
XBL 704-735

Fig. 22f

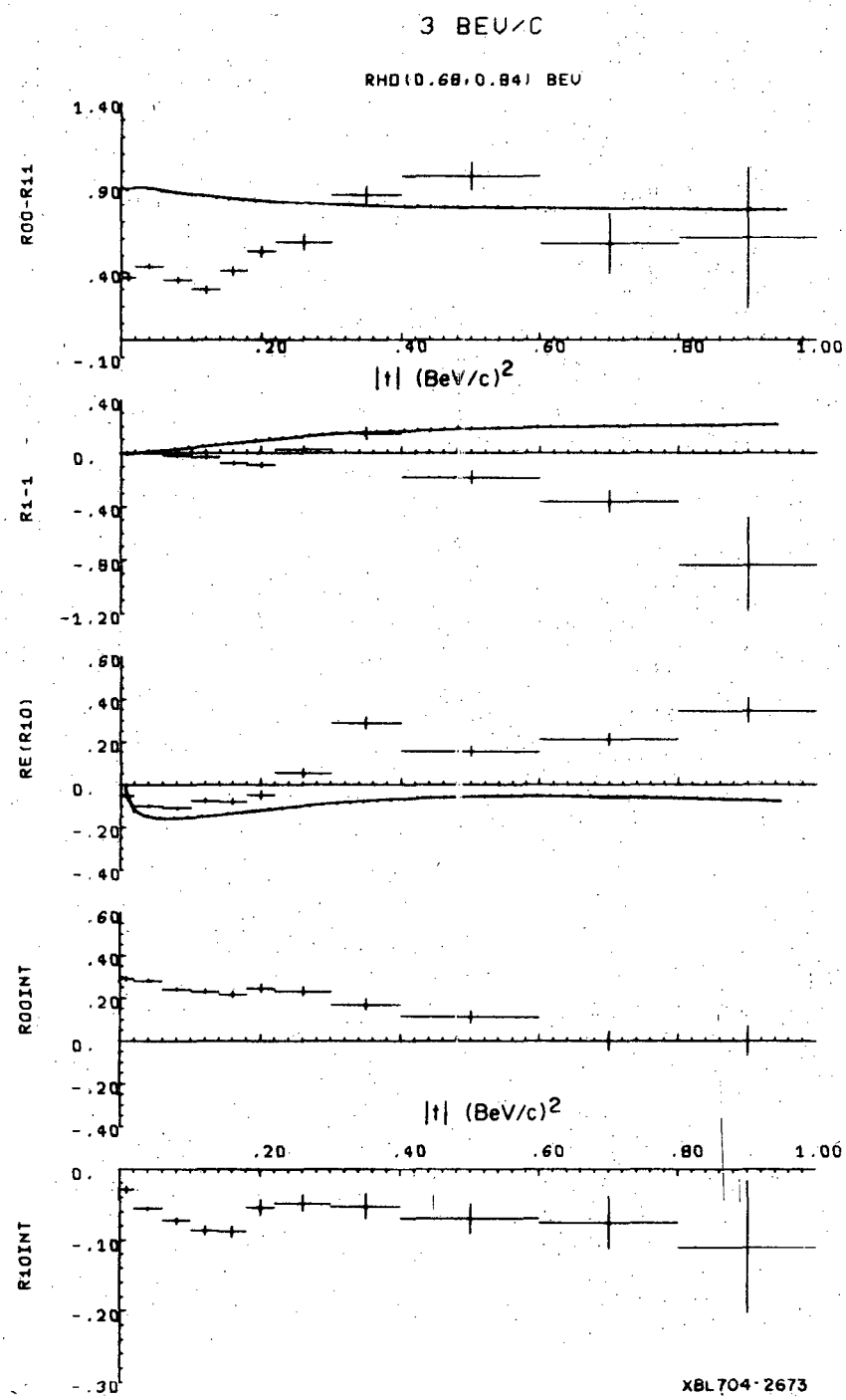
3 BEV/C
RHO(0.68,0.84) BEV
R00-R11
1.40
.90
.40
-.10
.20
.40
.60
.80
1.00
|t| (BeV/c)2
R1-1
.40
0.
-.40
-.80
-1.20
RE(R10)
.60
.40
.20
0.
-.20
-.40
R00INT
.60
.40
.20
0.
-.20
-.40
|t| (BeV/c)2
.20
.40
.60
.80
1.00
R10INT
0.
-.10
-.20
-.30
XBL704-2673

Fig. 23a

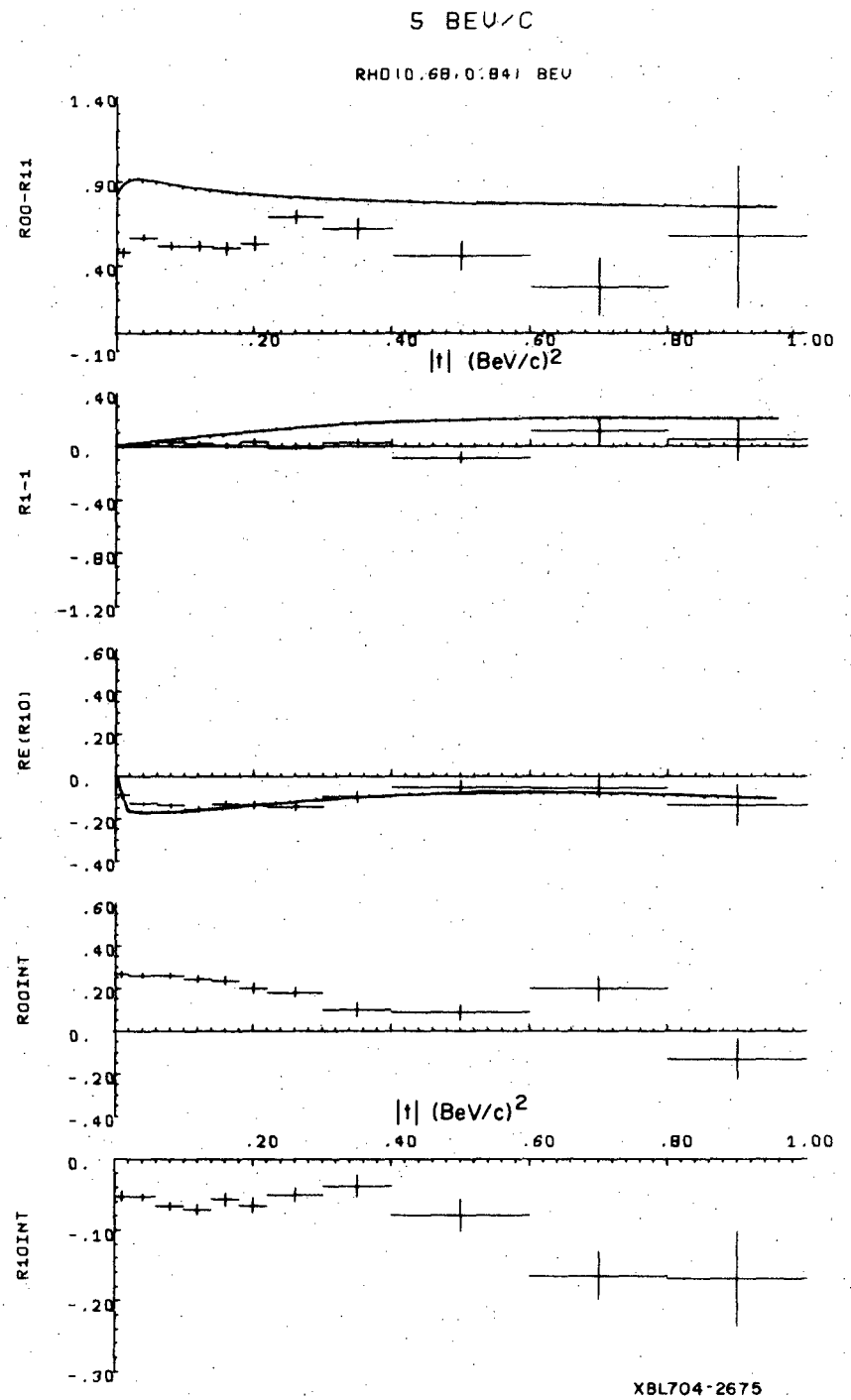
5 BEV/C
RHO(0.68,0.84) BEV
R00-R11
R1-1
RE(R10)
R00INT
R10INT
|t| (BeV/c)^2
XBL704-2675

Fig. 23b

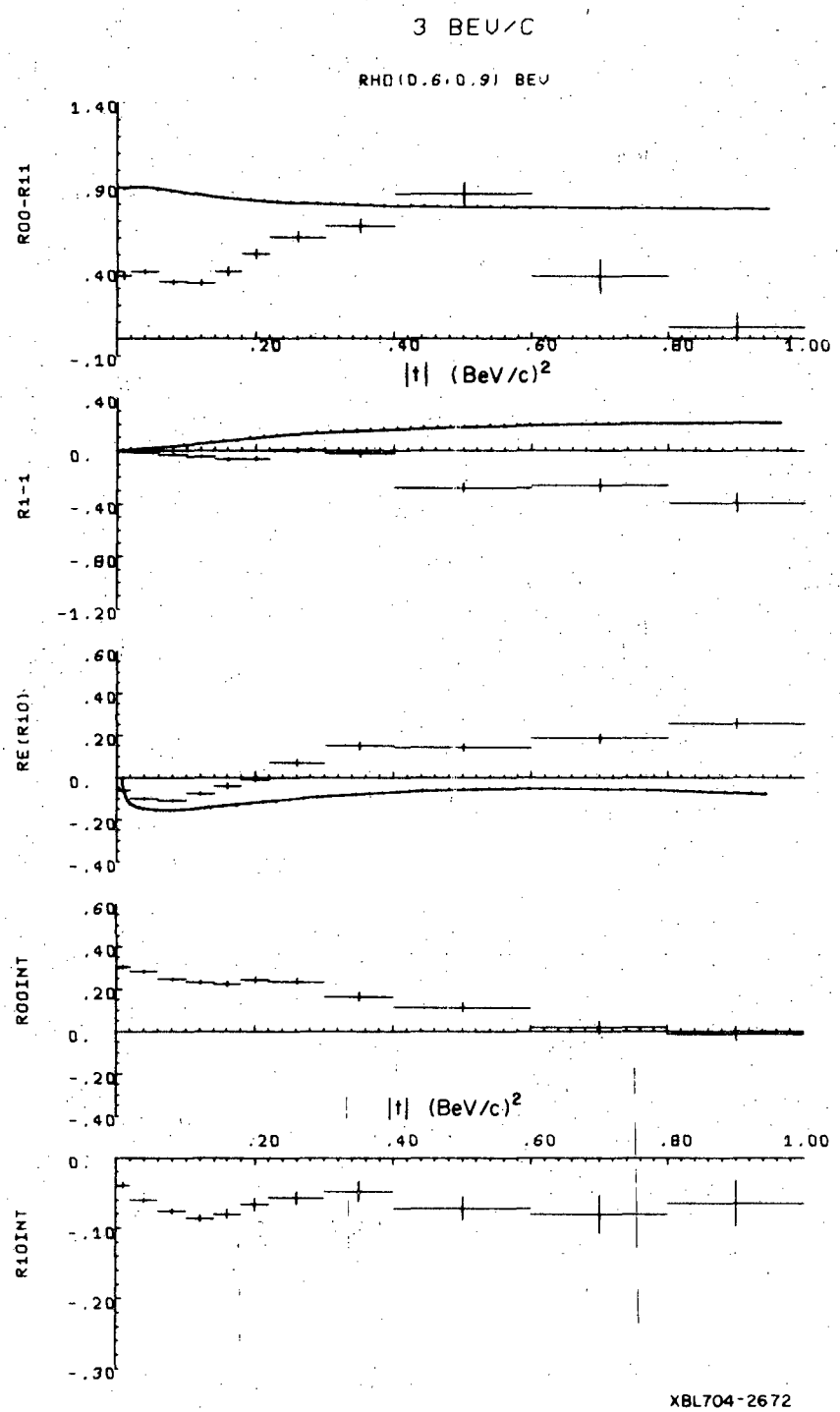
3 BEV/C
RHO(0.6,0.9) BEV
R00-R11
1.40
.90
.40
-.10
.20
.40
.60
.80
1.00
|t| (BeV/c)^2
R1-1
.40
0.
-.40
-.80
-1.20
RE(R10)
.60
.40
.20
0.
-.20
-.40
R00INT
.60
.40
.20
0.
-.20
-.40
|t| (BeV/c)^2
.20
.40
.60
.80
1.00
R10INT
0.
-.10
-.20
-.30
XBL704-2672

Fig. 24a

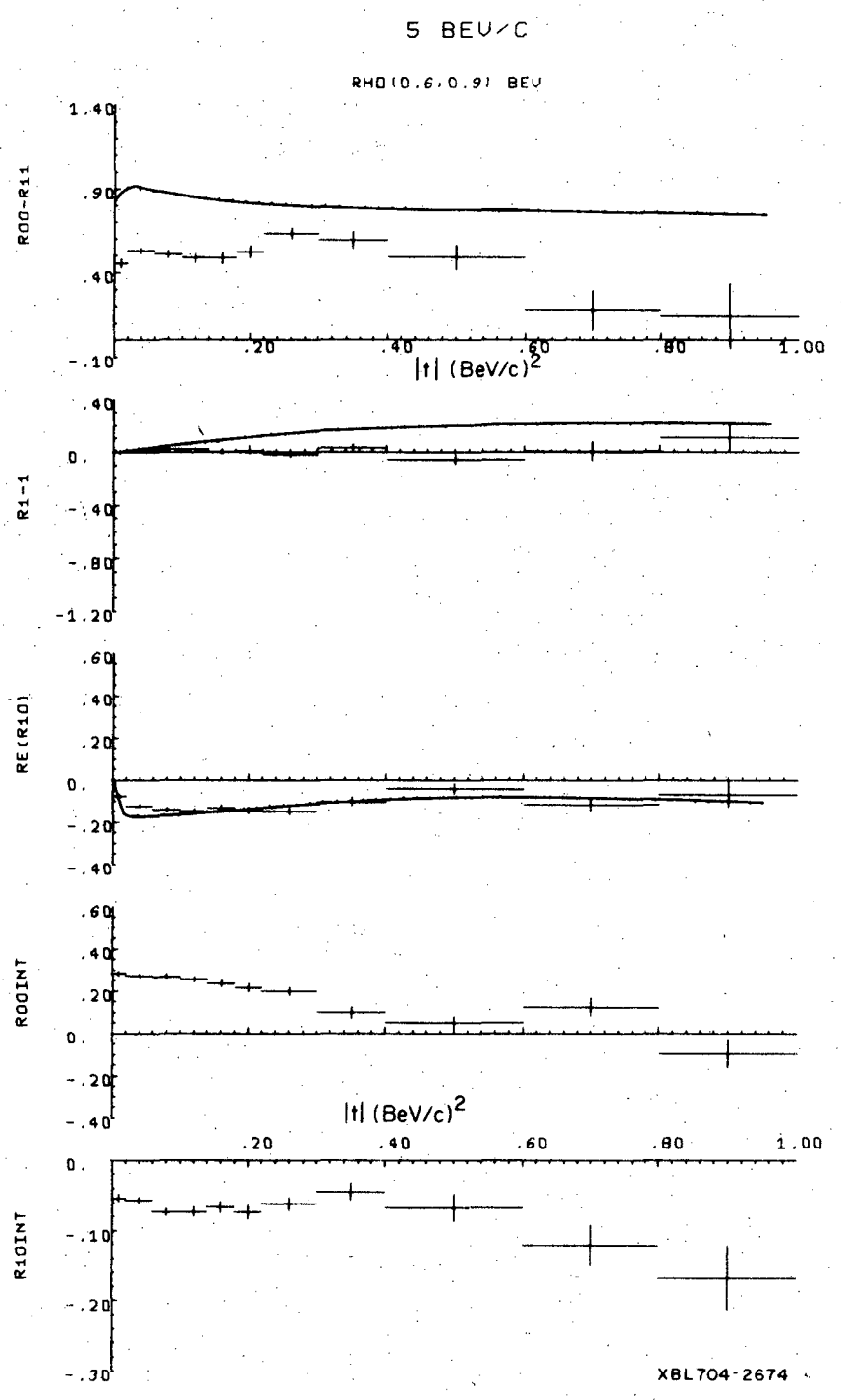
5 BEV/C
RHO(0.6,0.91 BEV
R00-R11
1.40
.90
.40
-.10
.20
.40
.60
.80
1.00
|t| (BeV/c)^2
R1-1
.40
0.
-.40
-.80
-1.20
RE(R10)
.60
.40
.20
0.
-.20
-.40
R00INT
.60
.40
.20
0.
-.20
-.40
|t| (BeV/c)^2
.20
.40
.60
.80
1.00
R10INT
0.
-.10
-.20
-.30
XBL704-2674

Fig. 24b

3 BEV/C

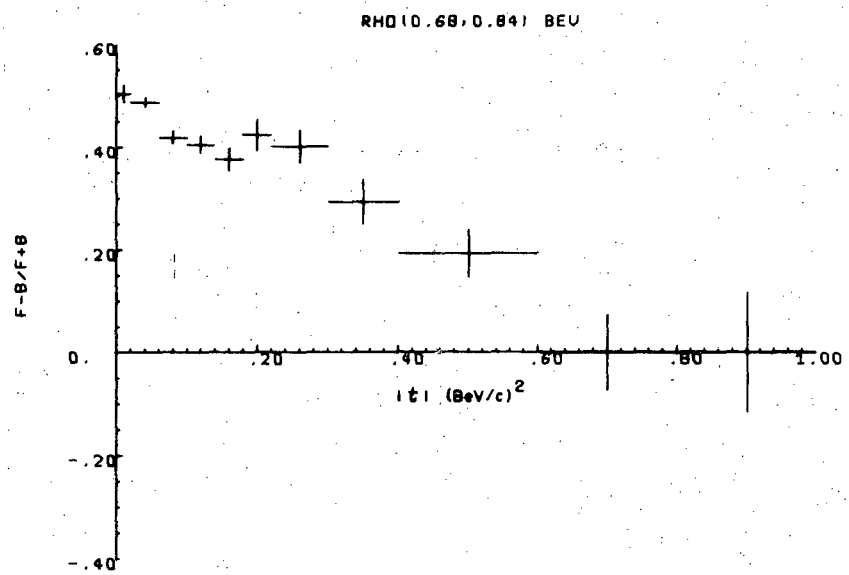

Fig. 25a

5 BEV/C

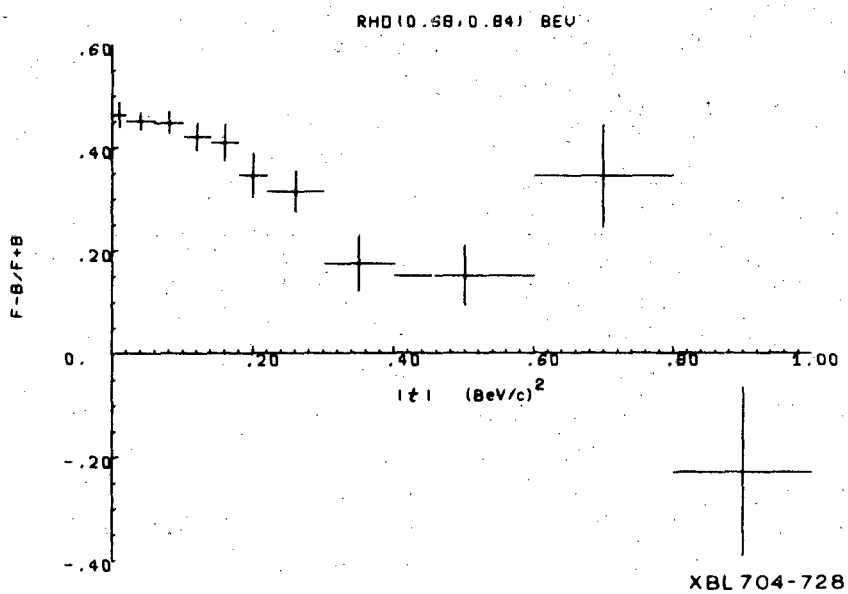

XBL 704-728

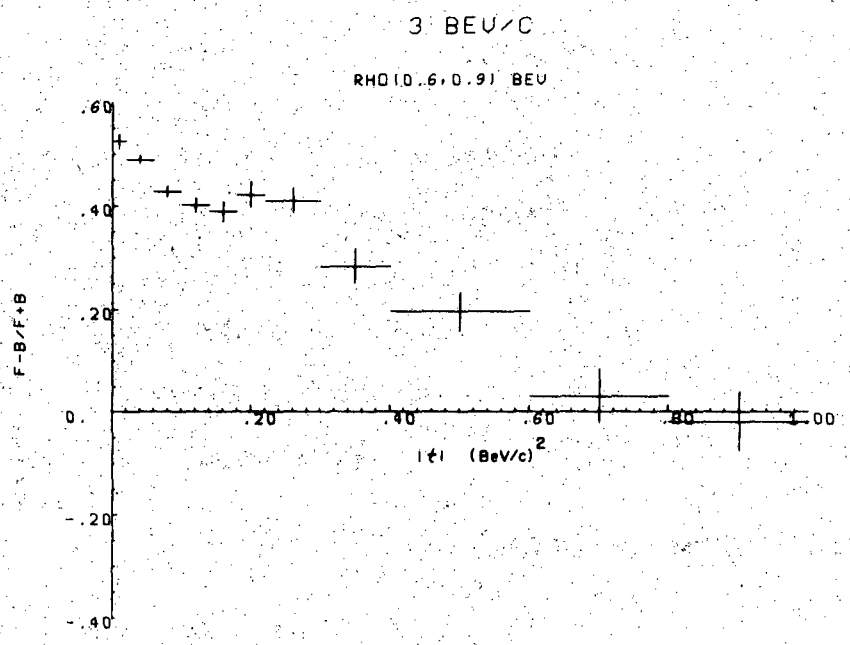

Fig. 25b

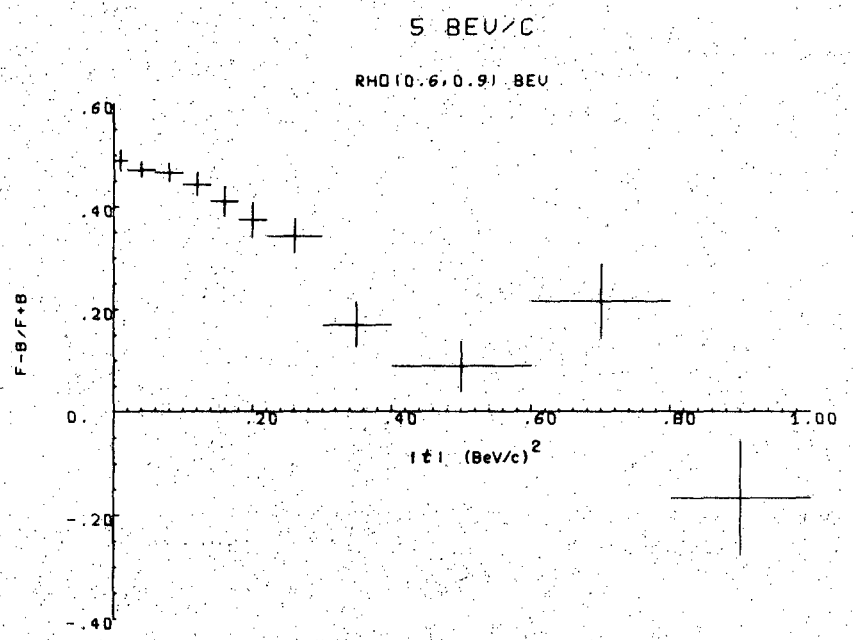

XBL 704-736

3 BEV/C

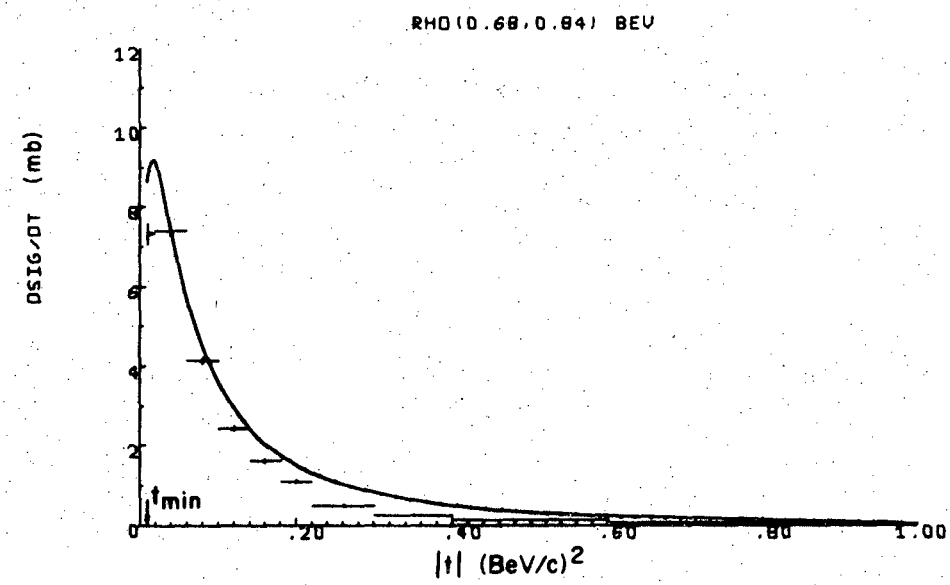

Fig. 26

5 BEV/C

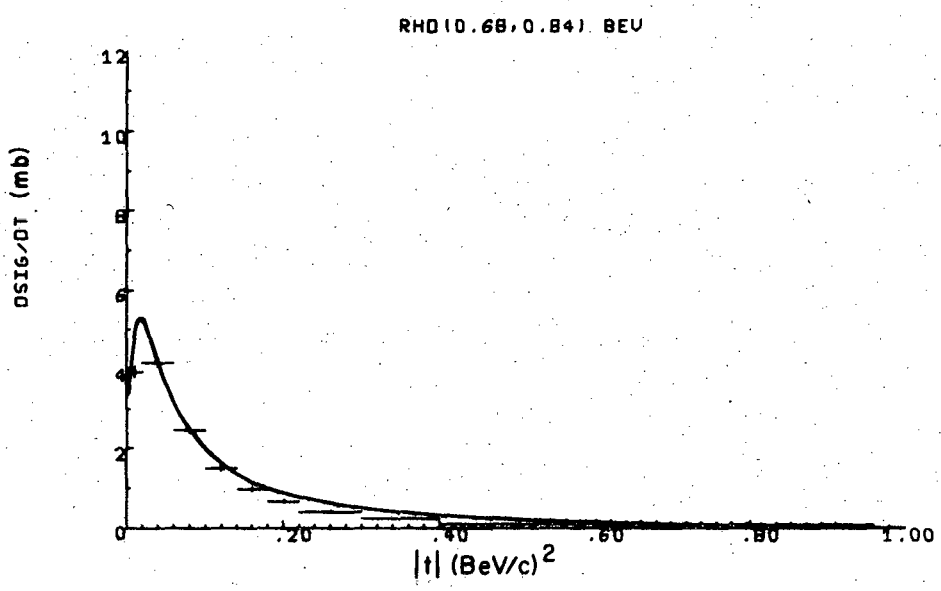

XBL704-2676

3 BEV/C

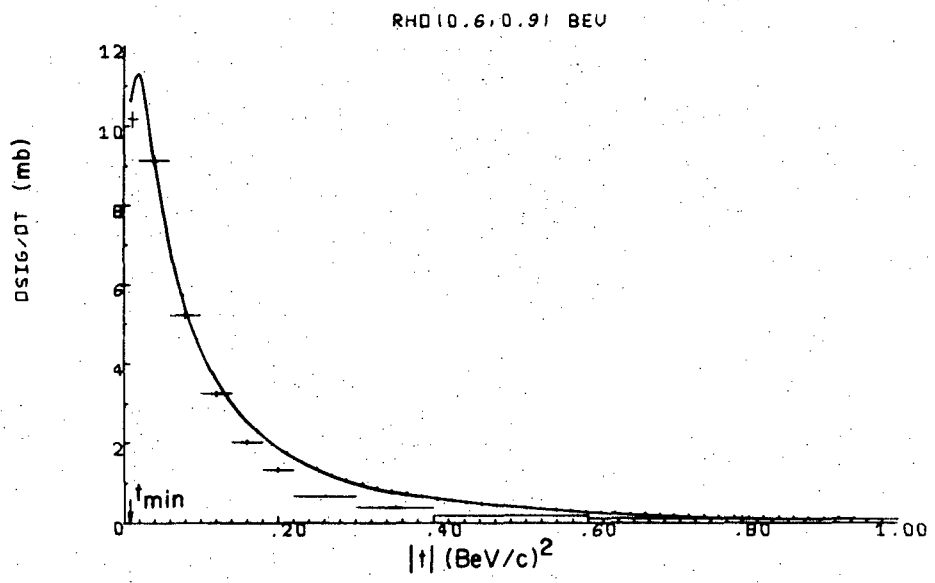

Fig. 27

5 BEV/C

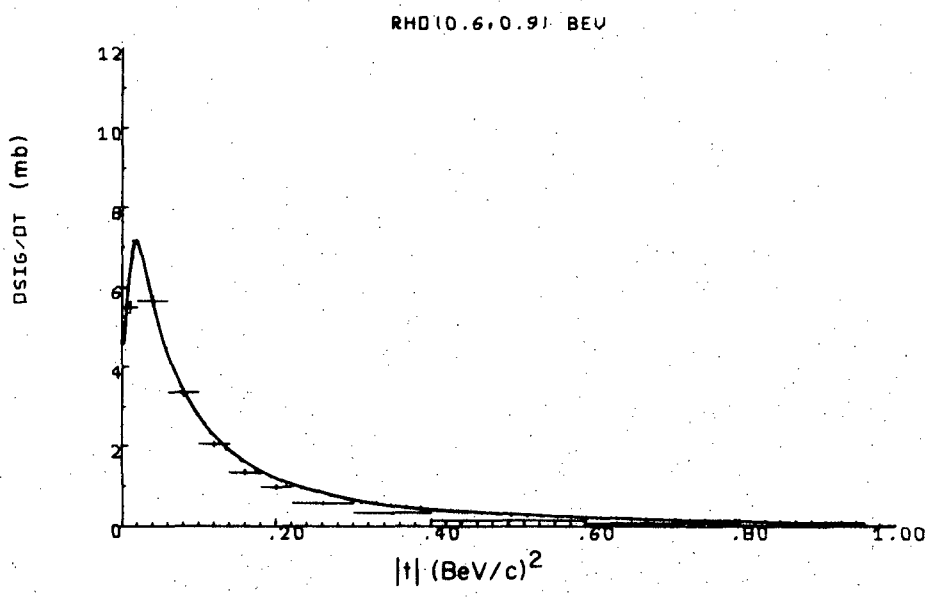

XBL704-2671

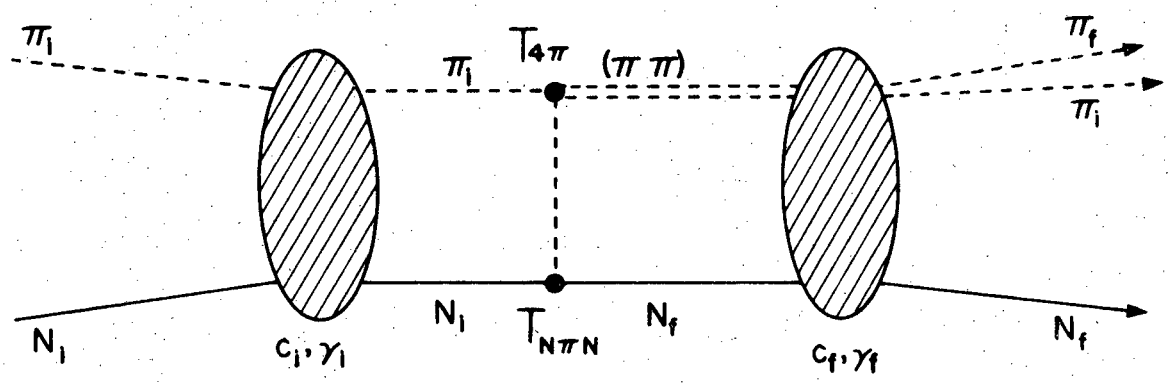

XBL 702-337

Fig. 28

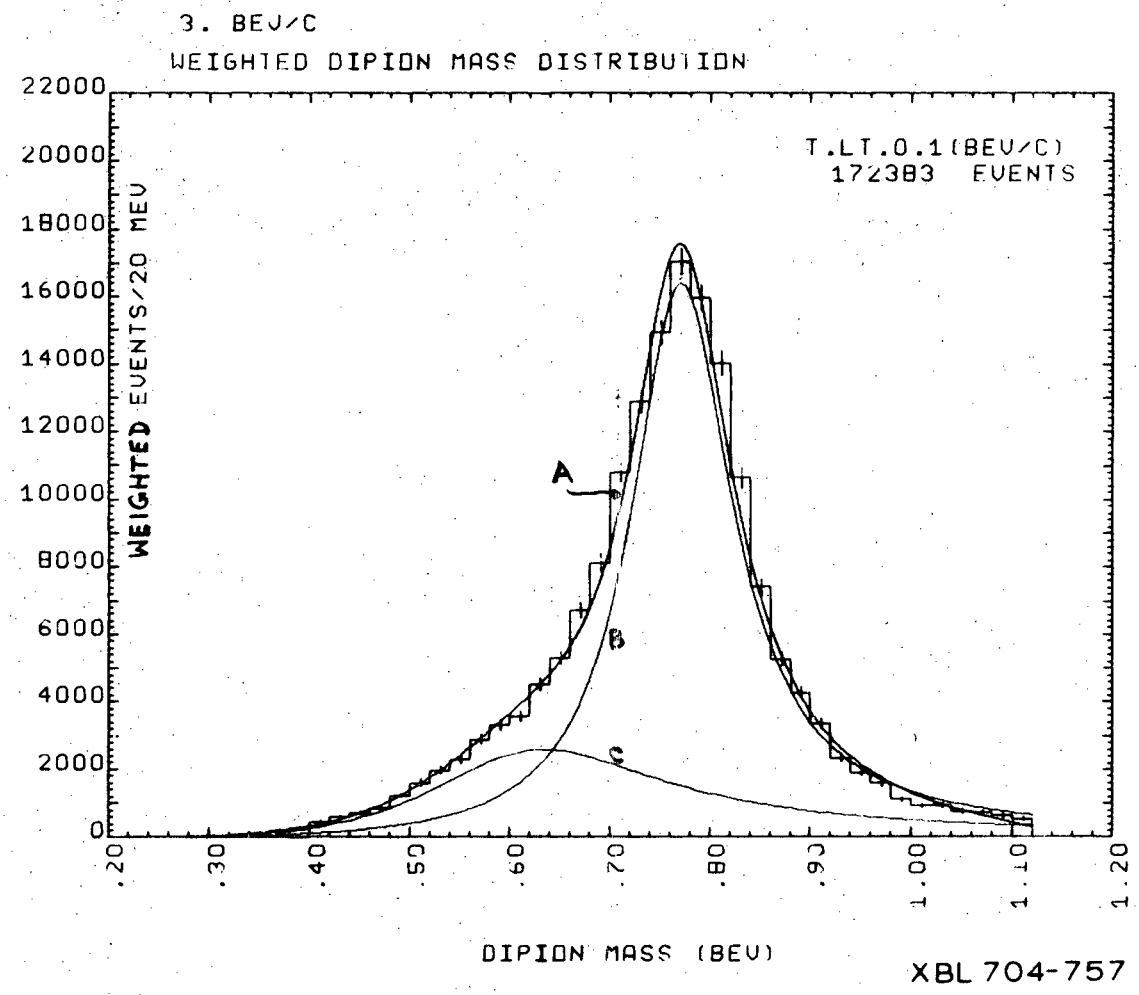
3. BEV/C
WEIGHTED DIPION MASS DISTRIBUTION
T.LT.0.1(BEV/C)
172383 EVENTS
WEIGHTED EVENTS/20 MEV
22000
20000
18000
16000
14000
12000
10000
8000
6000
4000
2000
0
A
B
C
.20
.30
.40
.50
.60
.70
.80
.90
1.00
1.10
1.20
DIPION MASS (BEV)
XBL 704-757

Fig. 29a

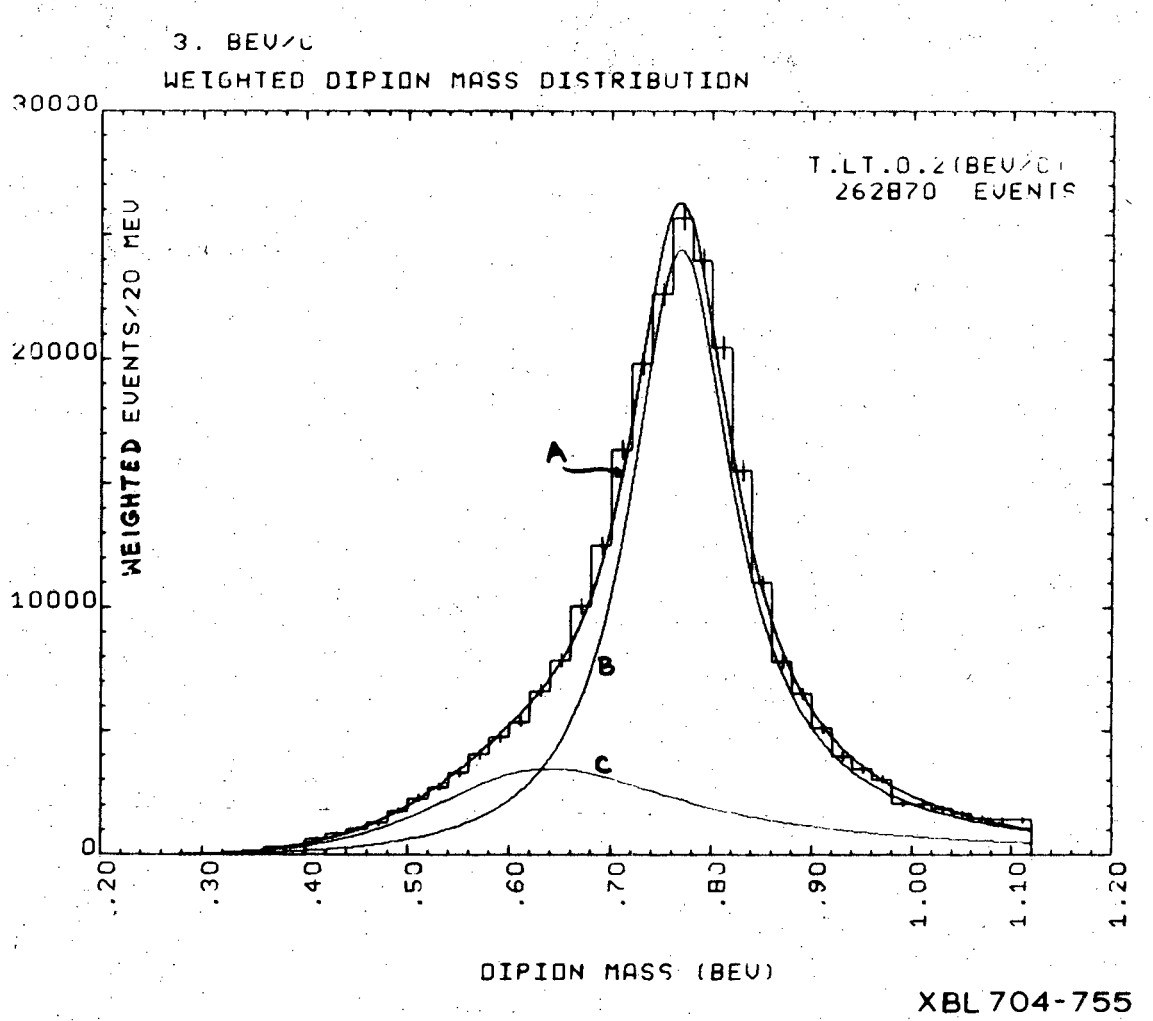
3. BEV/C
WEIGHTED DIPION MASS DISTRIBUTION
T.LT.0.2(BEV/C)
262870 EVENTS
WEIGHTED EVENTS/20 MEV
30000
20000
10000
0
A
B
C
.20
.30
.40
.50
.60
.70
.80
.90
1.00
1.10
1.20
DIPION MASS (BEV)
XBL 704-755

Fig. 29b

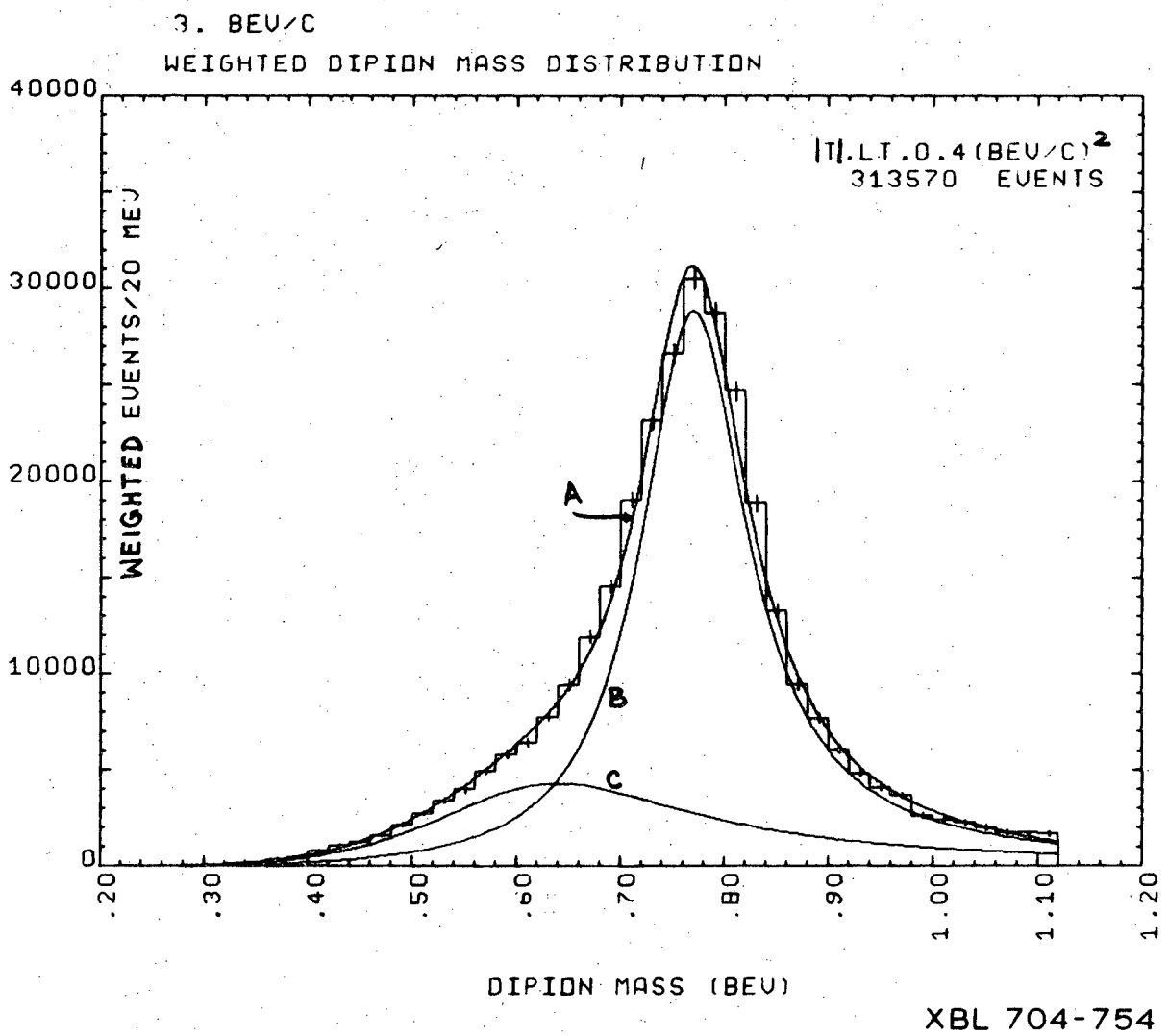

XBL 704-754

Fig. 29c

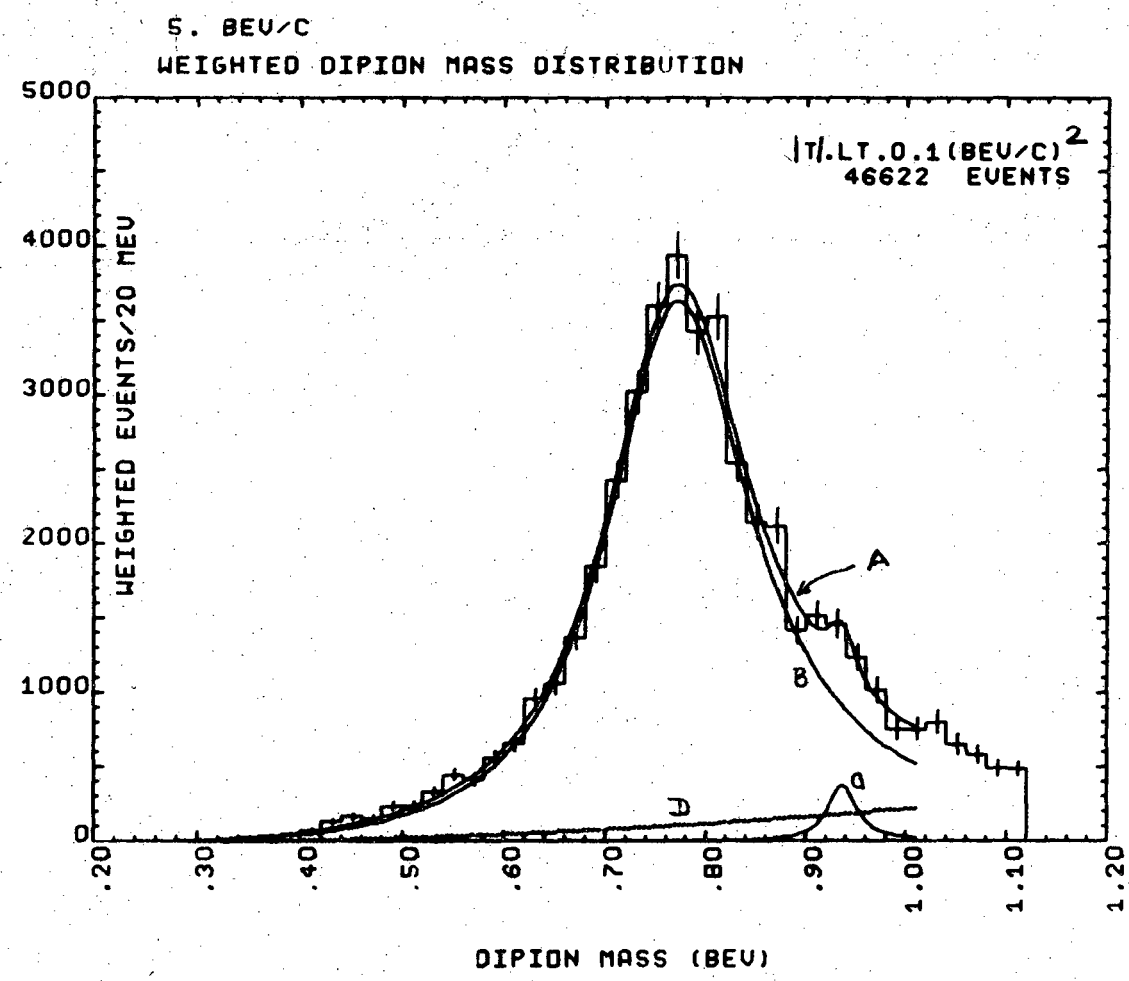

XBL 704-790

Fig. 30a

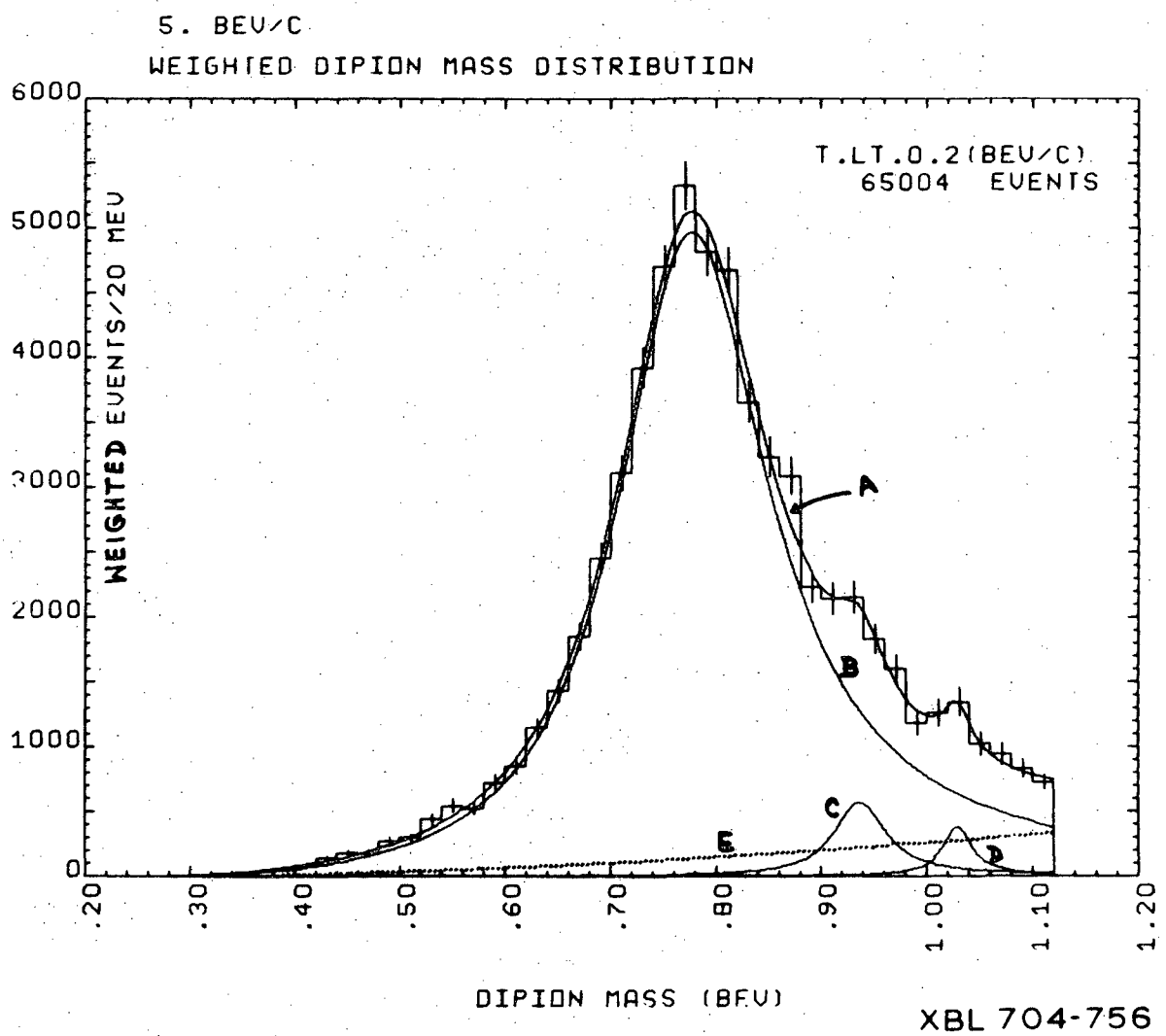
5. BEV/C
WEIGHTED DIPION MASS DISTRIBUTION
T.LT.0.2(BEV/C)
65004 EVENTS
WEIGHTED EVENTS/20 MEV
6000
5000
4000
3000
2000
1000
0
A
B
C
D
E
.20
.30
.40
.50
.60
.70
.80
.90
1.00
1.10
1.20
DIPION MASS (BEV)
XBL 704-756

Fig. 30b

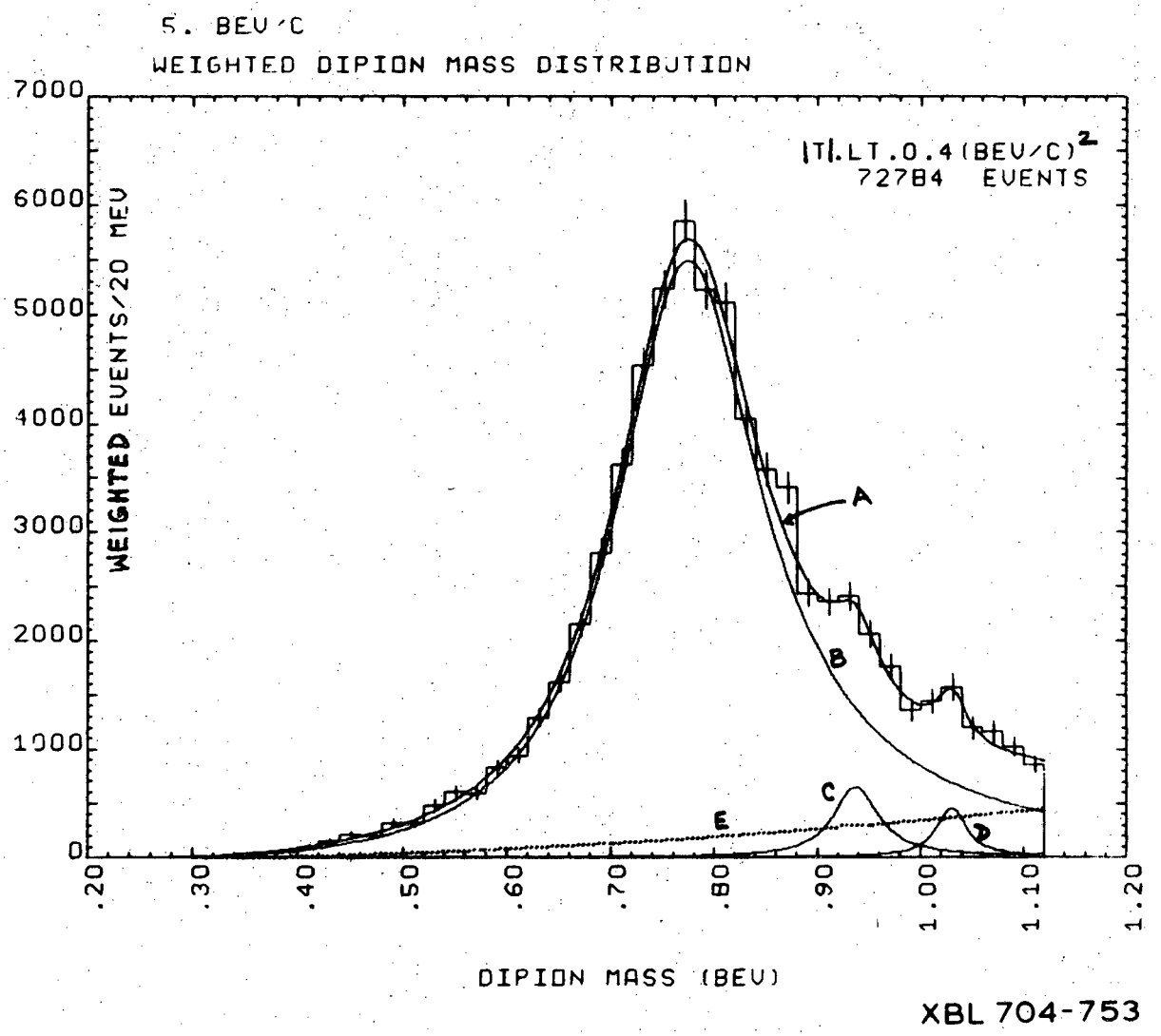
5. BEV/C
WEIGHTED DIPION MASS DISTRIBUTION
|T|.LT.0.4(BEV/C)²
72784 EVENTS
WEIGHTED EVENTS/20 MEV
7000
6000
5000
4000
3000
2000
1000
0
A
B
C
D
E
.20
.30
.40
.50
.60
.70
.80
.90
1.00
1.10
1.20
DIPION MASS (BEV)
XBL 704-753

Fig. 30c

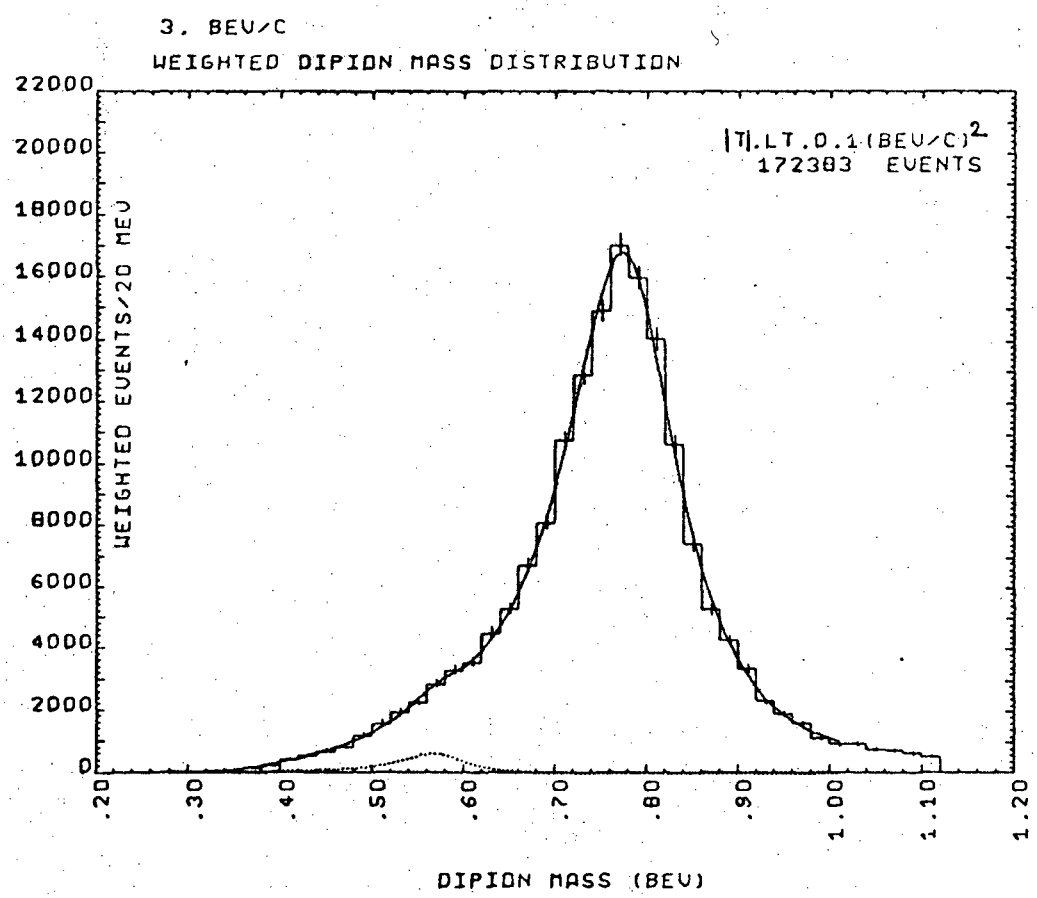
3. BEV/C
WEIGHTED DIPION MASS DISTRIBUTION
|T|.LT.0.1(BEV/C)2
172383 EVENTS
WEIGHTED EVENTS/20 MEV
22000
20000
18000
16000
14000
12000
10000
8000
6000
4000
2000
0
.20
.30
.40
.50
.60
.70
.80
.90
1.00
1.10
1.20
DIPION MASS (BEV)

Fig. 31(a)

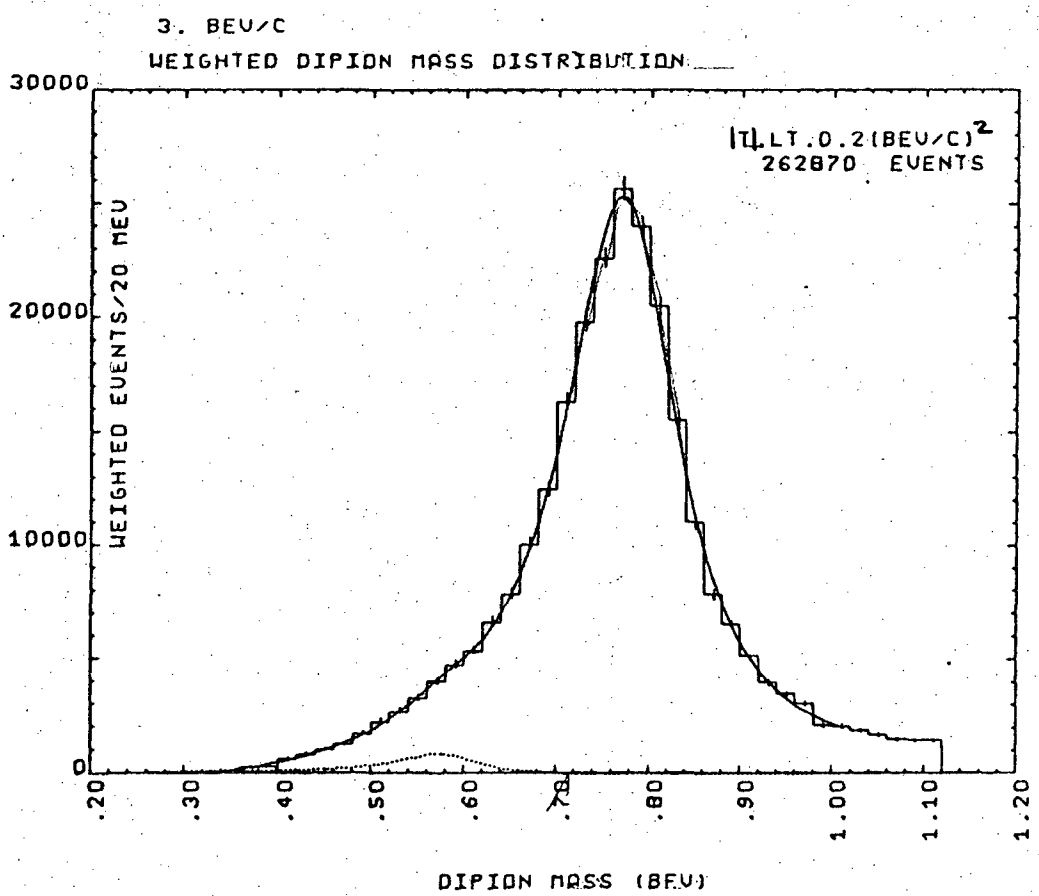
3. BEV/C
WEIGHTED DIPION MASS DISTRIBUTION
|T|.LT.0.2(BEV/C)²
262870 EVENTS
WEIGHTED EVENTS/20 MEV
30000
20000
10000
0
.20
.30
.40
.50
.60
.70
.80
.90
1.00
1.10
1.20
DIPION MASS (BEV)

Fig. 31(b)

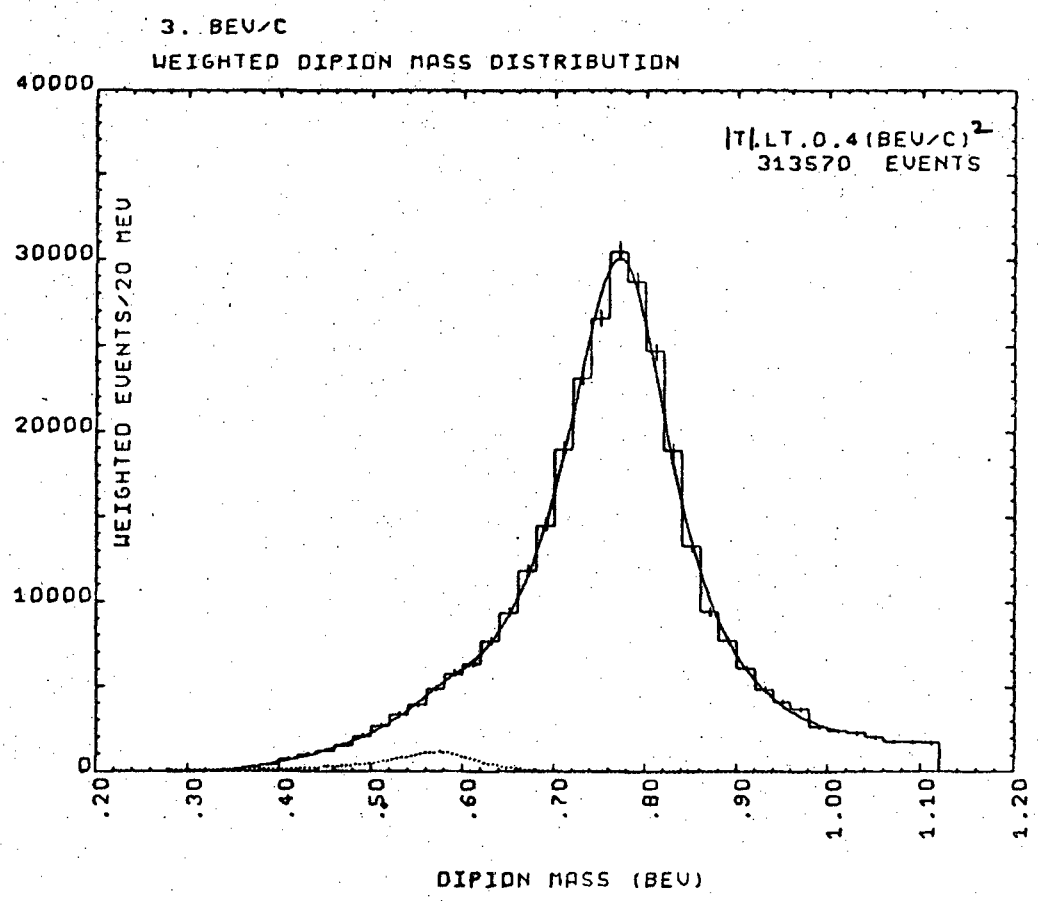
3. BEV/C
WEIGHTED DIPION MASS DISTRIBUTION
|T|.LT.0.4(BEV/C)^2
313570 EVENTS
WEIGHTED EVENTS/20 MEV
40000
30000
20000
10000
0
.20
.30
.40
.50
.60
.70
.80
.90
1.00
1.10
1.20
DIPION MASS (BEV)

Fig. 31(c)

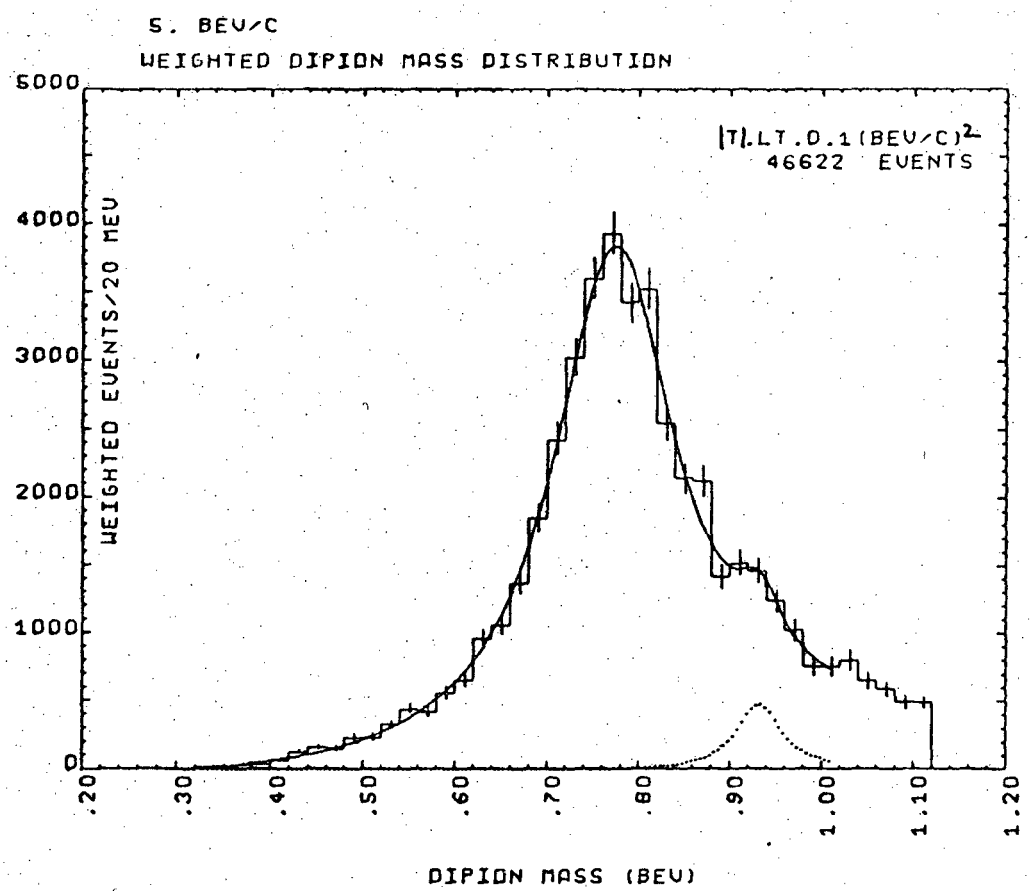
5. BEV/C
WEIGHTED DIPION MASS DISTRIBUTION
|T|.LT.0.1(BEV/C)2
46622 EVENTS
WEIGHTED EVENTS/20 MEV
5000
4000
3000
2000
1000
0
.20
.30
.40
.50
.60
.70
.80
.90
1.00
1.10
1.20
DIPION MASS (BEV)

Fig. 32(a)

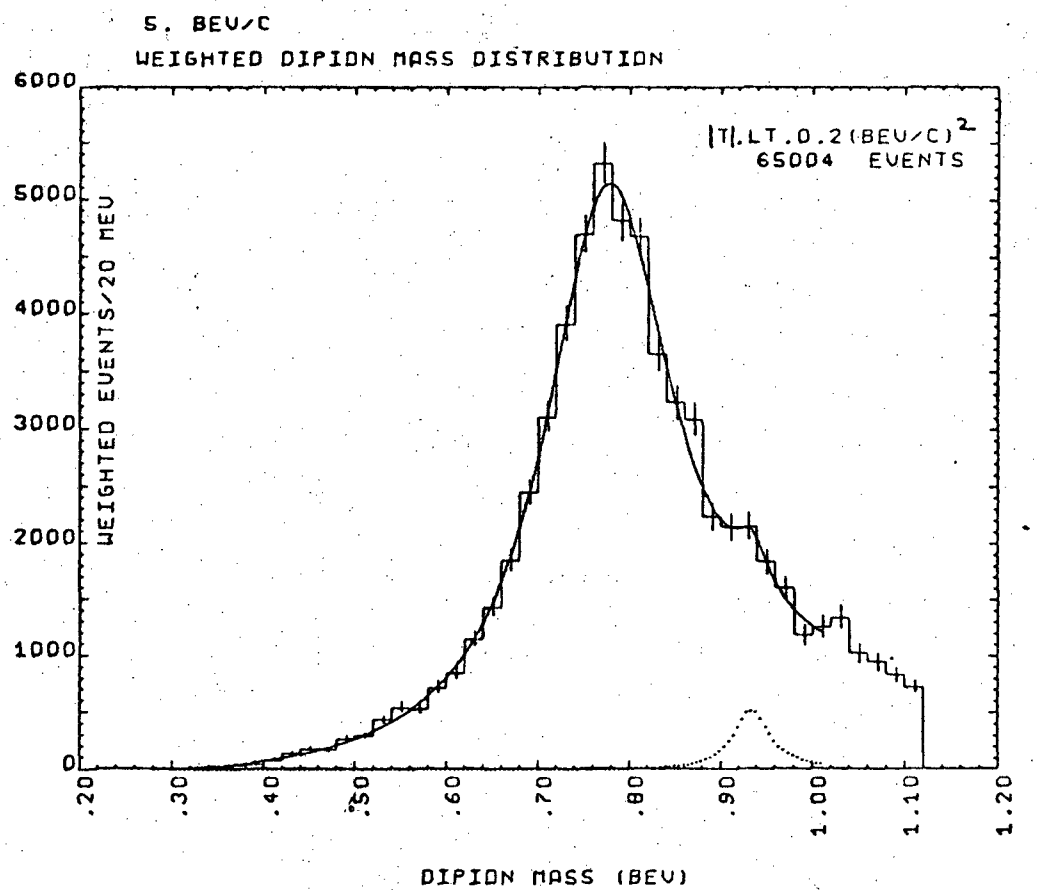
5. BEV/C
WEIGHTED DIPION MASS DISTRIBUTION
|T|.LT.0.2(BEV/C)^2
65004 EVENTS
WEIGHTED EVENTS/20 MEV
6000
5000
4000
3000
2000
1000
0
.20
.30
.40
.50
.60
.70
.80
.90
1.00
1.10
1.20
DIPION MASS (BEV)

Fig. 32(b)

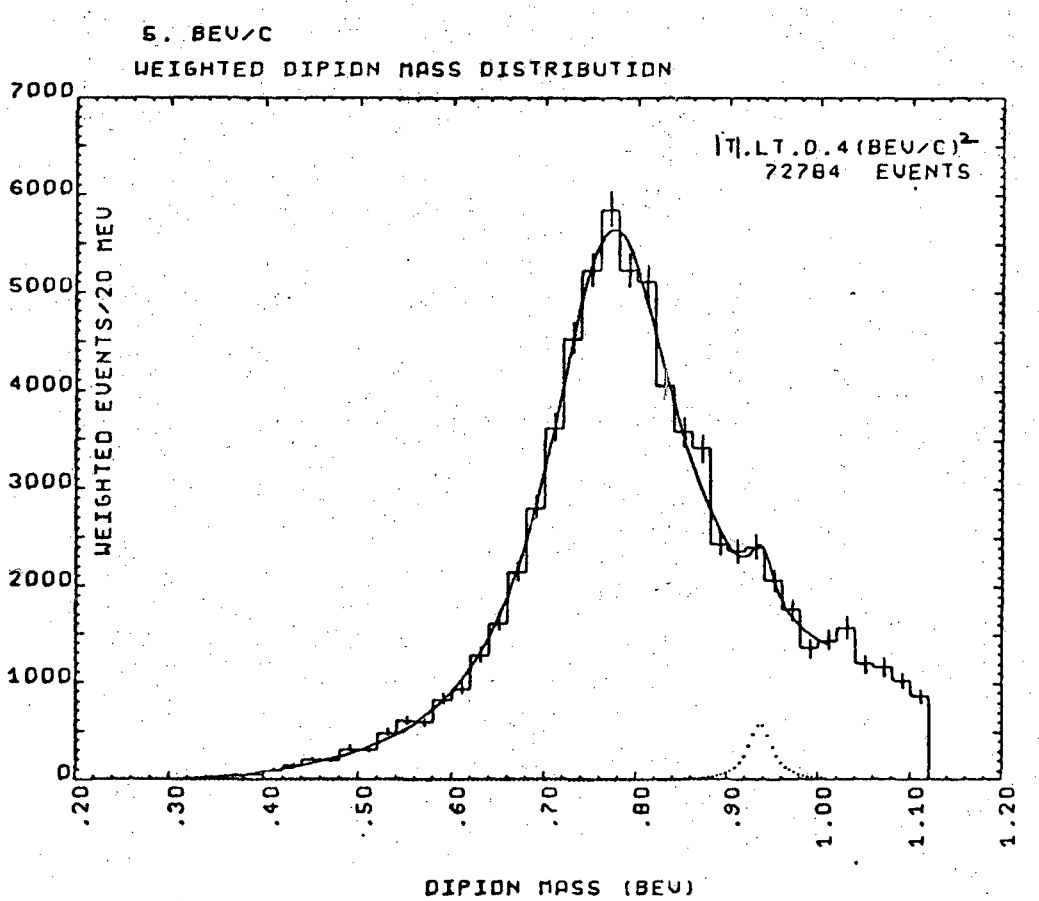
5. BEV/C
WEIGHTED DIPION MASS DISTRIBUTION
|T|.LT.0.4(BEV/C)²
72784 EVENTS
WEIGHTED EVENTS/20 MEV
7000
6000
5000
4000
3000
2000
1000
0
.20
.30
.40
.50
.60
.70
.80
.90
1.00
1.10
1.20
DIPION MASS (BEV)

Fig. 32(c)

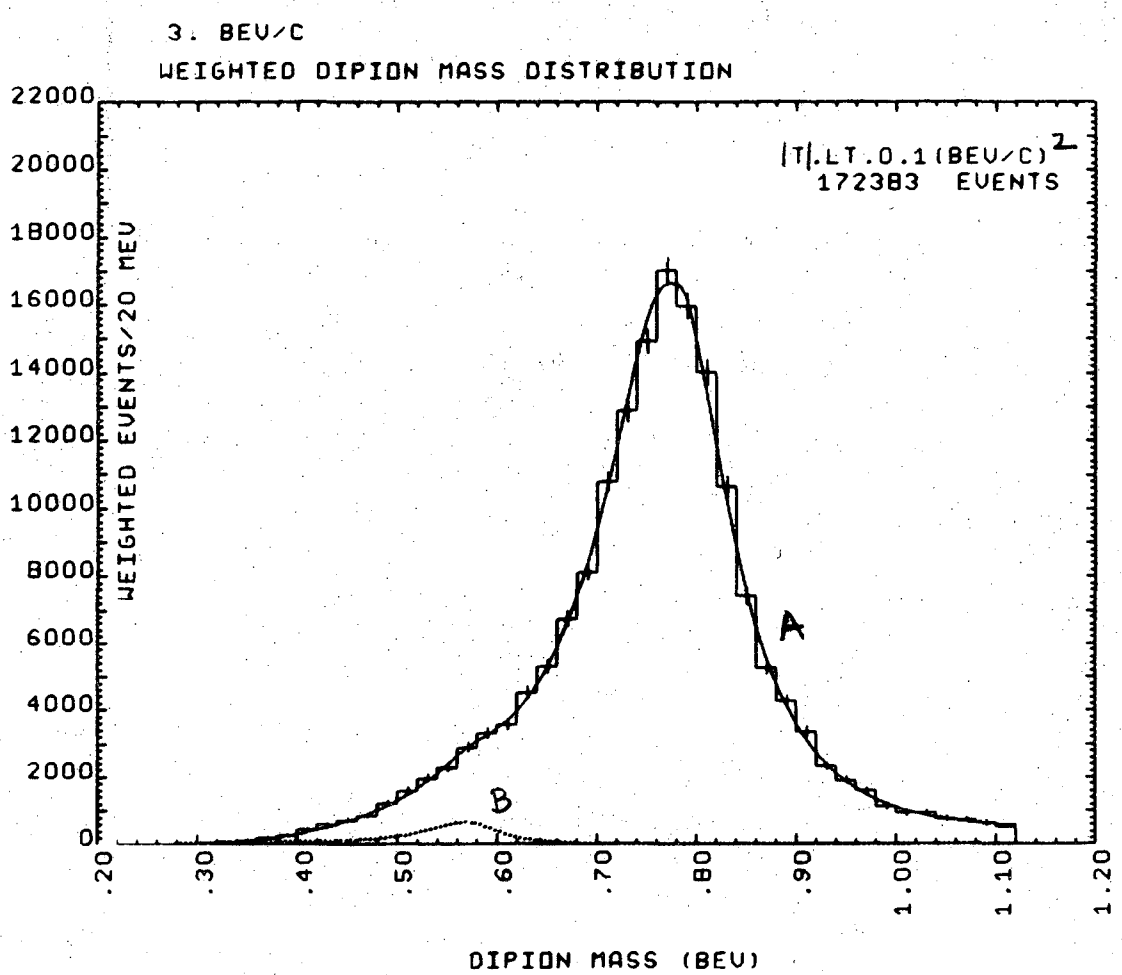

XBL 704-786

Fig. 33a

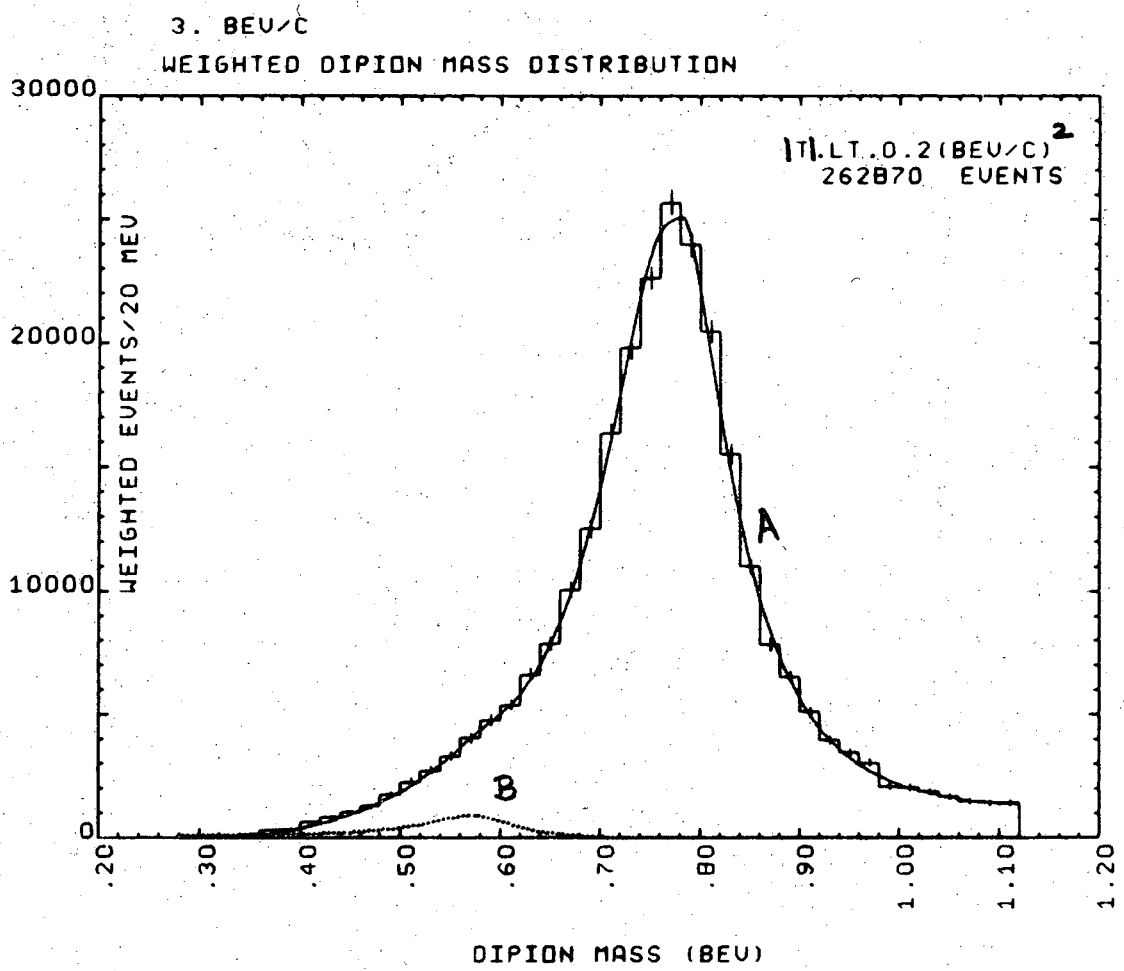

XBL 704-787

Fig. 33b

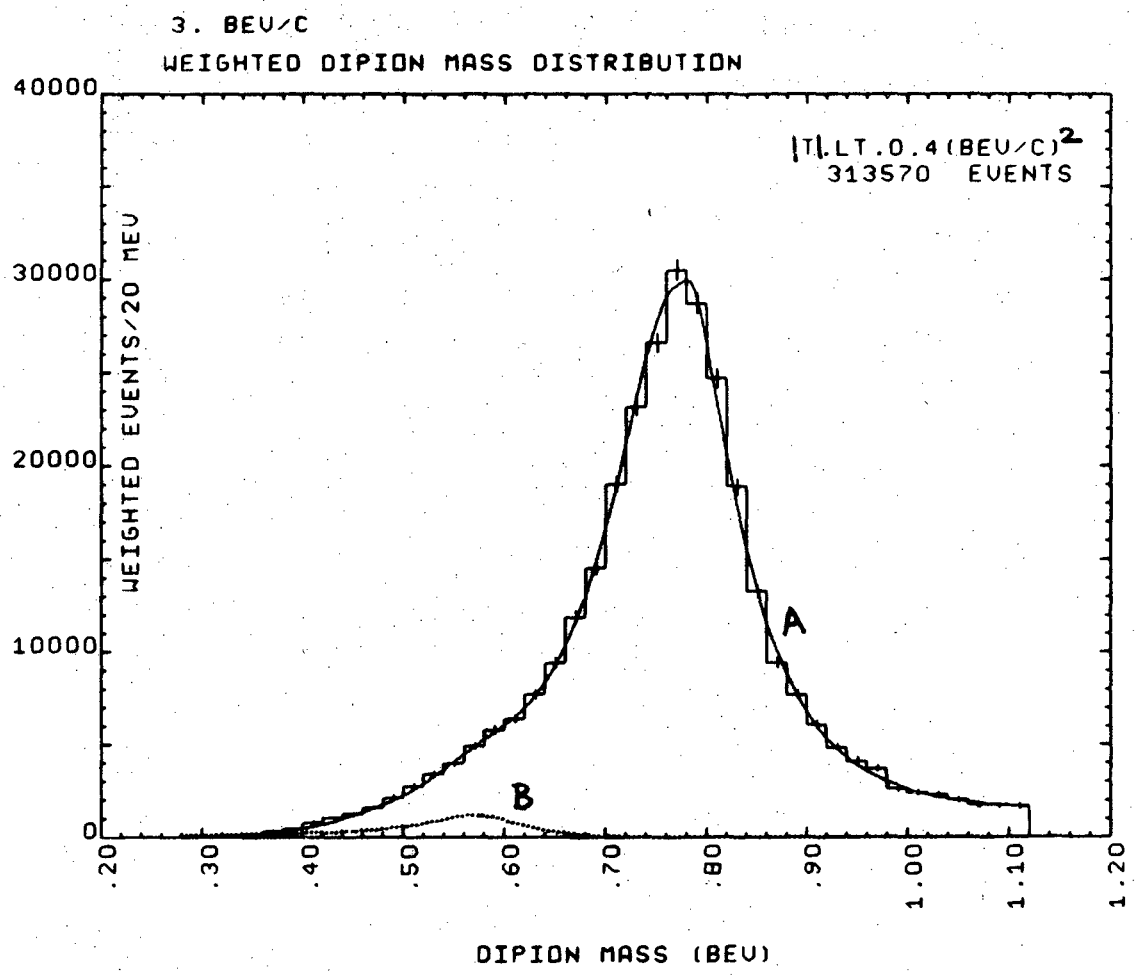

XBL 704-784

Fig. 33c

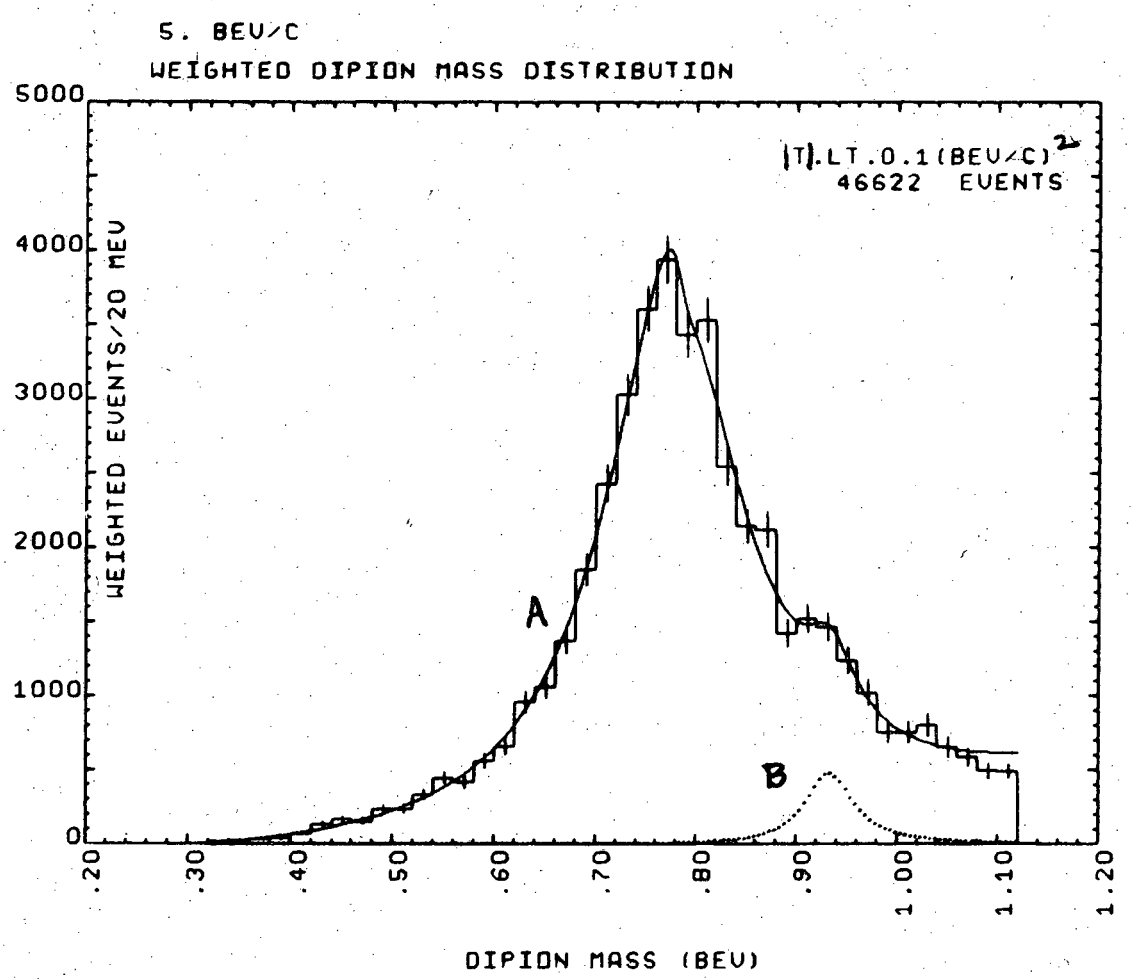

XBL 704-788

Fig. 34a

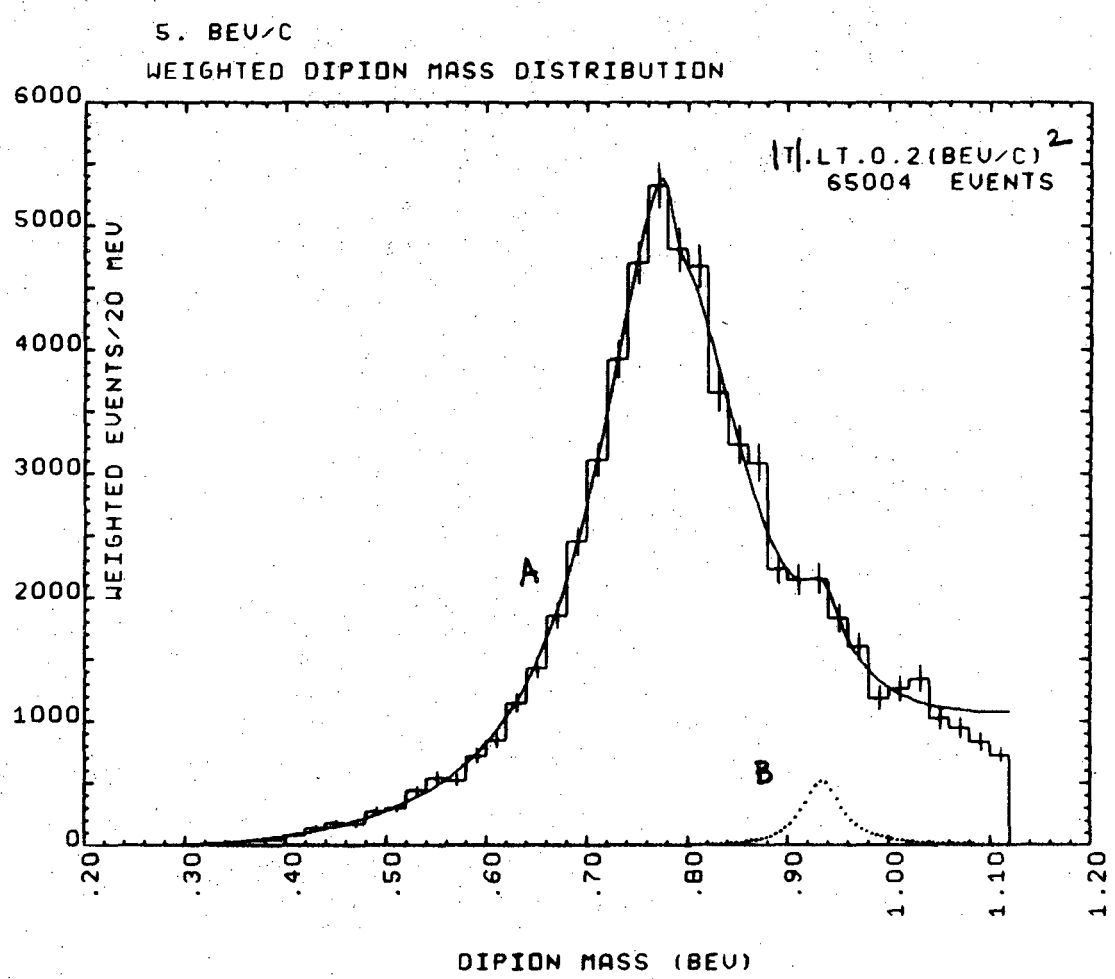

XBL 704-789

Fig. 34b

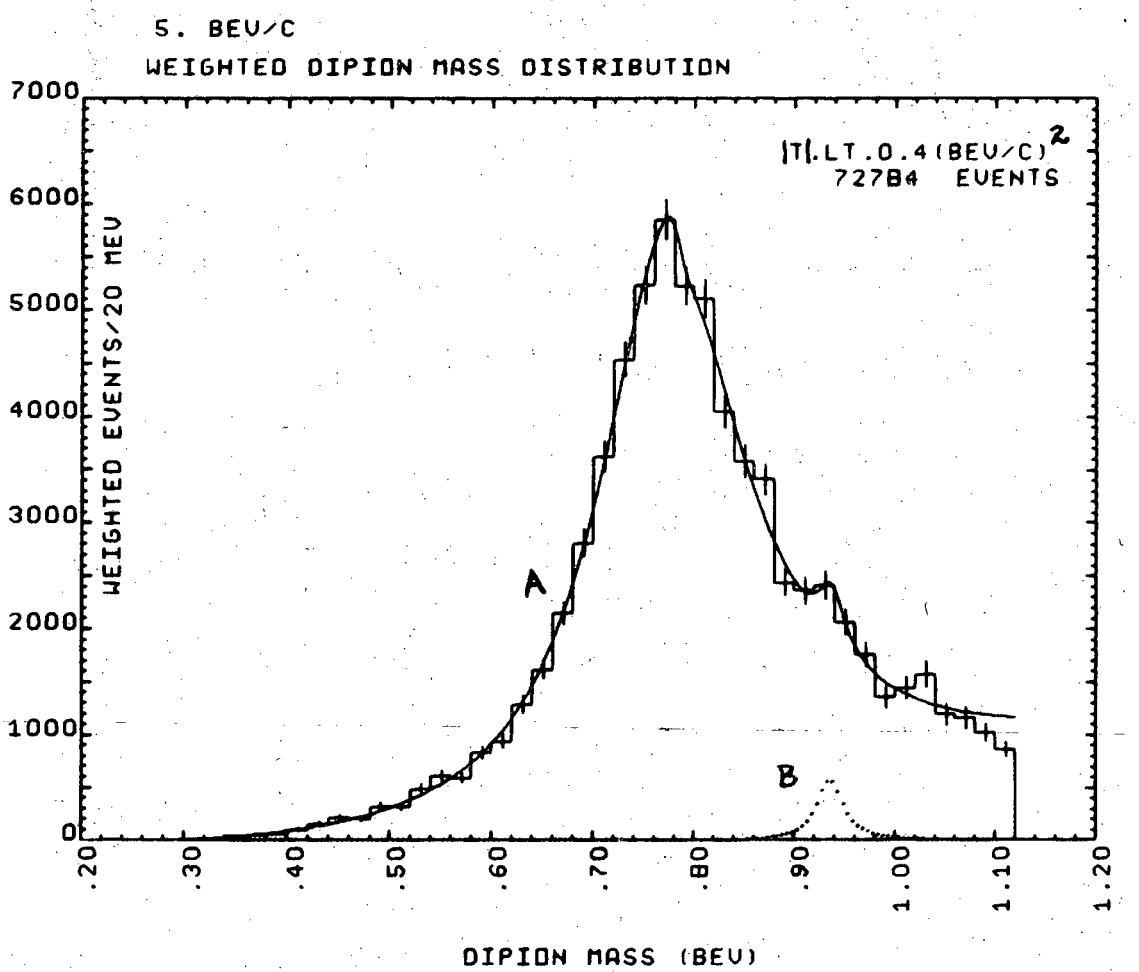

XBL 704-785

Fig. 34c

LEGAL NOTICE

This report was prepared as an account of work sponsored by the United States Government. Neither the United States nor the United States Atomic Energy Commission, nor any of their employees, nor any of their contractors, subcontractors, or their employees, makes any warranty, express or implied, or assumes any legal liability or responsibility for the accuracy, completeness or usefulness of any information, apparatus, product or process disclosed, or represents that its use would not infringe privately owned rights.

TECHNICAL INFORMATION DIVISION
LAWRENCE BERKELEY LABORATORY
UNIVERSITY OF CALIFORNIA
BERKELEY, CALIFORNIA 94720